DEVELOPMENT OF A 6 MV TANDEM ACCELERATOR MASS SPECTROMETRY FACILITY AND ITS APPLICATIONS.

Kamela Godwin Sekonya

Student number: 9811024J

A thesis submitted to the Faculty of Science,
University of the Witwatersrand, Johannesburg,
in fulfilment of the requirements for the degree of

Doctor of Philosophy

School of Physics

Johannesburg, 2017

I declare that this thesis is my own, unaided work. It was submitted for the Degree of **Doctoral of Philosophy** at the University of the Witwatersrand. It has not been submitted before for any degree or examination in any other university.

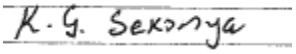

Kamela Godwin Sekonya

04 June 2017

ABSTRACT

Accelerator Mass Spectrometry (AMS) is an ultra-sensitive isotopic analysis technique that allows for the determination of isotopic ratios of rare long-lived radionuclides such as radiocarbon. AMS has become an important tool in many scientific disciplines, due to its sensitivity of detecting isotopic ratios at the level of 10^{-15} by making use of nuclear physics techniques and methods.

The objective of the present work was to design and implement a new AMS system at iThemba LABS, the first of its kind on the African continent. The system is described in detail along with the relevant ion optics simulations using TRACE-3D. Beam optics calculations were performed for carbon isotopes, using the TRACE-3D code, in order to optimize the design of the new spectrometer and assess its overall performance.

The AMS technique was applied in two unique South African research projects in relation to archaeology and environmental air pollution studies. The AMS technique, combined with the Proton-Induced X-Ray Emission (PIXE) technique, was also applied in an environmental study with respect to the contribution of contemporary and fossil carbon in air pollution in the Lephalale District, close to both the newly built Medupi coal-fired power station (~5 GW, the largest ever build in South Africa), and the existing Matimba coal-fired power station.

The discrimination of contemporary carbon and fossil carbon is accomplished by using the AMS technique in measurements of the $^{14}C/C$ ratios of aerosol particulate matter. The absence of ^{14}C in fossil carbon material and the known $^{14}C/C$ ratio levels in contemporary carbon material allows us to distinguish between contemporary carbon and fossil carbon and decipher in this manner different anthropogenic contributions.

The contemporary carbon throughout our sampling campaign in the Lephalale District has been measured to be approximately 53% of carbon aerosol. As many studies have been performed of contemporary carbon and fossil carbon, no other contemporary and fossil carbon source assessment method provides the definitive results that can be obtained from radiocarbon measurements.

PIXE analysis for the determination of the elemental composition of particulate matter in samples near the Medupi coal-fired power station in the Lephalale District was also performed for 6 elements, namely, K, Ca, Ti, Mn, Fe, and Zn. In the samples that were analyzed the particulate matter concentrations did not exceed the air quality standards regulation at Lephalale. The recommended daily limit air quality standard by South African legislation is 75 $\mu g/m^3$.

Enrichment Factor (EF) analysis of soil with respect to Fe shows anomalously high values for Zn.

AMS was also applied to archaeological studies of early herding camps of the khoe-khoe people at Kasteelberg, situated on the southwest coast in South Africa, and are among the best preserved sites of their kind in the world. Sea-shell samples from the Kasteelberg B (KBB) site have been dated with AMS at Lawrence Livermore National Laboratory (LLNL) in an effort to elucidate the relationship between the herder-foragers of the inland and shoreline sites in terms of migration patterns. The radiocarbon dates obtained are in general agreement with the other studies that have been performed on the site, and show that the ages of artifacts are less than 2000 years. The samples for this study originate from various well defined stratigraphic-levels at square A3 at KBB. It was evident from excavation that the artefacts seem to be of the same period and there is no evidence of mixing from different stratigraphic layers.

Radiocarbon dates were calibrated using Calib 6.1 and each was corrected for marine reservoir effect. The date range between the earliest and most recent dates that were obtained span gap is approximately 400 years from AD 825 to AD 1209. The majority of the radiocarbon dates of the KBB site belong to dates of 1002-1100 AD, the other few belong to 825-958 AD, and the last single date of 1209 AD. The new AMS dates from this work suggest the high probability that indeed there was a hiatus between the two occupations designated as lower and the upper KBB. The significant changes seen in material culture styles as well as in the nature of occupation and change in accumulation rate of deposits therefore do not necessarily indicate a cultural replacement caused by the arrival of a new population. This implies that the occupants of lower KBB may also have been Khoe-speakers, and not local San.

ACKNOWLEDGEMENT

I would like to thank Dr. Tom Brown of Centre of Accelerator Mass Spectrometry at Lawrence Livermore National Laboratory for fruitful scientific discussing on beam optics calculations for the Accelerator Mass Spectrometry (AMS) system. I wish to thank Professor Elias Sideras-Haddad for giving me opportunity to work in the field of accelerator mass spectrometry at the Physics Department, University of the Witwatersrand. Professor Stuart Piketh of the University of North West (Potchefstroom Campus) is being acknowledged for allowing me to use his equipment such as the Partisol-plus and filters for air quality in Lephalale projects for PIXE and environmental samples for AMS. I would also like to thank Professor Karim Sadir of the Archaeology Department at the University of the Witwatersrand for shell samples from Kasteelberg B. Many thanks goes to Paula Zermeno and Dr Tom Brown at Lawrence Livermore National Laboratory for introducing me to sample preparation of graphite targets for AMS and for helping me to prepare my quartz filter samples for the environmental air pollution studies and shell samples for the archaeology project. I also thank Dr. Tom Brown for scientific discussions on AMS and proof-reading of my thesis. I would like to thanks Mr. Hans Delsiki of iThemba LABS for the drawing of the lower energy and higher energy AMS systems of the iThemba LABS facility. I am indebted to the iThemba LABS Accelerator Group for providing me with TRACE-3D beam optics software and I do not forget Mr. Peter van Schalkwyk who helped with setting up the ion source test bench and testing the LLNL/CAMS, and Dr. Mark Sundquist of National Electrostatics Corp (NEC) for providing some information on some of the equipment in the AMS system.

Warmest thanks are expressed to my wife Mmamokete and my three children Maeleletje and Tumelo Sekonya and Tumelo Nogemane for supporting me all these years. I also thank my

parents Maeleletje and Ramaisela Sekonya for supporting me for so many years and allowing me to further my studies.

Financial supports from IAEA for allowing me undertake a scientific visit to LLNL and from NRF for study fees of my PhD are acknowledged.

CONTENTS

LIST OF FIGURES

LIST OF TABLES

CHAPTER 1
INTRODUCTION

1.1 Accelerator Mass Spectrometry

Accelerator Mass Spectrometry (AMS) is an analytical technique for measurements of isotopic abundances at extremely high sensitivity levels. Isotopic ratios in the range of 10^{-10} to 10^{-15} are currently routinely achievable for a large range of different isotopes along the nuclear chart. As in conventional Mass Spectrometry (MS), atoms are extracted from a sample, ionized, accelerated, separated by mass, charge, and/or energy and finally detected. One of the major limitations of conventional mass spectrometry techniques, such as Inductive Coupled Plasma Mass Spectrometry (ICPMS) and Secondary Ion Mass Spectrometry (SIMS), is their inability to break below the $\sim 10^{-9}$ isotopic ratio sensitivity regime due to isobaric and molecular interferences. While the Decay Counting (DC) technique can measure isotopic ratios as low as 10^{-17}, it suffers from its own inherent constraints which frequently result in long counting times as well as often requiring relatively large sample sizes (few hundred mg to g).

In terms of the new needs among many fast-developing sciences during the 60's and 70's, all the above limitations were overcome through the development of the AMS technique. This new spectrometry technique accomplished that by making use of electrostatic "Tandem" accelerators, which were traditionally used in nuclear physics research. The acceleration of ions to energies higher than those achievable with other conventional mass spectrometry technique made it possible to use nuclear physics instrumentation and methods to detect the isotopes of interest and at the same time, thereby eliminating molecular interference.

The idea of accelerator-based mass spectrometry can be attributed to Luis Alvarez and Robert Cornog at the University of California, Berkeley, when for the first time, they used a cyclotron as a mass spectrometer in an effort to detect naturally occurring ^{3}He (Alvarez and Cornog, 1939).

It was only in 1977 that Richard Müller, a student of Luis Alvarez, recognized that cyclotrons could be used to accelerate cosmogenic nuclei such as ^{10}Be, ^{3}He, ^{14}C, to energies such that background isobaric interferences could be separated by using solid state detectors (Müller, 1977). Richard Müller was also responsible for accomplishing the first successfully radioisotope date experimentally obtained using ^{3}H (Müller, 1977). Following that, experimental work performed with electrostatic Tandem accelerators by two groups at McMaster and Rochester led to the successful detection of ^{14}C and opened up a modern era of high sensitivity cosmogenic isotope detection (Nelson et al., 1977; Bennett et al., 1977). Most AMS systems in use today are laboratory- or facility-sized, with the majority of the AMS systems being used for ^{14}C measurements and a few also measuring other isotopes, such as ^{10}Be and ^{26}Al. There are now much smaller spectrometers being designed specifically for biological tracing applications with tritium and radiocarbon (Suter et.al, 1997). The numbers of existing AMS facilities that can measure a breadth of isotopes spanning the whole periodic table is ≤ 12.

The basic idea behind AMS is to extract radionuclei of interest out of the sample and count them directly, instead of counting their decays. The measurement time therefore can be reduced by orders of magnitude and the same stands for the size of the sample. As an example, using AMS a sample of 1 mg of carbon that is 50,000 years old will require a measuring time of about 30 minutes to produce a 1% precision radiocarbon measurement: by comparison, decay counting would require 1 g of the same carbon and 2 days of measurement time to produce a measurement with similar precision.

In terms of radiocarbon detection, the isobaric interference from ^{14}N is detrimental to the use of conventional mass spectrometry systems. In an AMS system the accelerated radiocarbon is initially in the form of a negative ion $^{14}C^-$. It is a fortunate fact that the life time ($\sim 5x10^{-14}$ s) of negative ^{14}N ions is too short to allow it to get into the accelerator and therefore the possible ^{14}N isobaric interference is eliminated in the first stages of ^{14}C AMS measurements. In terms of molecular isobaric interferences, the abundance of molecular ions of similar mass as ^{14}C produced in the ion source, that is $^{12}CH_2^-$ and $^{13}CH^-$, is much higher than that of the $^{14}C^-$ produced. However, the interfering $^{12}CH_2^-$ and $^{13}CH^-$ molecular ions are injected into the positive terminal Tandem accelerator together with the $^{14}C^-$. At the centre terminal of a Tandem there exists a so-called "charge exchange canal", consisting of a thin foil (~4 μg/cm) or stripping gas (N_2, Ar, etc) where atomic collisions take place between the incoming accelerated ions and the atoms of the foil or gas. During these collisions, electrons are stripped off the incoming ions and in this manner the accelerated species become positively charged, and are then subsequently accelerated a second time, away from positive terminal to the exit part of the accelerator. In addition, during these atomic collisions the interfering molecules, such as $^{13}CH^-$ and $^{12}CH^-$ in the case of radiocarbon measurements, dissociate and do not interfere in subsequent mass analysis of positively-charged ^{14}C ions. In AMS measurements of other isotopes, isobaric interferences, such as ^{10}B in ^{10}Be measurements may also be resolved using appropriate nuclear physics techniques such as gas ionization detectors or gas-filled magnets or stopper foils.

A major disadvantage of AMS lies with the cost of operation in terms of the setting-up, maintenance of the system and it is also technically complicated. Therefore, the most significant technical developments during the past years has been the trend towards smaller AMS system. In addition, sample preparation for radiocarbon in comparison to decay counting is small in size, more demanding and time consuming. This involves many different steps,

ranging from chemical pre-concentration and pre-treatment for enrichment or removal of contaminants respectively, to the graphitization or solidification of the radiocarbon interest which usually found in gaseous form which originates from a combustion process. Moreover the best decay counter can still achieve higher precision and lower backgrounds than an AMS system assuming a suitably large pure sample can be found.

The AMS techniques have almost completely superseded the older decay counting techniques and have extended the use of cosmogenic isotopes within the scientific community in addressing more complex scientific problems. AMS techniques allow for measurements of extremely low nuclide concentrations in very small size samples; such measurements were otherwise impossible to perform before the development of AMS.

The most important application of AMS has been in connection with radiocarbon measurements, where it has replaced decay counting as the primary analysis tool in almost all applications. AMS of long-lived radioisotopes has become an important tool in many scientific disciplines, such as archaeology, geosciences, hydrology, oceanology, paleoclimatology and a wide range of environmental applications. In addition, the efficient AMS detection of radioisotopes with longer half-lives, such as ^{10}Be, ^{26}Al, ^{36}Cl, ^{41}Ca, and ^{129}I, as well as other interesting unstable isotopes up to actinides, has opened up a large variety of new applications which could not be undertaken with conventional MS or decay counting systems.

The expected research outputs with particular relevance to southern Africa cover a wide range of scientific disciplines as listed below. As can be seen, these applications are of paramount importance to South Africa and prompted the development of the only AMS facility presently within the African continent; it is located at iThemba LABS within the campus of the University of the Witwatersrand. Brief descriptions are presented below of the roles that AMS measurements will play in a number of fields of study of particular relevance to South Africa.

Climatic Studies

Research in global and regional climate change is based on long-lived cosmogenic isotopes in the atmosphere such as ^{14}C, ^{10}Be and ^{36}Cl. These isotopes enable studies of longer-term climatic change and geologic processes and it make it possible to establish current and past ocean circulation patterns that are strongly coupled to climate, such as global patterns of changes associated with the *El Ninõ* effect. In such ocean circulation studies, South Africa's unique geographical location being at the meeting point of the Atlantic and Indian Oceans will allow important studies of oceanographic changes of global importance.

Characterization of anthropogenic and fossils sources of atmospheric pollution

Radiocarbon applications to atmospheric aerosol research relate primarily to the determination of fossil and contemporary components. Urban air pollution is a complex mix of organic molecules which are emitted by vehicle exhausts, by fossil-fuel and biomass burning, and many other industrial processes. Efforts to reduce/remediate urban air pollution require knowledge of the contributions from many different sources. Since about 90% of South Africa's energy is produced in coal-fired power stations, energy production results in an enormous CO_2 gas emission to the atmosphere. The CO_2 emitted from coal and other fossil fuel burning (e.g., vehicles) is essentially ^{14}C-free and, hence, AMS ^{14}C measurements can distinguish between such energy production emissions and emissions from the combustion of more recent materials, such as biomass burning.

Characterization of Regional Groundwater Systems

The advantage of AMS for Isotope Hydrology would lie principally in the ability to measure very small samples of ^{14}C and in the ability to measure longer-lived and/or low-level

isotopes such as ^{36}Cl. Isotope hydrology studies are vital for the entire Southern African region with a strong desert and semi-desert nature and scarce water resources.

Anthropology, Archaeology, History and Preservation Technology

AMS has made significant contributions in dating precisely the transition to the cultivation of crops, the age of stone tools, prehistoric rock painting, and other events and artifacts of historical and prehistorical importance. The requirement of microgram-sized samples makes the technique nearly non-destructive and enables its use in measurements of sensitive artifacts such as the San's paintings and historic pottery. The San people's paintings are one of the few well-preserved artifacts from hunter-gatherer societies, and the ability to date possible small amounts of organic carbon will give unique insight to migration periods of both the San people and newcomers of Bantu origin.

AMS in Biosciences

The high sensitivity of the technique for long-lived isotopes allows one to five orders of magnitude increase in the sensitivity of DNA adduct detection in carcinogenesis studies. This allows the testing of assumptions concerning physiological responses to small doses of carcinogens in relation to specific nucleotides; such AMS studies can be carried out at ng/kg exposure levels. Importantly, AMS in pharmacokinetic studies and in highly-specific radio-immunoassays could play an extremely important role in research in relation to the two highest killer diseases in South Africa, tuberculosis and HIV/AIDS.

Research in Earth Sciences and Geosciences

The high sensitivity of AMS makes it possible to use ^{10}Be measurements in establishing erosion rates of rocks, dating of young volcanic flows, marine and lake sedimentation rates,

which would contribute significantly to Earth Sciences and Geoscience research in Southern Africa and its station in the Antarctica.

Potential Isotopic Tools for Paleontological dating with AMS

Investigations to use ^{36}Cl and particularly $^{26}Al/^{10}Be$ as chronometers for paleontology are possible. South Africa is home to the world largest pool of Australopithecus Africanus with the Sterkfontein cave as a prime example. The Sterkfontein fossil site has produced the largest concentrations of early hominid fossils from a single locality (Berger et. al, 2002) and its dating is estimated to be around 3.5 million years, which is older than member 3 hominids (i.e. 3 million years) from Makapansgat (Vrba, 1982).

Nuclear Facilities and Safeguard related activities with AMS

South African government is considering building four new 20 GWe new nuclear power stations for electricity, in addition to the two existing nuclear power stations at Koeberg which generate 5% of South Africa's electricity. There are many long-lived radioactivities generated by nuclear facilities that are very hard to detect by conventional alpha, beta or gamma ray counting methods. As a result, their unintentional release occurs which, although of little significance biologically, provides information on the processes inside nuclear facility and nuclear power plants and reprocessing facilities emit these and other long-lived radioactivities into surrounding, which can be detected by AMS at sensitive levels provide valuable information.

Besides detecting long-lived radioactivities such as ^{129}I and ^{36}Cl, it is possible to detect rare long-lived isotopes of uranium and thorium using AMS because of the almost complete absence of isobars. Here, the destruction of interfering molecular ions and the fact that both negative and positive-ion ??? mass spectrometry are used, makes new measurements possible.

Consequently, as part of nuclear safeguards protocol, the assay of ^{236}U, ^{233}U in uranium and ^{229}Th, ^{230}Th in thorium could be valuable for indicating the human use of these elements in the past. Since, uranium has been distributed in the environment as a result of nuclear activities including nuclear explosions, accidents at nuclear plants, dumping of nuclear waste and releases from nuclear facilities (Hotchkis et. al., 2000).

The extension of early work by Zhao on "Detection of Naturally-Occurring uranium" will require some improvements in both the negative and positive ion- mass??? spectrometry if a goal of 1 ppt (10^{-12}) is to be reached (Zhao et. al., 1994). Moreover, the relative abundance of Pu isotopes was measured at 1.25 MV. Then, at the Australian National University (Fifield et. al., 1996; 1997) the utilization of higher terminal voltage (4 MV) allowed to improve the sensitivity of the method, both for the detection limit as minimum detectable number of U atoms in the sample, and lower limit isotopic ratio measurable in samples at high concentration. Similar detection system has been developed at the Vienna Environmental Research Accelerator (VERA) (Steier et. al., 2002), at LLNL (Brown et. al., 2002), at the Australian Nuclear Science and Technology Organisation (ANSTO) (Hotchkis, 2000), at lower energies at the Eidgenossische Technische Hochschule-ETH in Zurich (Walker et. al., 2005). More recent measurements of $^{233}U/^{238}U$ ratios to as low as 10^{-13} (Tumey et. al., 2009). Because ^{233}U has separate production pathways than ^{236}U, it can provide valuable information on the particular source of anthropogenic uranium in a sample.

1.2 Objective s of present PhD research study.

Within the above context, the objectives of the present thesis are to:

- Develop an optimized design of a new AMS Laboratory based on the existing 6 MV EN Tandem facility at iThemba LABS, through beam optics calculations.
- Establish a modern sample preparation laboratory with the main emphasis on the pretreatment and graphitization processes for radiocarbon AMS measurements of a variety of samples types.
- Apply AMS and PIXE techniques in environmental studies related to the largest newly-built coal-fired power station (~5 GW) at Medupi-Lephalale in South Africa.
- Apply AMS techniques in dating studies of archaeological remains from sites of Khoi-speaking settlements at Kasteelberg in the south Western Cape with the goal of contributing to resolving migration patterns and elucidating the transition process from hunting to herding in southern Africa.

The last two applications in environmental and archeological studies, which have their own merit as scientific projects, constitute a first effort for cross-referencing and standardization of the new AMS system through comparisons of measurements made on the same samples at both the Centre of Accelerator Mass Spectrometry at Lawrence Livermore National Laboratory and the new AMS facility at iThemba LABS.

In developing the new AMS facility at iThemba LABS, the previously existing 6 MV EN Tandem Laboratory was heavily modified, upgraded and redesigned in order to provide the needed elements for an AMS measurement capability. The upgrade included an entirely new Low Energy (LE) injection system, the replacement of the accelerator tubes and charging

system, and the design and implementation of a new High Energy (HE) beam transport system including new magnetic and electrostatic isotope separation elements and a multi-anode energy-loss gas ionization detector. The LE and HE beam transport systems were optimized through beam-optics computer modeling using the TRACE-3D code. The calculations comprised of two parts. The first part concerned the LE injection system from the ion source up to the EN's central terminal and included the charge exchange canal. The second set of beam optics calculations was performed for a beam exiting the charge exchange canal with an implicit "virtual emittance", based on the results from the first calculations. These second calculations included the two HE acceleration tubes, a series of electrostatic and/or magnetic quadrupoles, the AMS 90° bending magnet, the 22.5° cylindrical electrostatic analyzer and the 25° bending magnet before the energy-loss gas ionization detector. The main purpose of this thesis is the development of 6 MV EN Tandem accelerator to AMS system. Firstly, transport of the beam of interest using beam optics calculation in the LE system through the injection magnet which will match the acceptance of the accelerator. Secondly, the beam optics calculation will be performed on HE beam line to the end of detector. The intention is to have the AMS system, firstly for the measurement of ^{14}C and thereafter AMS measurements for ^{10}B, follow by ^{27}Al and other isotopes.

Graphite is the most common type of sputtering targets used in ^{14}C AMS. The objective of iThemba LABS sample preparation laboratory is to produce graphite a targets by the catalytic reduction of CO_2 by hydrogen over an iron-group metal powder (Vogel et. al., 1984). The goal of the iThemba LAB AMS facility is to reach a throughput for radiocarbon measurements of more than 3000 samples/years. The structure of iThemba LABS sample preparation will consist of 12 graphitization units and 12 individual sealed-tube combustion units.

The AMS techniques together with Proton Induced X-Ray Emission (PIXE) were applied to environmental samples from the Lephalale region where the largest coal-fired power station (~5 GW) in South Africa is being built at Lephalale. PIXE analyzes of atmospheric aerosol samples with respect to six elements, namely, K, Ca, T, Mn, Fe, and Zn were performed to assess the sources of pollution in the region.

An important issue in both scientific and policy terms is the relative contributions of anthropogenic and biogenic sources to the carbon aerosol. The distinction between "wood-burning" by the local communities and "fossil fuel burning" due to combustion engines and coal-fired power stations is of vital importance in environmental studies and pollution legislation. An analytical challenge is the very high level of accuracy and precision to which the very low abundances of ^{14}C need to be quantified. The capability of AMS measurements on radiocarbon samples of environmental pollution using very small samples of microgram quantities is essential. The $^{14}C/C$ will be used to discriminate the carbon concentrations contents between the contemporary and fossil carbon fractions of the aerosol samples collected at Lephalale. The measurements will help air quality legislation in the region.

Archaeology research with respect to establishing migration patterns and evolution of social structures in South Africa can be of a complex nature particularly in connection with studies of hunter gather and early pastoral societies, as writing and therefore written history had not been developed.

According to archaeological findings, sheep and pottery appeared in the region of the Cape about 2000 years ago. One of the important questions is in regard to their origin. Two different views have prevailed over the last 30 years. The first asserts that the so-called Khoi-speakers introduced them during their migration from the north (Walker, 1983, Parkington, 1984, Parkington et al., 1986, Smith, 1992, Boonzaier et al., 1996). The second asserts that certain livestock diffused southward and were partially adopted by Cape dwelling hunter-

gatherers (Deacon et al., 1978, Deacon, 1984, Klein, 1986, Kinahan, 1995). Neither of these hypotheses enjoys sufficient supporting archaeological evidence to confirm or refute either beyond any reasonable doubt. Linguistic studies and the absence of the wild-progenitors of livestock in southern Africa indicate that both the Khoi-speakers and the earliest livestock must have come from the north, indirectly supporting the migration hypothesis that Khoi and livestock came together. The present work constitutes part of an attempt to test these two opposing hypotheses by establishing that either:

a) that livestock and pottery appear together as a package at sites dating to around 2000 BP (in support of the migration hypothesis), or
b) the earliest livestock and pottery, it is argued, probably reached the Cape by process of diffusion (in support of the diffusion hypothesis)

Recently Kamir Sadr and others (Sadr, 2007, Sealy and Yates, 1994; Smith, 2006) have produced test results in support of the migration scenario, and evidence suggests that the livestock, pottery and Khoi language spread as an integrated package around 2000 years ago, perhaps combined with a distinctive style of geometric rock art (Smith and Ouzman, 2004). Further, it has been suggested that this spread was a result of migrations from the far north of Botswana (Westphal, 1963), and possibly with ultimate origins in East Africa (Smith, 2008). Khoi-speaking hunter-gatherers appearance on late first/early second-millennium AD development in the Cape, preceded by many centuries in which sheep were exchanged among indigenous hunter-gatherer populations in Namibia and western South Africa (Sadr, 1998; Sadr, 2008). The alternative is that some of the first livestock diffused southward from one to another group of hunter-gatherers (Deacon et. al., 1978; Deacon, 1984, Klein, 1986; Kinahan, 1995). The objective is to see whether livestock and pottery appear together as a package at sites dating to around 2000 BP. The test of this hypothesis depended to some extent on whether the switch from lower to upper occupation at KBB was a rapid event or whether an occupational

hiatus existed between the lower and upper deposits of KBB. The new AMS dates reported here suggest the high probability that indeed there was a hiatus between the two occupations designated as lower and the upper KBB. The significant changes seen in material culture styles as well as in the nature of occupation and change in accumulation rate of deposits therefore do not necessarily indicate a cultural replacement caused by the arrival of a new population. This implies that the occupants of lower KBB may also have been Khoi-speakers, and not local San.

Outline of the thesis

CHAPTER 2
RADIOCARBON DATING AND CALIBRATION

2.1 Radiocarbon in the environment

The most abundant carbon isotopes are ^{12}C and ^{13}C with a relative occurrence in the atmosphere of 98.89% and 1.11%, respectively. Both of these isotopes are stable. However, a heavier carbon isotope, ^{14}C is radioactive and has a natural abundance in the atmosphere of about 1.2×10^{-12} relative to ^{12}C.

The possibility of production of ^{14}C in the Earth's atmosphere by cosmic-ray neutrons was first suggested by Montgomery and Montgomery (1939), soon after discovery of cosmic-ray neutrons (Locker, 1933; Rumbaugh and Locker, 1936). Korff pointed out that most of the slow cosmic-ray neutrons would lead to production of ^{14}C because of the rather high thermal neutron cross section on ^{14}N (Korff and Danforth, 1939; Bethe et.al, 1940):

$$^{14}N + n \rightarrow {}^{14}C + p \qquad (2.1)$$

with ^{14}C decaying back to ^{14}N via β-decay according to

$$^{14}C \rightarrow {}^{14}N + \beta^- + \bar{\nu}_e \qquad (2.2)$$

Subsequently, Libby developed the Nobel Prize winning radiocarbon dating technique (Arnold, and Libby, 1949), based on the ^{14}C β-decay using decay counters. The fact that the ^{14}C has half-life ($t_{1/2}$) of 5600 years, when coupled with routine measurement backgrounds, limits routine radiocarbon dating of old artifacts to ages less than 45,000 to 55,000 years ago.

The decay of ^{14}C follows the radioactivity exponential law

$$A = A_0 e^{-\lambda t} \qquad (2.3)$$

A_0 is grams of radioactive isotope that has half-life of t of years, A refers to specific activities (i.e., decay per gram of material) and $\lambda = \ln 2/t_{1/2}$ *is* the reciprocal mean lifetime of ^{14}C.

The current accepted half-life is not 5568 yearss, but is now 5730 yearss. However, Libby's half-life of 5568 (Libby, 1955) is still widely used in the radiocarbon community in calculations of radiocarbon dates. Because of this relatively long half-life, atmospheric circulation distributes ^{14}C uniformly across the surface of the earth. The amount of radiocarbon in the Earth system is in an equilibrium state, with a balance of production and decay rates.

For a Libby half-life of 5568 years, and when measured in 1950, radiocarbon ages before 1950 AD are calculated as (Stuiver and Polach, 1977):

$$t = -8033.\ln\left(\frac{A_{SN}}{A_{ON}}\right) \tag{2.4}$$

The time t refers to radiocarbon years before 1950 (according to the conventions of Stuiver and Polach (1977)). The conventional radiocarbon age (t) is expressed in radiocarbon years Before Present (BP), where Present is defined to be 1950. 1950 was chosen as reference year because of historical reasons in the years surrounding the publication of the first experimental results and also because following years the atmospheric radiocarbon concentration started to increase considerably due to atmospheric nuclear weapon tests. A_{SN} is the measured value that is related to the sample material. A_{ON} is the measured value that is related to the internationally accepted primary standard for radiocarbon dating, OX I; whereas OX I is oxalic acid ^{14}C standards. The actual measurements of sample and oxalic acid activities were not made in 1950. The measured A_{SN}/A_{ON} does not change with time and it stays equal to the 1950 ratio because both sample and oxalic acid lose their ^{14}C at same rate. Thus the calculated age (t), given by Eq. (2.4), is fixed number independent of the year of measurement.

The industrial revolution of the late 19th century changed the ^{14}C content of the atmosphere. The increased burning of fossil fuels, which are free of ^{14}C (virtually all of the ^{14}C

originally fixed in organic matter from millions of years ago decayed long ago), added a significant amount of ^{14}C-free carbon dioxide to the atmosphere. As result, the atmospheric $^{14}C/^{12}C$ ratio was lowered and thus, radiocarbon ages measured samples effected by this fossil-fuel sourced CO_2 will provide erroneously old estimates of the real ages of the samples (Suess, 1955). The industrialization process has been not concluded yet, so this so called Suess effect is still present in all living organism (Levin et. al, 2008). Figure 2.1 shows the atmospheric history of ^{14}C from AD 1511 to AD 1954 (Stuiver, 1993). The strong decrease that occurs after AD 1880 is due to dilution by anthropogenic addition of CO_2 during the industrial revolution by burning of fossil fuels. An oceanographic radiocarbon result that appears on vertical axis of Fig 2.1 are generally reported as delta ^{14}C, activity ratio relative to standards (NBS oxalic acid, 13.56 dpm per g of carbon) with a correction by anthropogenic CO_2 with age corrections of the standard material to AD 1950.

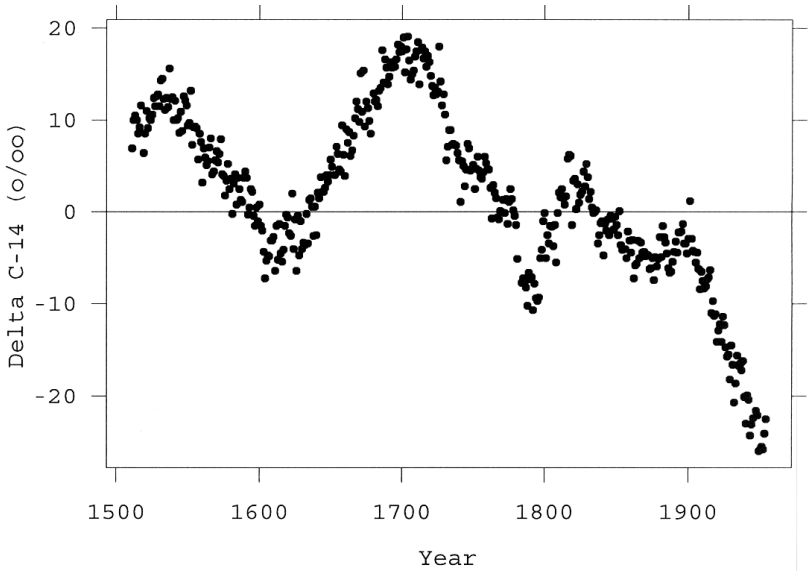

Figure 2.1: Atmospheric history of ^{14}C (Stuiver, 1993 as presented in Key, 2001). Most of the decrease since 1890 is due to the addition of anthropogenic CO_2 into the atmosphere by the burning of fossil fuels following on the industrial revolution.

However, atmospheric nuclear weapon testing in the 1950s and early 1960s carried out by the United States of America (U.S.A), the former Soviet Union, the United Kingdom (U.K.) and France, resulted in the production of significant quantities of thermal neutrons in the stratosphere. These thermal neutrons reacted with ^{14}N to produce significant additional ^{14}C in the atmosphere; this ^{14}C formed CO_2 and dispersed throughout the atmosphere, and was subsequently slowly equilibrated with components of the terrestrial ecosystem and the oceans (via CO_2 gas exchange at the ocean surface). This additional "bomb" ^{14}C resulted in a substantial increase in the atmospheric ^{14}C concentration. Figure 2.2 shows ^{14}C bomb peaks as deviation of ^{14}C ($\Delta^{14}C$) from the natural (reference) value in atmospheric CO_2 during the second half of the 20th century in the Northern Hemisphere (NH) and in the Southern Hemisphere (SH) (Levin and Hesshaimer, 2000). By 2009 the decreasing atmospheric ^{14}C level was approaching the pre-nuclear and pre-industrial revolution "natural" ^{14}C level (Kutschera, 2010). The measured ^{14}C bomb "pulse" in atmospheric CO_2 in both the Northern and the Southern hemisphere (Levin and Hesshaimer, 2000), provides unique records reflecting inter-hemispheric exchange across the Inter-Tropical Convergence Zone and re-distribution from the atmosphere into the oceans and the biosphere. The fact that all organisms that incorporated carbon from these reservoirs during the second half of the 20th century are labelled with bomb ^{14}C has been used in aging such organisms during this period; e.g., in studies involving the aging of cells in the human brain and the human body (Spading et al, 2005; Spading et al, 2008). Certain air pollution investigations in particular would not have been possible without the use the AMS technique in that AMS allowed the measurement of ^{14}C in very small samples (containing 10s of µg of carbon) which permitted the partitioning of the measured carbon between fossil-fuel and contemporary carbon sources (Bench, 2004; Bench et al., 2007).

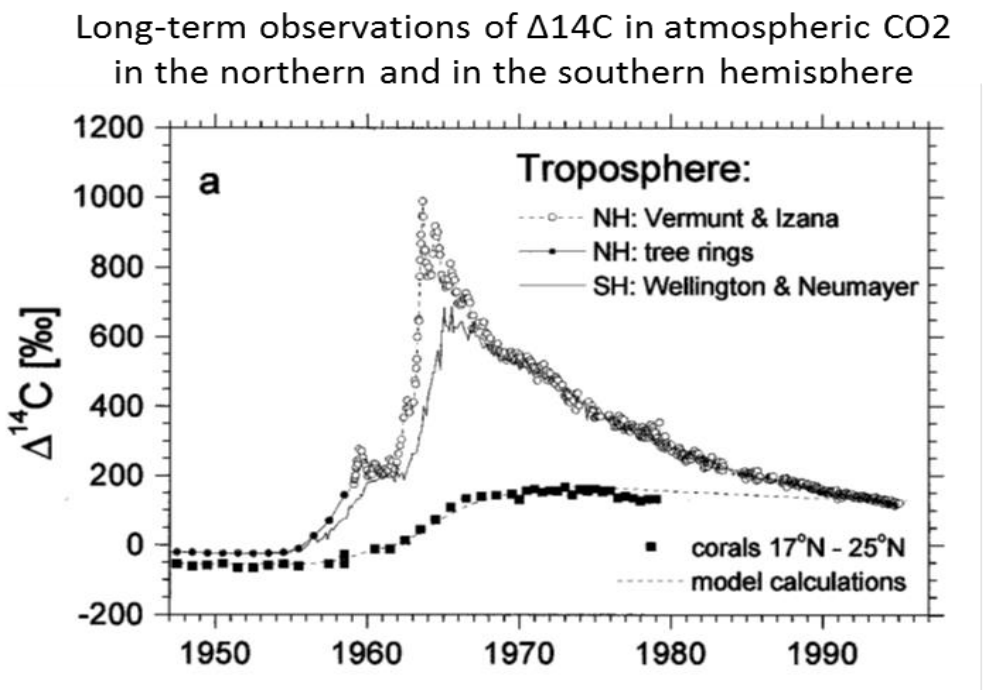

Figure 2.2: The ^{14}C bomb peak: deviation of ^{14}C ($\Delta^{14}C$) from natural (reference) value in atmospheric CO_2 during the second half of the 20th century in the northern hemisphere (NH) and the southern hemisphere (SH) (Levin and Hesshaimer, 2000). After the Nuclear Test Ban Treaty (NTBT). ^{14}C rapidly distributed to other domains of the Earth system. The relatively slow radioactive decay of ^{14}C is insignificant over this timescale; the shape of the bomb peak curve after 1963, was determined primarily by the mean residence time of ^{14}C molecules in the atmosphere (~7 years) (Kutschera, 2010).

2.2 Dating and calibration

Variations in the atmospheric ^{14}C content through time, and inaccuracy in the half-life used to calculate radiocarbon ages cause ^{14}C ages to deviate from the "calendar year" timescale. Calendric ages can be derived from radiocarbon dates through the use of a "calibration curve", a plot of, for example, ^{14}C ages measured on tree rings vs dendrochronologically-determined calendar ages of those tree rings. Calibration of radiocarbon ages corrects for both the offset introduced by use of the Libby half-life and for the temporal variability of the atmospheric ^{14}C content.

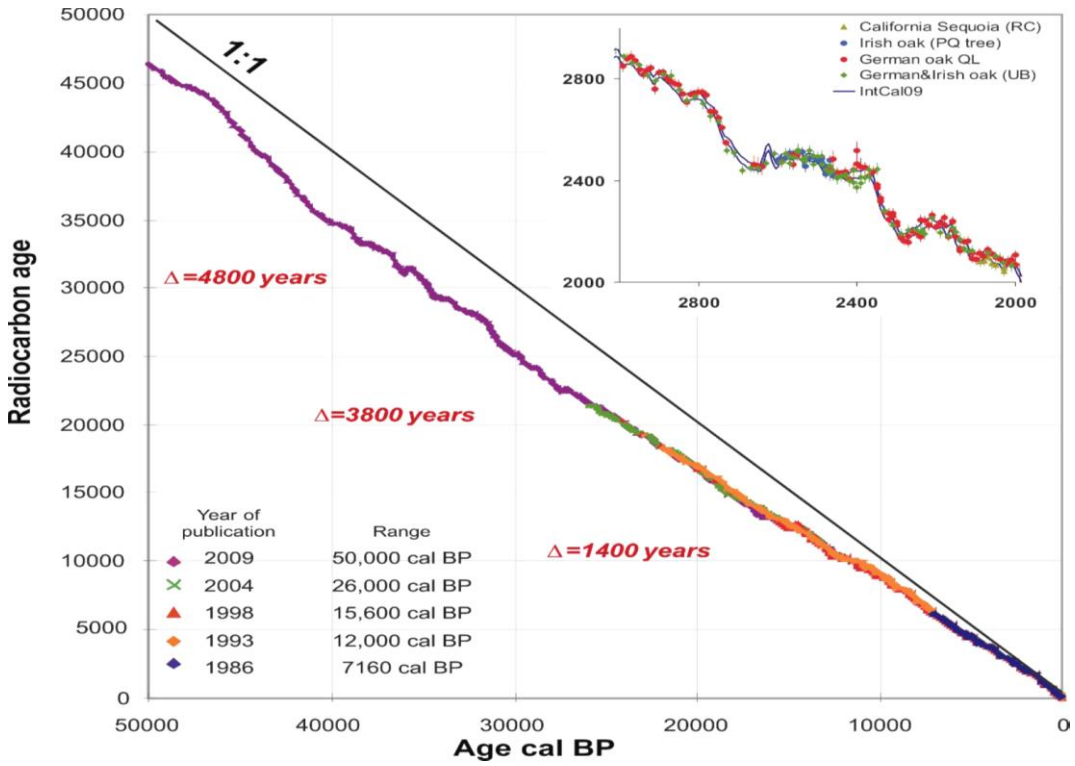

Figure 2.3: Historical comparison of radiocarbon calibration curves published since 1986**.** The straight line would apply if radiocarbon and calendar ages were equal, and the Δ values indicate approximate deviations of calendar ages from radiocarbon ages. The inset in the upper right corner shows a selection of the datasets used for construction of the radiocarbon calibration curve between 2 and 3 ka BP and IntCal09 calibration. Datasets: IntCal (Reimer et al., 2009), IntCal04 (Reimer et al., 2004), IntCal98 (Stuiver et al., 1998), IntCal 93 (Stuiver et al., 1993), IntCal86 (Stuiver & Kra, 1986). Datasets for the inset: German Oak QL, Irish oak (PQ tree) and California Sequoia (Stuiver and Braziunas, 1993; Stuiver etal, 1998); German and Irish oak UB (Pearson et al, 1986; Piotrwska et al., 2010).

The construction of calibration curves relies on ^{14}C dating of known-age archive samples such as dendrochronologically-dated wood, corals and speleothems (calendric ages from U/Th measurements), and annually-layered lake or marine sediments (calendric ages from layer counting). The updated calibration curve IntCal09 is described by Reimer et al. (2009). This curve (Fig. 2.3) shows clearly that the difference between radiocarbon age and calendar age generally increases with sample age, for example up to more than 1000 years for samples for samples 5k-10k years old. A characteristic feature of the calibration curves is the presence of periods where single ^{14}C ages correspond to multiple calendar ages, known as plateaux

(periods of several hundred calendar years during which radiocarbon age is nearly constant) and wiggles (periods where radiocarbon age fluctuates rapidly) (Piotrowska et al., 2010).

Calibration is a mathematical procedure that places the measured radiocarbon ages (taken with their error) on the experimentally drawn curve. Calibration of a single radiocarbon age is performed using statistical methods. In the probabilistic calibration procedure, calendar ages, corresponding to the radiocarbon age obtained for the measured material, are given with the probability distribution (68% and 95% confidence intervals (CI) for 1 sigma and 2 sigma errors respectively) (Stuiver and Reimer; 1986,1989). The calibration of a set of radiocarbon ages is usually performed with the help of dedicated statistical programs such as CALIB (Stuiver and Reimer, 1993), CALIB (Reimer et al., 2009) and OxCal (Bronk Ramsey, 2009). The calibrated radiocarbon averages are then reported as 'cal AD/BC' or 'cal BP' (calibrated years BP). Because of the wiggles on the calibration curve, the transfer to calendar time scale may have a complicated probability distribution; see Fig. 2.4 for typical calibration of radiocarbon age from Xia-Shang-Zhou (Guo et.al., 2000). The calibration of radiocarbon age to calendar age with the tree ring calibration curve will usually enlarge the age error due to the wiggles of the calibration curve. In a typical situation, the enlargement factor may be about two. That is to say if the ^{14}C measurement has a precision of 0.4%, the 1σ uncertainty in the radiocarbon age is about 32 a and the 68% CI 1σ-equivalent width of the calendar age is about 65 a and the full width of 95% CI (±2σ full range equivalent) of the calendar age will be about 260 a. In some cases, the wiggles in the calibration curve may result in discontinuous confidence intervals and the probability distribution of the calibrated age may be bimodal or trimodal. In most cases, we have the best situation and the error of the calendar age is reduced considerably as show in Fig. 2.4. But more often, the data may fall into "wiggle platform" section and even the 1σ error could be more than 300 a as shown in Fig. 2.5. In such a situation

the high precision does not reduce uncertainty of the calendar age very much. So, generally the chronologist and/or archaeologist will not be satisfied with the radiocarbon dating.

The idea of wiggle matching was suggested quite early. In principle, if we have series of sample with certain sequence, their radiocarbon age will go up or down with curve's wiggles. So, we can fix their calendar age better by matching the group of radiocarbon ages with calibration curves.

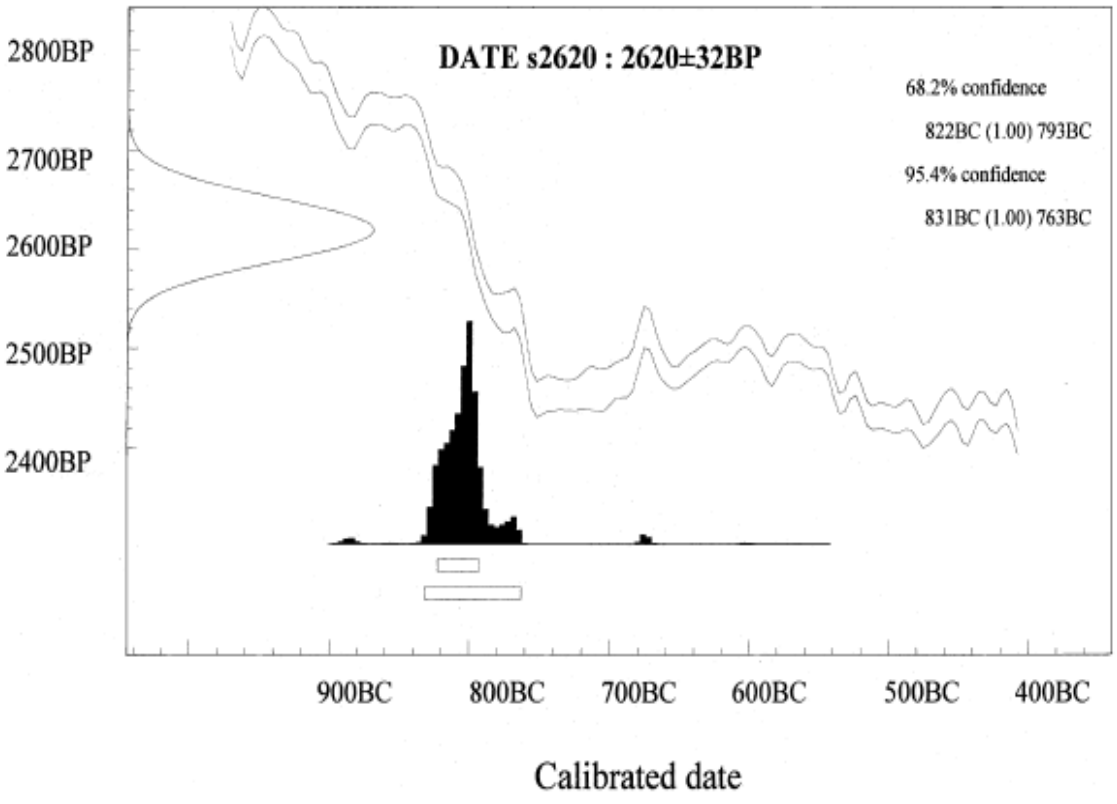

Figure 2.4: Example of calibration of radiocarbon age with small error from Xia-Shang-Zhou (Guo et.al., 2000). The calendar age is shown on the x axis, the measured radiocarbon age is represented on the y axis as Gaussian distributed variable; the calibration curve is drawn as in Figure 2.4. The distribution of probability of the calibrated age is represented; the calibrated time intervals corresponding to level of probability are also indicated and sigma 1 and 2 are represented.

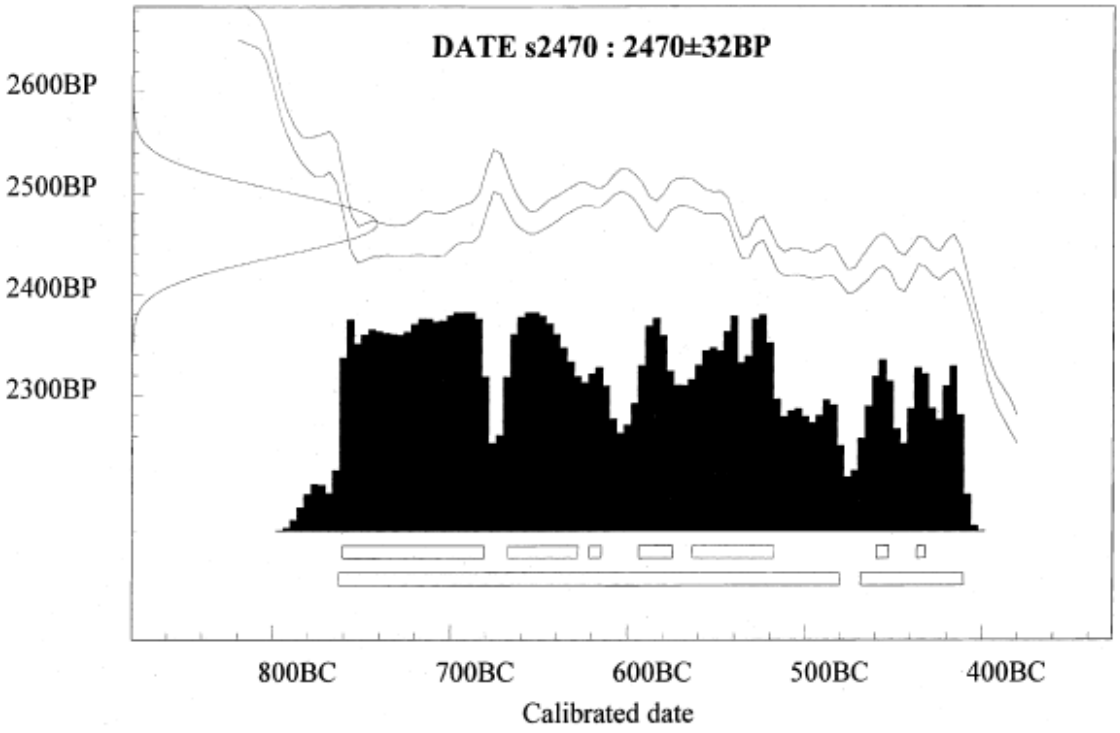

Figure 2.5: Example of calibration of radiocarbon age with large error from Xia-Shang-Zhou (Guo et.al., 2000).

CHAPTER 3
ACCELERATOR MASS SPECTROMETRY AT ITHEMBA LABS

3.1 The New 6 MV EN Tandem AMS Facility at iThemba LABS-South Africa

In 2005, the Schonland Centre for Nuclear Sciences, with its 6.0 MV EN Tandem accelerator laboratory, was donated by the University of the Witwatersrand to iThemba LABS (Laboratories for Accelerator Based Sciences). iThemba LABS is administered by the National Research Foundation (NRF) and the Department of Science and Technology (DST) of the Republic of South Africa (RSA). One of the major reasons for this transfer was the intention to establish an Accelerator Mass Spectrometry Facility, the first of its kind in South Africa and the African continent.

Understandably, refurbishment of the Tandem for its new purposes, (it was designed originally to perform nuclear physics research), involved major modifications and funding in order to become an accelerator mass spectrometry laboratory. An AMS measurement with a Tandem accelerator follows a process that in many respects is different to the traditional nuclear physics experiments or ion beam analysis (IBA) measurements performed with the same equipment. The difference lies on the sensitivity of the technique to the high performance of each individual part of a Tandem laboratory. In AMS measurements, unlike in nuclear physics, the spectrometer is not confined in a nuclear reaction chamber with a detector at the end of the accelerated beam path. The AMS spectrometer is the entire Tandem laboratory. The process starts at the heavy ion source, which produces a high quality beam of the isotopes of interest and ends at the detection station of the accelerated isotope after the ions have run a physical distance of about 50 meters and gone through a series of high-voltage electromagnetic elements of exceptional precision which constantly accelerate, steer, focus, analyze and filter

the beam. Unlike in conventional measurements, AMS requires each component of the entire spectrometer to operate reliably and within high and stringent tolerances.

In order to achieve this, major components had to be modified, upgraded or replaced keeping in mind that the major aim was to develop a system that performs high precision AMS measurements (better than ~0.5% uncertainties) with high sample throughput; the following were consider essential attributes of the refurbished system:

a) high ion beam current,
b) very high and very stable transmission,
c) high terminal voltage stability,
d) high resolution momentum analysis and
e) satisfactory isobar separation.

Consequently, the following existing components of the EN Tandem accelerator system were of major concern:

- the negative Cs-sputtering ion source,
- the accelerator tubes,
- the charging belts system,
- the high voltage column resistors,
- the terminal voltage stabilization system,
- vacuum systems throughout the spectrometer (from ion source to detector),
- the dipole bending magnets and magnetic and electrostatic and magnetic quadrupole lenses and lenses
- the energy-loss gas ionization detection systems.

3.1.1 *iThemba LABS Tandem accelerator and modified AMS system*

In developing the new AMS facility at iThemba LABS, the previously existing 6 MV EN Tandem Laboratory was heavily modified, upgraded and redesigned in order to provide the needed elements for an AMS measurement capability. The upgrade included an entirely new LE injection system, the replacement of the accelerator tubes and charging system, and the design and implementation of a new HE beam transport system including new magnetic and electrostatic isotope separation elements and a multi-anode Energy-Loss Gas Ionization Detector. Layouts of the original Tandem accelerator laboratory of iThemba LABS and the modified iThemba LABS Tandem AMS system are shown in Fig. 3.1.

The first part of the AMS system at iThemba LABS is 64-sample ion source from LLNL/CAMS, because none of existing ion sources could be used for AMS. The LLNL/CAMS ion source is followed by an Einzel lens, steerers, beam profile monitor (BPM), Electrostatic Analyzer (ESA), Faraday cup, slits, injection magnet and a preaccelerating column.

The accelerator is 6 MV EN Tandem, with accelerator tubes, and stripper canal, with Ar gas used for charge exchange of ions.

The new HE beam was installed to separate the ion beam analysis line from other existing beam lines. The HE beam line components are the following; Electrostatic Quadrupole Triplets (EQT's), BPM's, pump stations, slits, AMS bending magnet, offset Faraday cup, Magnetic Quadrupole Doublets (MQD's), ESA, Switching Magnet and detector as can be seen in Fig. 3.1.

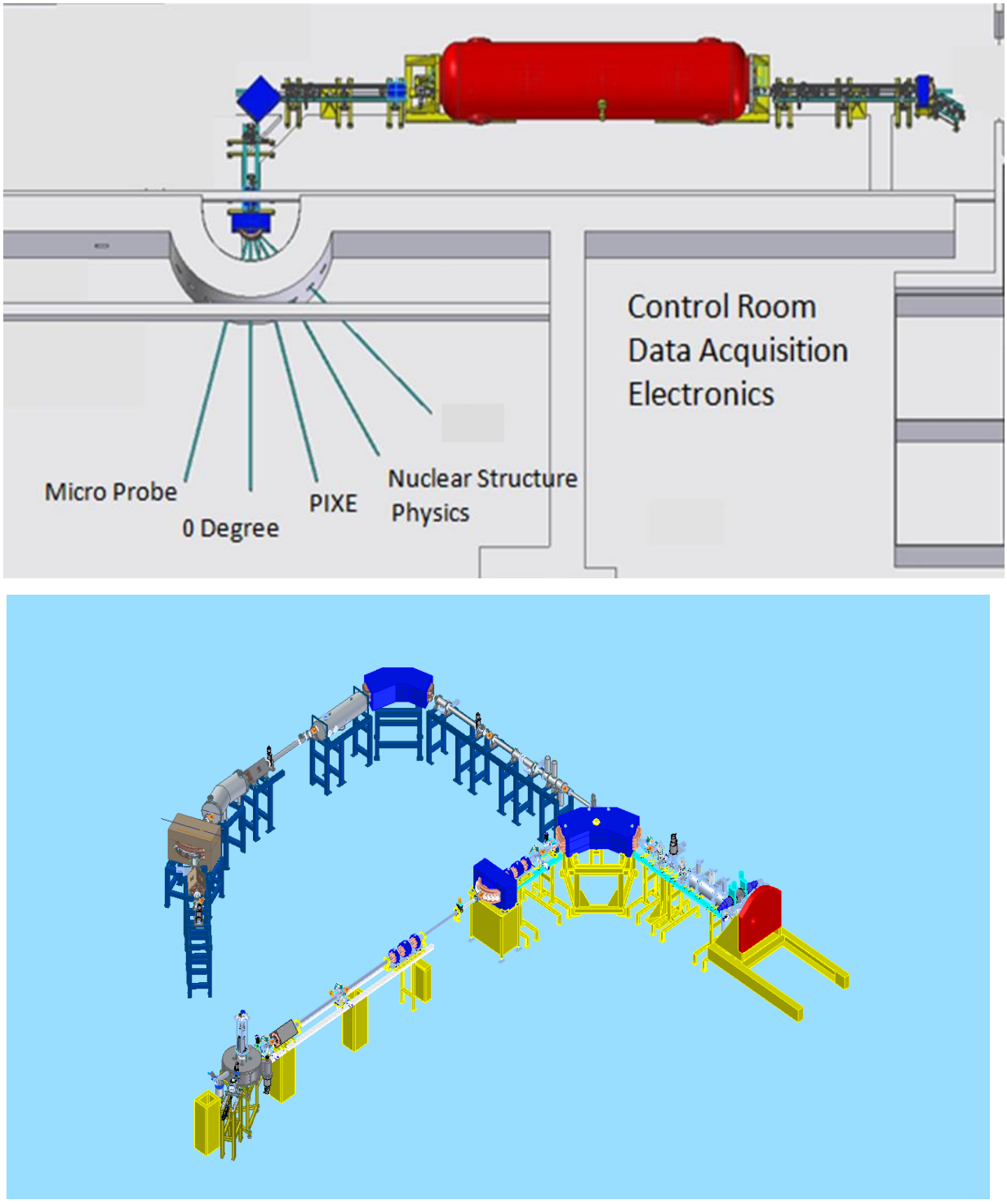

Figure 3.1: A layout of the original iThemba LABS Tandem accelerator and the modified iThemba LABS AMS facility.

3.1.1.1 *Negative Heavy Ion Cs-Sputtering Source*

For the operation of the Tandem accelerator system, negative ions of the isotopes of interest are required so that they can be injected into the Tandem and accelerated by the positive voltage on the terminal of the Tandem accelerator. For the iThemba Tandem AMS system a Cs-sputter ion source is used; within this ion source, Cs^+ ions are formed when Cs vapour is made to impinge on a hot metallic surface and the Cs^+ ions are accelerated to about 9 keV and focused onto the sample material that forms part of a cathode (Pelletron, 2014). After implanting into the sample surface Cs^+ ions lower the sample work function (due to the low Cs electronegativity), thus the emission of secondary electrons is increased; their capture by sputtered atoms (or clusters) with high electron affinity leads to the generation of negative ions. The negative ion yield depends on the electron affinities of the different elements. Higher yields of negative ions are observed for elements with a higher electron affinity and lower yields are observed for elements with a low electron affinity. The sputtering process and negative ion production is illustrated in Fig. 3.2.

Fortunately, no interfering negative isobars or isobaric molecular ions can be formed for a number of isotopes of interest to AMS because of their negative electron affinities. This is the case with ^{14}C, ^{26}Al, ^{36}Cl, $^{41}CaH^-$ and ^{129}I and their interfering corresponding stable isobaric interferences ^{14}N, ^{26}Mg, ^{36}S, $^{41}KH^-$ and ^{129}Xe, respectively. It is a fortunate fact that the life time ($\sim 5 \times 10^{-14}$ s) of negative ^{14}N ions is too short to allow it to get into the accelerator and therefore the possible ^{14}N isobaric interference is eliminated in the first stages of ^{14}C AMS measurements. ^{36}S does form and has to be suppressed using chemistry and detector/data acquisition configuration. The other important fact is that some isobars of concern like in cases like ^{36}Cl and ^{129}I are rare noble gases (i.e. ^{36}Ar and ^{129}Xe)) which are essentially not present in

the Cs-sputter ion sources. Additionally, since they generally form neither negative atomic or molecular ions, beams of such noble gases cannot be created with a Cs-sputter ion source.

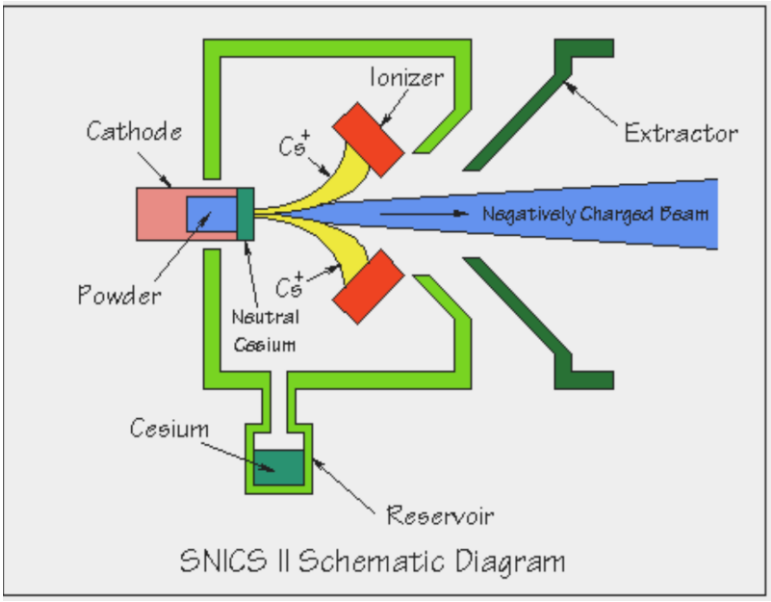

Figure 3.2: Idealized drawing of the principle operation of ion source (courtesy of National Electrostatic Corporation).

As a part of the Tandem refurbishment effort, the old single-sample 860B Cs-sputtering ion source at iThemba LABS was replaced with a new multi-cathode, high stable-current, and high-efficiency Cs-sputter ion source, which also exhibits low memory effects and includes a sample changer for fast switching between multiple samples. The following aspects, therefore, were of particular importance:

- high stable currents in order to reduce systematic errors, especially when rare and abundant species are sequentially injected and analyzed,
- negligible “memory effects” necessary to guarantee that measurements in series of samples are free of cross contamination,
- multi-cathode capability to rapidly switch the samples in order to reduce over-all measuring times,

- high ionization efficiency (the fraction of the atoms sputtered from the sample which becomes negatively charged), necessary to guarantee the ability to measure very small samples and
- better focused as well as intense cesium beam spot at the cathode, which leads to improved ion beam production with lower emittance.

Although several commercial sputtering sources for AMS applications have been developed over the years, mainly by National Electrostatics Corporation (NEC) and High Voltage-Engineering Europa (HVEE), careful review of their specifications during the present study showed that they could not match the capabilities of the source developed at Lawrence Livermore National Laboratory's (LLNL) Centre for Accelerator Mass Spectrometry (CAMS). The CAMS/LLNL source makes use of a spherical ionizer which provides inherently better Cs^+ focusing than the standard NEC, 40-sample version of the MC-SNICS is difficult to maintain, since no provision is made for in-situ servicing and entire source must be dismounted for even minor routine maintenance. The spherical ionizer caused a marked improvement in the focusing of the Cs^+ ions, leading to major gains in ion source efficiency and negative ion beam quality (low emittance) (Southon and Santos, 2007; Brown et al., 2000). Better confinement of the Cs within the ionizer assembly resulted in lower Cs consumption and, therefore, in significant reduction in arcing problems. Special care has been taken to improve the sample chamber; these improvements included proper shielding of insulators, increased high voltage gap clearances and the use of stainless steel as the construction material for the source body and sample wheel (Southon and Roberts, 2000). The vacuum in the ion source and injection lines was greatly improved by adding a Cryo-Torr 8 pump, by increasing distances between the ionizer assembly and immersion lens, and by slotting the sides of the immersion snout (Roberts et al., 2010). The improved vacuum also essentially eliminates high voltage arching within the ion source, as such arching could detrimentally effect the sensitive

electronics and computer interface modules sitting at high voltage in the source electronic racks. The improved vacuum is also a positive factor in preventing sample-to-sample memory effects. The cathode voltage in the CAMS/LLNL ion source usually operates at 5-10 kV; the extraction voltage is usually run at 40-50 kV. The insulator shields were designed to allow stable, long-term operations at higher cathode and extraction voltages and to reduce the need for frequent cleaning of the ion source due to insulator breakdowns.

The geometry and target location of the CAMS/LLNL source are optimized to place the surface of the target graphite-catalyst matrix at a position just beyond the Cs^+ focal point, which results in the sputtering being concentrated in an annular ring centered within the sample well with a less-sputtered cone in the middle of the target well (Fallon et al., 2007). The ion source's Cs oven has been placed at the shortest possible distance from the ionizer, located outside of the source vacuum body directly below the ionizer, which allows any bending of the Cs vapour-feed tube to be avoided (such bending has been a major cause of Cs clogging of vapour-feed tubes in older NEC ion source designs). In addition, the Cs vapour-feed tube actually consists of a tube running to the ionizer and an outer sleeve that terminates in the wall of the source vacuum body; the tube is heated by conduction from the Cs oven and the ionizer while the sleeve provides a vacuum insulation gap between the tube and the outer sleeve (which is exposed to surrounding cool air); this arrangement also reduces clogging of the Cs vapour-feed tube (Southon and Roberts, 2000).

The CAMS/LLNL source design is equipped with a sample wheel or a "carousel", into which up to 64 metal sample holders can be loaded for the measurement. AMS experiments require quick change between the samples, standards and blanks to minimize potential effects of machine parameter fluctuations. All samples holders within a wheel can be selected for measurement by the AMS data acquisition computer or manually by an operator. The sample wheel uses a fibre optic shaft encoder for accurate rotational indexing of the sample wheel and

a series of sequenced pneumatic cylinders for mechanical indexing of the wheel and insertion and retraction of sample holders (Roberts et al., 1994)

The CAMS\LLNL ion source is characterized by its high ion beam current of carbon beam, of about 250-300 μA (Brown et. al., 2010), which outclasses commercial designs which typically have best output ranging from 100 μA to 150 μA. In addition, the emitted negative ion beam from the CAMS/LLNL ion source has a relatively low emittance with an estimated value of ~100 π mm mrad for the 39 keV carbon beam as tested and measured at iThemba LABS on a home-made ion source test bench, as shown in Fig. 3.3. The sample-to-sample memory effects are also essentially negligible for most applications of the ion source.

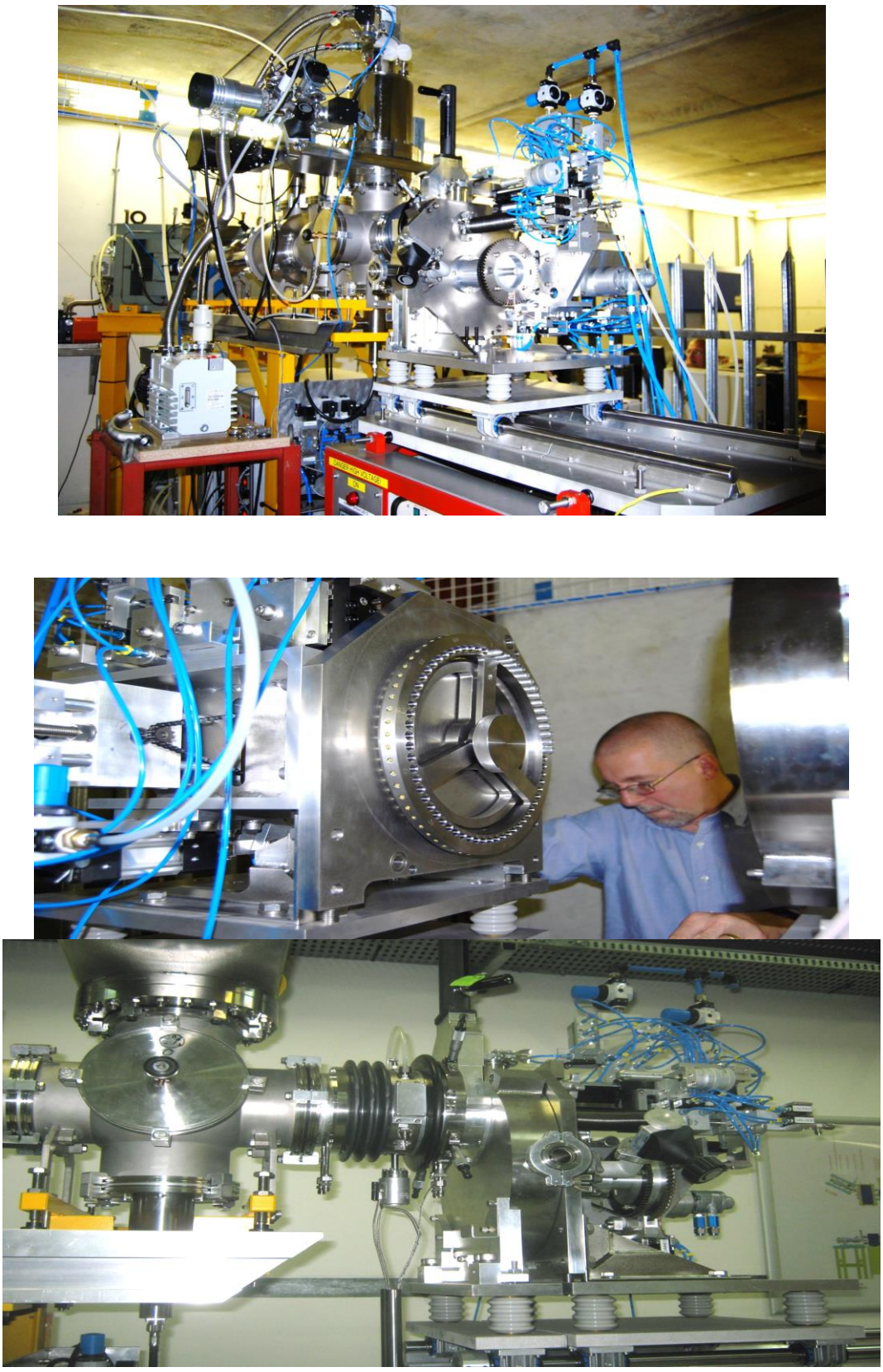

Figure 3.3: Photographs of the CAMS/LLNL ion source and during the testing of the ion source at iThemba LABS.

3.1.1.2 Lower energy injection systems for AMS

After leaving the source, the beam of negative ions/isotopes of interest, together with the interfering isobars or molecules, is transported by the LE injection system into the Tandem accelerator. Figure. 3.4 shows the LE injection system of iThemba LABS and Fig. 3.5 shows a photograph of the iThemba LABS LE injection system. In the present design, the energy of the negative ions in the LE injection system is about 50 keV as defined by the extraction voltage of the ion source of about 50 kV.

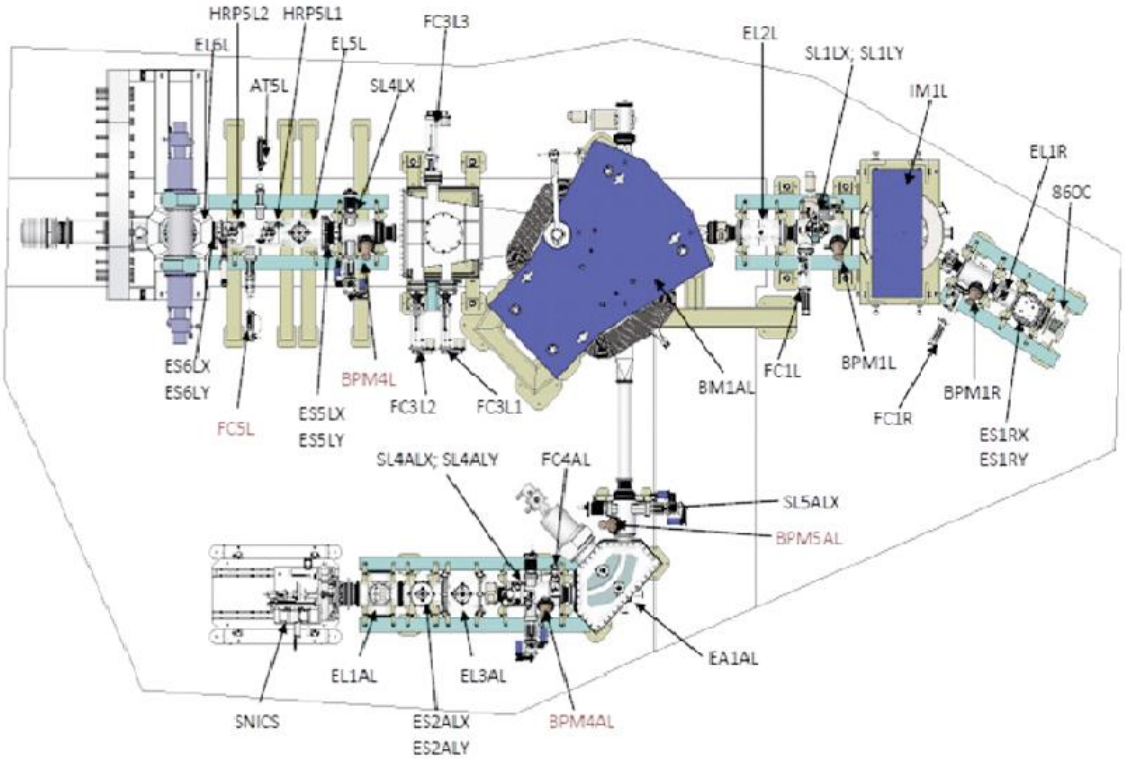

Figure 3.4: The injection system for 6 MV Tandem accelerator at iThemba LABS.

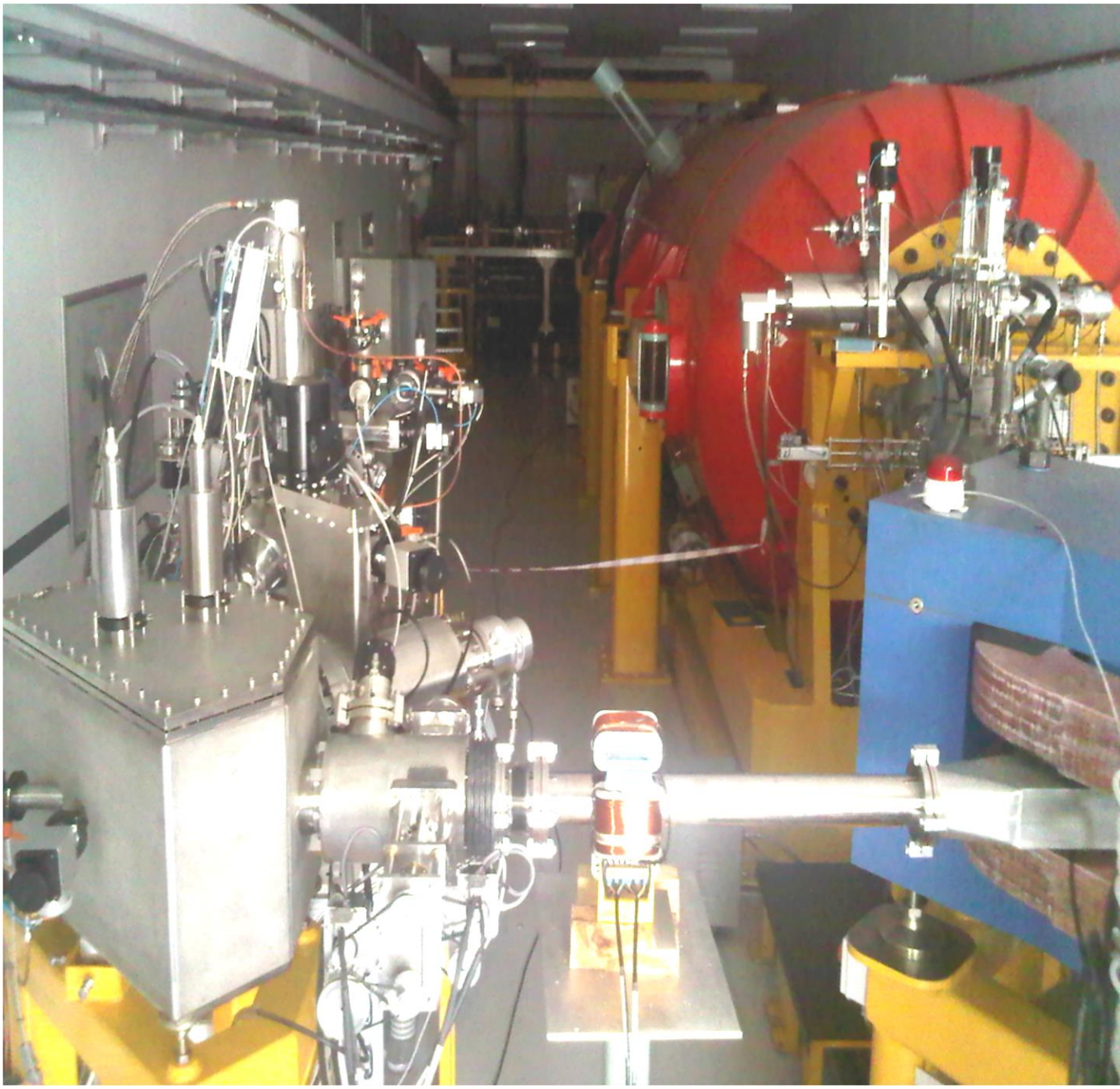

Figure 3.5: A photograph of injection system for 6 MV Tandem accelerator at iThemba LABS.

The main “characteristics”, some of which would be the equipment items and some of which would be the performance ideals of the LE injection system are the following:

- designed to keep the beam envelope as sufficiently small to allow 100% transport of the ions throughout the system,
- designed to perform sufficient mass and energy analyzes of the transported ions to allow selection of the ions of interest and to eliminate interferences to the degree possible at the low energies of ions in the system,
- incorporates a 90° bending magnet that has a radius of curvature of 608 mm and a mass-energy product of 15.6 MeV amu and
- incorporates a 90° spherical electrostatic analyzer that has a bending radius of 306 mm and an energy/charge ratio of 90 keV.

In order to ensure high mass as well as high energy resolution, the new LE injection system incorporates a magnetic analyzer for momentum analysis and also an Electrostatic Analyzer (ESA) for energy analysis as its major components. The system also includes additional electrostatic elements, such as Einzel lenses and steerers, for focusing and steering the ion beam. The new LE system is of the sequential injection type i.e. during AMS measurements ions of the rare isotope of interest and of the stable normalization isotope are injected into the Tandem in an alternating sequence. This sequential injection of isotopes allows the determination of rare isotope detector counts to stable isotope current ratio which, amongst other attributes, allows for the normalization of the measured rare isotope ion counts to a monitor of ion source output. In order to ensure injection of the highest possible quality and transmission, special care was taken with the main equipment:

An ESA is placed after the ion source with 90° bend and a radius of 306 mm. This optical element is of the spherical type in order to have double-focusing properties, as the spherical electrodes provide focusing in both the horizontal and vertical directions. The ESA is followed by a double focusing 90° bending magnet that has a radius of curvature of 608 mm and a mass-energy product of 15.6 MeV amu. The high energy-resolution ESA and high mass resolution bending magnet are required in order to deal with one of the disadvantages of the Cs sputter ion source, that is, the high-energy tail of the ion beam produced (Hellborg and Skog, 2008). Energy from the energetic Cs^+ ions can be transferred to the negative ions leading to a high energy tail (Litherland, 1984). This effect is significantly less pronounced for high intensity sources like CAMS/LLNL source operating with low Cs energies of only 5-10 keV. Tails toward lower energies can be obtained from unstable molecules. Those that decay in the extraction field lead to a continuum and those decaying after the extraction field lead to discrete peaks in the spectrum (Suter, 1990). These tails can cause serious interference/background problems, especially for the detection of heavier isotopes for which the relative mass differences are smaller.

The placement of the ESA before the injection magnet (as shown in Fig. 3.4) allows the use of the energy dispersive characteristics of the ESA and appropriately placed adjustable slits to cut off much, if not effectively all, of these higher and lower energy tails. In, fact, the combination of the ESA and the following high mass-resolution bending magnet makes the total LE system achromatic, that is non-dispersive energy for ions transport from the ion source to beam image/waist position of the LE magnet. Since ions with lower than desired mass that are part of the high energy tail may end up with the same magnetic rigidity as the ions of interest (and vice versa for ion with higher than desired mass that are part of the low energy tail) both the energy resolution of the ESA and the magnetic rigidity resolution of the injection magnet are essential features of the injector. Because of this high/low energy tail elimination, the

installation of the ESA as a part of the AMS LE injection has particular advantages for the measurements of actinides at iThemba LABS. In addition, the 90° bends of both the injection magnet and the ESA provide for a U-shaped injection system whose dimensions were particularly advantageous in terms of space issues at the LE end of the accelerator hall.

As mentioned above, a LE mass analysis magnet is placed after the ESA; this magnet has high mass-resolution by being double focusing, with a 90° deflection angle and a large radius of curvature. The large pole gap of the magnet ensures excellent flat top transmission and the magnet vacuum box exit is wide enough to allow simultaneous off-axis transmission of stable isotopes even when the rare isotope is being transmitted on the central axis. This wide exit vacuum box allowed for two off-axis Faraday cups to be installed in positions that allow the measurement of off-axis ion beam currents at the output of the magnet; in the case of ^{14}C measurements, the $^{12}C^-$ ion current can be measured on one of these LE off-axis Faraday cups when the $^{14}C^-$ beam is being injected into the Tandem. When the LE magnet and ESA are set to transport and inject mass 14 ions with the desired energy (about 50 KeV from the extraction potential of the ion source) into the accelerator, atomic and/or molecular ions of different masses are eliminated from the injected ion beam. In terms of the required beam line elements of the HE part of the iThemba AMS system, it is important to recognize that when set to inject $^{14}C^-$ ions the LE injection system will also inject mass 14 molecular ions, that are produced in the ion source, such as $^{12}CH_2^-$ and $^{13}CH^-$.

Electrostatic Analyzer

The ESA consists of two spherical-section electrodes which are a distance d = 50 mm apart. Figure. 3.6 shows the ESA and the two Einzel lenses (between ion source and the ESA of the LE section) of the iThemba LABS AMS system. The applied potential ΔK between the

electrodes is of the order of 16 kV forcing the nominal beams to follow a circular trajectory of the central radius of curvature of the ESA, r_0 =306 mm. The electrodes extend over the angle φ = 90º; a 1:1 imaging can be achieved for an object at r_0 tan (φ/2) distance (= r_0 for φ = 90º) before the entrance, with the corresponding image at the same distance after the exit. The ESA acts as an energy filter based on an-*E/q* analysis:

$$\frac{E}{q} = \frac{\Delta K r_0}{2d} \tag{3.1}$$

where E is the electric field between the ESA plates, q is the equilibrium charge state, K is the voltage difference between electrodes and d is distance between the ESA plates. Subsequently, it can be derived that ions with small relative energy deviation *ΔE/E* obtain a spatial separation of (Steier, 2000)

$$\Delta x = r_0 \frac{\Delta E}{E} \tag{3.2}$$

at the image position which can be sufficient for the removal of much of the energy tailing from the sputtering source before magnetic analysis and injection into the Tandem accelerator.

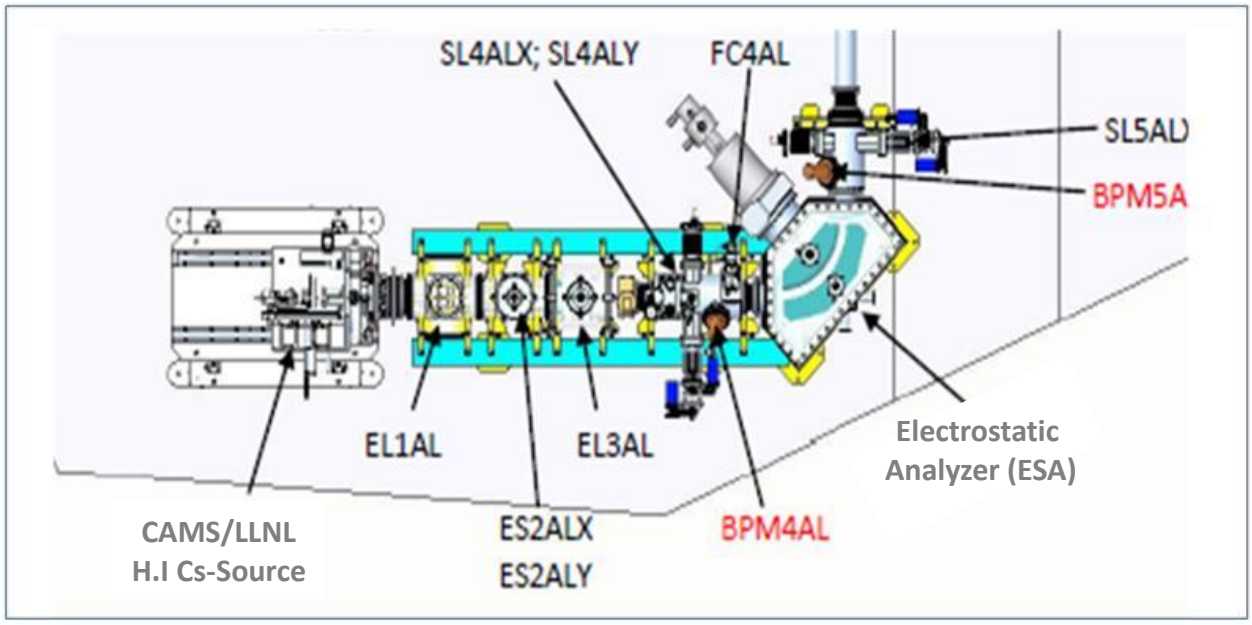

Figure 3.6: The set of two Einzel lenses (EL1AL and EL3AL) and the Electrostatic Analyzer (ESA) setup after the CAMS/LLNL source. ES2ALX/Y are horizontal (H) electrostatic steerers and vertical (V) electrostatic steerers, SL4LX/Y are adjustable H and V beam limiting slits,BPM4AL and BPM5AL are beam profile monitors and FC4AL is the faraday cup to monitor the current.

Einzel lenses

An Einzel lens is an axially symmetric ion optical element, and it is the main tool for beam focusing in many electrostatic injection systems. The four Einzel lenses in the iThemba LABS LE injection system are each comprised of two gap lenses combined into one cylindrical three-electrode system with the first and last electrodes at the beamline (ground) potential U_1 and the center electrode at a different potential U_0. The first two Einzel lenses are located immediately after the ion source and their geometry is chosen in such a way as to act as a zoom telescope for the nearly-arbitrary placement of a beam waist before the 90° ESA. The other two Einzel lenses are located just before the entrance of the Tandem and are used to focus the beam into the Tandem accelerator.

L.E. Faraday cups for stable isotope measurements

In addition to the various Faraday cups at different positions along the beamline used for tuning the beam, two faraday cups have been installed immediately after the 90° LE magnet in order to measure the ^{12}C and ^{13}C isotopes at low energy before acceleration. Although the designed AMS system sequentially injects ^{12}C, ^{13}C and ^{14}C, with both being measured after acceleration and analysis (^{13}C with a Faraday cup after the first 90º HE magnet and ^{14}C with gas ionization detector at the end of the AMS beamline), the system also allows ^{13}C to be measured at the LE end. If transmission of ^{14}C and ^{13}C ions through the Tandem and HE end is stable and consistent, then LE measurement of $^{13}C^-$ might be useful, but that would have to be checked through a series of measurements (the "mass 12" current is overwhelmingly $^{12}C^-$ – there is no $^{11}CH^-$ to interfere with the $^{12}C^-$ measurement). FC5L is the Faraday cup that is used for tuning a beam down the center of the beamline (i.e., setting up the beam for injection into the Tandem). Fig. 3.7 shows the bending magnet, Einzel lenses and Faraday cups in the LE injection system. Fig. 3.8 is the photograph of the LE Tandem accelerator of iThemba LABS AMS system.

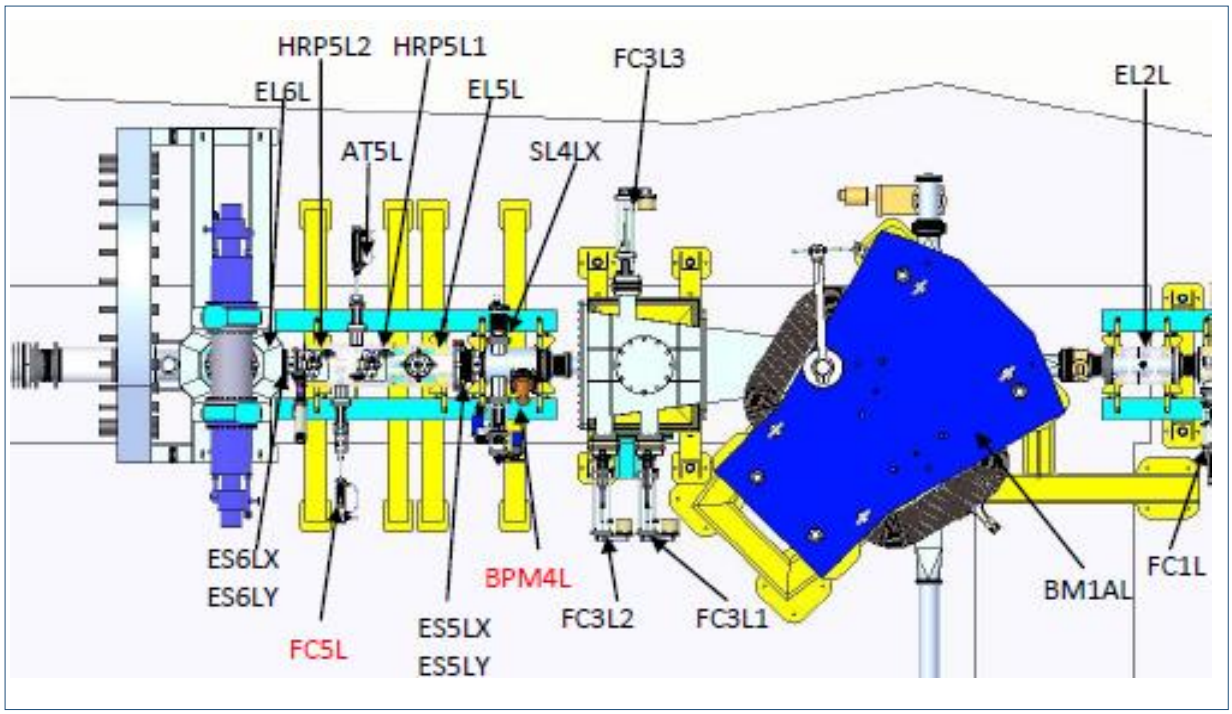

Figure 3.7: A schematic layout of the LE bending magnet together with the Faraday cups and the Einzel lenses before the entrance into the Tandem.

Figure 3.8: A photograph of the LE Tandem accelerator at iThemba LABS.

Bending magnet

One of the most significant improvements over the previous LE injection system is the introduction of the large double-focusing magnet replacing the old single-focusing injection magnet, which was undesirable because it had a small pole gap had poor mass resolution (due to its small bending angle of only 30° and small bending radius) and the fact that it focused only in the bending plane. The new 90° bending magnet has a 608 mm bend radius, a mass energy product of 15.6 MeV amu, and a significantly larger 94 mm pole gap. The entry and exit pole face angles are 30° and 28°, respectively; these pole-face angles provide the vertical focusing required for the double-focusing properties of the magnet. The double-focusing properties of the magnet are shown by the orange colored ion trajectories from ray trace calculations in Fig. 3.9. The magnet's mass-energy product for charge 1 is quoted as ME/q^2 = 15.6 MeV amu (where M is the mass, E is the kinetic energy, and q is the charge) which provides an upper limit on the capabilities of the magnet. This mass-energy product implies that the magnet will be able to bend 60 keV singly-charge ions of masses up to 260 amu along the central axis of the magnet, which is needed for actinides AMS measurements.

The bending magnet acts as a filter for "momentum divided by charge" and at a particular magnetic field setting, B, the magnet rigidity of the ions that will be properly transported by the magnet is given by:

$$B\mathrm{r}_0 = \frac{\sqrt{2mE}}{\mathrm{q}} \tag{3.3}$$

where m is the mass of the ion, E is the energy of the ion, q is the charge of the ion and r_0 is the radius of curvature of the magnet bend. At this field, the ions of interest will follow the central radius of curvature of the magnet, while heavier masses will curve less and lighter masses will curve more. The horizontal spatial separation achieved at the beam waist at the

image position downstream of the magnet for small relative energy differences, ΔE, or mass differences, Δm, is given by (Steier, 2000):

$$\Delta x = 2r_0\left(\frac{\Delta E}{E} + \frac{\Delta m}{m}\right) \tag{3.4}$$

The focusing properties of the magnet depend on the angles at which the beam enters and exits the pole faces (Septier, 1980). For a given magnet with bending angle φ = 90°, symmetrical pole-face angles of $\tan^{-1}$ (1/2) supply symmetric 1:1 focusing from an image position $2r_0$ before the entrance to a symmetrical position after the exit (Steier, 2000). In the case of the iThemba LABS LE bending magnet the pole faces are 30° and 28° for the entrance and exit faces, respectively. The object and images distance of the iThemba LABS LE bending magnet are 1181.9 mm and 1197.9 mm, respectively. It is worth noting that the $\tan^{-1}$(1/2) pole face angles (26.6°) for symmetric 1:1 focusing at an image position of $2r_0$ are for an idealized magnet with a zero mm pole-face gap. As indicated by the values obtained for the iThemba LABS LE bending magnet, for real-world relatively large-gap magnets pole-face angles tend to be around 29° and object/image distances tend to be around $2.25r_0$.

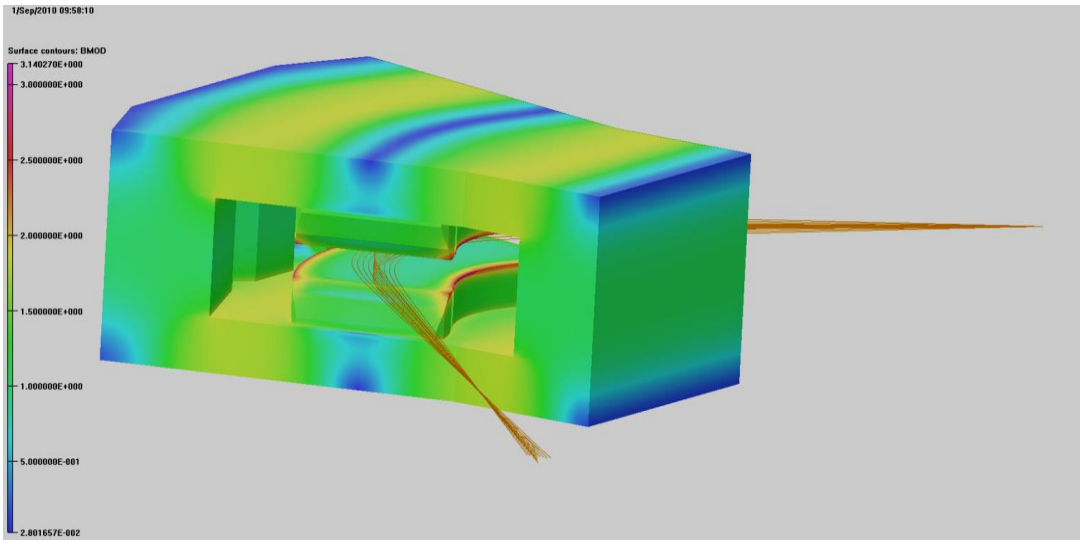

Figure 3.9: Vector Fields Ray Trace calculations illustrating the beam envelope around the LE Bending magnet for 6 MV Tandem accelerator at iThemba LABS(Gauteng).

3.1.1.3 *The 6 MV EN Tandem accelerator for AMS*

The EN Tandem accelerator is characterized by a two stage acceleration process. In the first LE stage, the negative ions (that were generated in the ion source and transported to the accelerator by the LE injection system) are accelerated towards the central terminal of the Tandem through a series of electric field gradients defined inside two horizontal end-to-end evacuated glass accelerator beam tubes (the LE beam tubes) which are composed of glass insulator rings sandwiched between metal electrodes. The outer accelerator housing is a large (1030 cm long by 185 cm in diameter) steel tank that is pressurized to 18 bar with an insulating gas mixture of 80% N_2 and 20% CO_2. An insulating support column runs horizontally through the center of tank; this insulating column supports the accelerator tubes, the central high voltage terminal and other accelerator components. Similar to the accelerator beam tubes, the column is composed of glass insulator sections sandwiched between metal plates with each glass section of the column corresponding to a glass insulator ring of the beam tubes. The

corresponding column planes and accelerator tube rings are electrically connected and high value resistors connect each column plane to the two adjacent planes. This resistor-chain arrangement of planes and resistors provides a smooth, controlled potential gradient throughout the accelerator beam tubes from the high voltage terminal to the end of the LE accelerator tubes grounded at the LE tank wall.

The EN Tandem accelerator is operated, as are all tandem accelerators, with a positive high voltage on the central terminal. In the refurbished iThemba LABS EN Tandem, a pelletron charging system transports and deposits charge onto the central terminal at a rate that allows the terminal potential to be raised to up to a maximum of about +6.5 MV. This positive voltage on the central terminal causes a potential gradient throughout the LE beam tubes, and in this gradient the injected singly-charged negative ions are accelerated to the central terminal; the ions gain an energy that is equal to their charge (1) times the terminal voltage i.e. for a terminal voltage of 5 MV, the negative ions reach the terminal with an energy of 5 MeV. At the central terminal, the incoming energetic negative ions pass through an atomic collision cell (the Tandem accelerator's "stripper canal") in which a constant pressure of gas molecules is maintained with high purity Ar. While passing through the stripper canal, the energetic ions interact with the "stripper" gas molecules and in those interactions one or more electrons are "stripped" off of the energetic ions. In this way most of the energetic ions are converted to positive ions, whose charge multiplicity depends on the number of electrons that have been stripped off.

The distribution of the stripped incident energetic ions into the various possible positive ion charge states is a function of the energy of the incoming energetic negative ions and, therefore, depends on the terminal voltage at which the Tandem is being run. The charge state distribution is also dependent on the thickness of the stripper gas or foil (in the case of gas the

thickness is related to the pressure in the stripper canal and the length of the canal). If the stripper is sufficiently thick, the electron stripping and recombination processes reach an equilibrium state and the charge state distributions are essentially stable above that stripper thickness; typical equilibrium stripper thicknesses are 1.2-1.6 µg/cm^2 over the range of terminal voltages accessible to the iThemba LABS EN Tandem accelerator. Figure. 3.10 shows the equilibrium 3^+ and 4^+ charge state fractions as a function of incident C ion energy for three different stripper media, Ar gas, O_2 gas and a thin carbon foil (C-foil). At lower ion energies of about 3 MeV, the highest charge state fractions (up to about 55%) are obtained using Ar or C-foil as the stripping media. At higher ion energies of about 6.5 MeV, the highest charge state fractions (60-70%) are obtained using any of the three media, with Ar producing the highest charge state fraction of about 70% across the 5.5 to 7.5 MeV energy range.

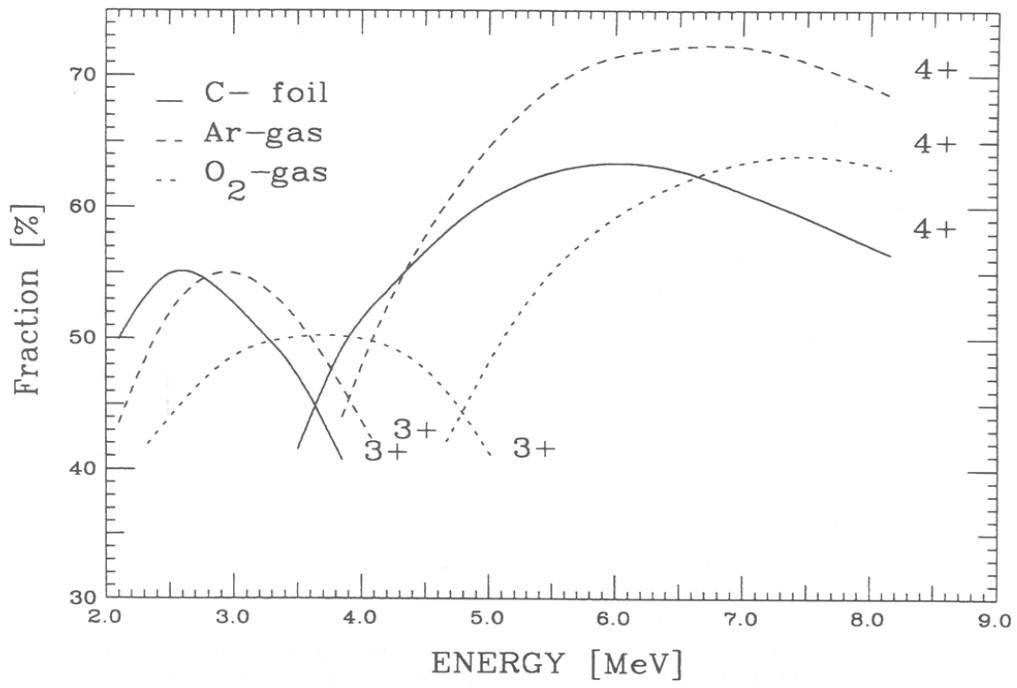

Figure 3.10: The stripping fractions are plotted as a function of incident C^- ion energies for various stripper media. Charge state fractions for 3+ and 4+ ions after stripping in O_2 gas (dotted line), Ar gas (dashed line) and carbon foil (solid line) are shown (Suter et al., 1990).

One of the advantageous attributes of tandem accelerators in AMS measurements is that the stripping process suppresses interferences due to isobaric molecules. During the interactions between the energetic incident ions and the atoms/molecules of the stripper media potentially interfering isobaric molecular species are stripped of some number of electron and the produced molecular ions are unstable and dissociate. For example, in the case of $^{14}C^-$ AMS measurements, the mass-14, $^{13}CH^-$ and $^{12}CH_2^-$ molecular ions (that are injected with the desired $^{14}C^-$ ions) tend to break up during the stripping process. The effectiveness of this molecular ion dissociation process is dependent on the incident ion energy, the thickness of the stripper media and the selected positive ion charge state.

Molecular ions that are stripped to charges states $\geq 3+$ are not stable and dissociate; this leads to AMS facilities that are able to run at terminal voltages in the range of 5-7 MV preferring to make ^{14}C measurement using the 4+ charge state (in addition, as shown in Fig. 3.10, this tends to produce the highest charge state fractions). In the case of AMS facilities that are able to run at terminal voltages in the range of 2-3.5 MV, 3+ tends to be the preferred charge state for ^{14}C measurements. For smaller AMS facilities that run at accelerating voltages of a few 100s of kV and select the 1+ charge state, a significant fraction of the $^{13}CH^-$ molecular ions will survive the stripping process if the stripper gas pressure is operated at the setting for the peak $^{14}C^{1+}$ production efficiency, and this leads to unacceptably high background count rates in the detector. By setting the stripper gas pressure somewhat higher than the setting for peak-peak $^{14}C^{1+}$ production efficiency, the significantly thicker stripper gas and the finite probability of the break-up of molecules with bound states in charge state 1^+ during molecular ion-gas molecule interactions leads to the suppression of the $^{13}CH^-$ molecular ion contribution to measurement backgrounds (Synal et. al., 2000; Suter et. al., 2000; Suter et. al., 1997).

After passing through the stripper canal, the now positive energetic ions enter the HE beam tubes. The HE beam tubes are almost identically constructed as the LE beam tubes and the tubes/column structures are essentially identical; as with the LE tubes/column/resistors the resistor-chain arrangement on the HE tubes/column provides a smooth, controlled potential gradient throughout the accelerator beam tubes from the high voltage terminal to the end of the accelerator tubes grounded at the HE tank wall (at the opposite end of the tank from the LE tank wall). On entering the HE beam tubes, the now positive energetic ions are accelerated away from the central terminal towards the grounded end of the HE accelerator tubes and exit the accelerator at the HE tank wall. In being accelerated by the potential gradient the now positive ions gain an energy that is equal to their charge state, q, times the terminal voltage; i.e., for a terminal voltage of 5 MV and a positive ion in charge state 4+, the ion will gain an energy of 20 MeV.

The now positive energetic ions exit the accelerator having gone through two stages of acceleration, firstly as a singly charged negative ion and secondly as a multiply charged positively ion; this two stage acceleration process is why these types of accelerators are called "tandem" accelerators. For a tandem accelerator being operated at a terminal voltage V_T, positive energetic ions in charge state q exit the accelerator having gained energies of 1e times V_T for the acceleration as a negative ion and qe times V_T for the acceleration as a positive ion, for a total energy for the positive ion at the exit of the accelerator of $(1+q)V_T$. Table 3.1 below shows the energies of exiting accelerated $^{14}C^{4+}$ and $^{14}C^{3+}$ ions for the terminal voltages that are normally accessible using the iThemba EN Tandem accelerator. In conducting AMS measurements, the energy that is imparted to the ions of interest is important in that this energy has allowed the application of nuclear physics instrumentation and methods to filter out interfering ion species such as atomic or molecular isobars, ions that obtained similar magnetic rigidity through scattering or charge exchange interactions with residual gas atoms/molecules

in the beam transport elements of the system, or ions that physically scatter off beam transport elements such as slits and vacuum box walls.

Table 3.1: Typical terminal voltages for $^{14}C^{4+}$ and $^{14}C^{3+}$ ions.

Terminal Voltage(MV)	Energy $^{14}C^{4+}$(MeV)	Energy $^{14}C^{3+}$(MeV)
2	10	8
2.5	12	9.5
3	14	11
3.3	15.2	11.9
3.5	16	12.5
4	18	14
4.5	20	15.5
5	22	17
5.5	24	18.5
6	26	20

Central Terminal Gas Stripper

As discussed above, the terminal of the iThemba LABS Tandem accelerator is equipped with a gas stripper canal in which electrons are stripped from the incoming negative ions, resulting in positive ions that exit the accelerator with an energy of $(q+1)V_T$. The advantages of gas stripping over foil stripping include that the gas can be continually replenished and that the thickness of stripping medium can be adjusted during operation to achieve optimal efficiency for any given desired ion charge state and terminal voltage combination. Disadvantages of foil stripping include that the commonly used carbon foils are usually quite fragile, that the foils often have to be carefully chosen to have the correct thickness for given application, and that foils have a limited lifetime and may have non-linear aging properties as the foils are exposed to energetic ions during the stripping process. The disadvantages of gas stripping are a lower beam transmission and a lower mean charge state of the positive beam at a given terminal voltage.

By considering of these advantages and disadvantages which leads to the decision for iThemba LABS to opt for gas stripper and it is combined with terminal pumping. The major decision not to consider foil stripper is fact that foil stripper is applicable for light ions as the lifetime of the foils is too short for heavy ions.

As a part of the refurbishment of the iThemba EN Tandem accelerator, the terminal stripper canal system was upgraded by incorporating a stripper gas recirculation system that included a high vacuum turbo pump in the terminal. The stripper gas system operates by leaking gas into the stripper canal through a tube connected to the middle of the canal; the gas then passes out the ends of the canal with a concentration of the gas being maintained in the stripper canal through conduction limitations on the passage of the gas from the entry point to the ends of the canal. Before the upgrade, the introduced stripper gas would pass from the ends

of the canal into the accelerator tubes. The presence of the gas in the stripper tubes was detrimental to the operation of the accelerator for several reasons, the most significant being the decreases in ion transmission caused by the interactions of the accelerated ions with the gas molecules in the tubes. With the installation of the stripper gas recirculation system, a set of baffles restrict the flow of stripper gas into the tubes and the terminal turbo pump is used to recirculate the stripper gas leaving the stripper canal back into the gas handling system that supplies gas to the input of the stripper canal. The stripper gas recirculation system allows operations with higher gas pressures in the stripper canal (which can be advantageous for some AMS measurements) while maintaining high vacuum in the acceleration tubes (which reduces collision and charge-exchange induced beam transport losses). Another important new feature of the stripper canal is that the gas tube has a larger diameter of about 10.5 cm for better beam transmission as compared to the previous smaller diameter stripper canal. The advantages of the new stripper system compared to the old one is that a higher beam current can be transported through the accelerator, the ion beam exiting the accelerator has better characteristics for transport through the rest of the AMS system, and the Tandem generally operates more stably.

Terminal Voltage Stability

AMS requires the smallest possible momentum and/or energy variations in the ions of interest at the exit of the accelerator in order to ensure transport of the desired ions to the detector and minimize interferences in the detector. Hence, the stability of the voltage on the central terminal of the Tandem accelerator is of paramount importance. A major limitation on the terminal voltage stability of the EN Tandem at iThemba LABS was that the old system used to transfer charge to the terminal was of the original Van de Graaff generator charging belt type. There are a variety of inherent problems with such charging belt systems; one of the most prominent of which is that the belt edges can end up flapping about causing charge transfer variations, directly causing terminal voltage instabilities. As a part of the

refurbishment, the charging system was changed from the belt-charging system to a Pelletron charging system. A Pelletron charging system is based around a chain consisting of alternate insulating and conducting segments; this chain provides a more uniform and consistent charge transport structure than was typically provided by conventional charging belts. The Pelletron charging system transfers charge to and from the Pelletron chain through induction rather than having the transfer of charge depend on physical contact as the belt moves under high voltage charging screens and/or shim stock. Continuous and consistent contact between the charging screens and the belt was difficult to maintain, and the terminal voltage stability of tandems with belt charging system has generally been inferior to that of tandems with Pelletron charging system. In addition, the Pelletron chain does not produce the lint and dust that a charging belt does; this reduces unnecessary electrical sparking between components within the accelerator. In addition, the Pelletron chain is considerably less sensitive to moisture, and the insulating segments of the chain can be intrinsically protected from spark damage by careful design of the conducting segments. The HE ground end of Pelletron charging system now installed in the iThemba LABS Tandem accelerator is shown in Fig. 3.11.

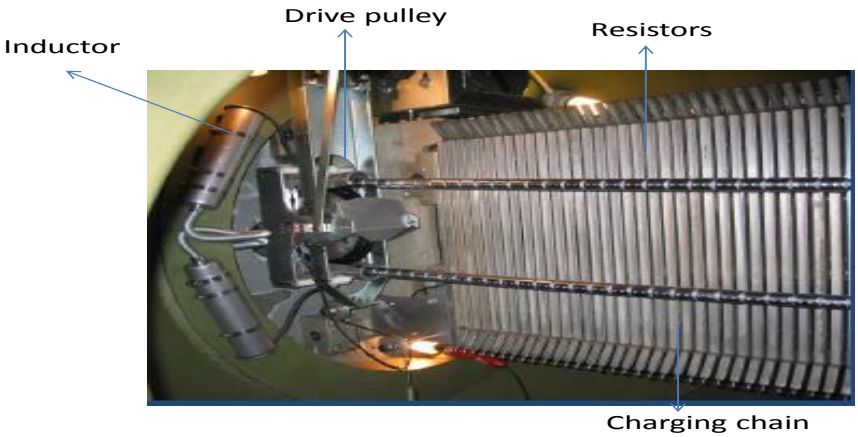

Figure 3.11: The Pelletron charging chain of iThemba LABS.

The terminal voltage of the accelerator is stabilized by using a refurbished Generating Voltmeter (GVM) and two Capacitive Pick-Up plate as voltage sensors, and a new NEC Terminal Potential Stabilization (TPS) system (that controls a conventional corona probe assembly), that was purchased and installed as part of the refurbishment of the iThemba LABS Tandem accelerator. The TPS is used to correct for low frequency variations in the transfer of charge to the terminal by the Pelletron charging system that would otherwise appear as large (1-10 kV), low frequency fluctuations in the terminal voltage. The GVM signal is primarily used to maintain the dc terminal voltage. The CPU provides an ac error signal that reduces higher frequency fluctuations in the terminal voltage.

In order to further improve voltage stability and reduce sparking, the set of four old accelerator tubes installed at Schonland Research Centre in 1971 (which were manufactured by High Voltage Engineering Corporation (Schonland, 1971)), and which had vertically inclined electrodes for electron suppression) were replaced by a set of four new HVEE accelerator tubes (which feature a high-voltage sparks gap and have a "Q-snout" electrode arrangement at the LE entrance to the tubes). The HVEE tubes are characterized by axial electric fields and have spiraling magnetic fields for electron suppression. As with the original tubes, electrode planes of the new HVEE accelerator tubes are directly connected to corresponding planes of the column, and high-value resistors between the planes of the column provide a smooth, controlled potential gradient throughout the accelerator beam tubes. Fig. 3.12 shows a section of the column and resistors of the 6 MV iThemba LABS EN Tandem accelerator.

Figure 3.12: Resistors inside the tank of 6 MV Tandem accelerator at iThemba LABS.

The old column "resistors" allow "controlled" current flow by corona-discharge across adjustable gaps. This corona-discharge based system had inherent stability disadvantages related to poor gap-gap voltage homogeneity and very low grading currents. As a part of the Tandem refurbishment, high-voltage grading resistors and resistor mounts were installed. There is no corona-discharge current with new resistor structures; these are real resistors which provide stable and well-characterized current conduction pathways and create and sustain a stable and essentially uniform electric potential gradient along the column sections of the Tandem accelerator. Such high-voltage grading resistors and resistor mounts have operated stably in other Tandem accelerators for periods measured in decades. The new resistors and mounts have resulted in more stable Tandem operation with improved beam transmission, and have allowed operation at terminal voltages as low as 1 MV, which is required for some nuclear physics experiments.

The operating characteristics of the iThemba LABS Tandem accelerator have shown an overall improvement from 4.2 to 5.4 MV in reliable operating capability during the five-

year period since the refurbishment. The iThemba LABS Tandem accelerator achieve stability and reliability and provide advanced computer control. At present, routine operation of an EN Tandem accelerator for research in the vicinity of 6.5 MV seems quite far-fetched; however, the iThemba LABS planned for installation of 80-100% SF_6 which is going to give much better performance of the accelerator at 6.5 MV. The ion beam analysis (IBA) and nuclear physics research were used for a long time at iThemba LABS on dedicated 6 MV EN Tandem accelerator beamlines. Currently good measurements were obtained on IBA, nuclear physics and AMS.

3.1.1.4 *HE AMS system*

As a part of the iThemba LABS Tandem accelerator refurbishment many components of the HE beam lines were replaced and a new HE AMS system was installed. The new HE AMS system was designed to fulfill the relevant essential attributes that were listed at the beginning of this chapter i.e. the system was designed such that its beam transport optics provide a well understood and controlled ion beam envelope that guarantees high and stable transmission of the desired ions throughout the system, high momentum-resolution and energy analysis, and good isobar separation at the detector. The major components of the new HE AMS system are a high mass-resolution, large radius, large pole gap 90^o bending magnet ($M/\Delta M$ ~725), a 22.5^o bend high energy cylindrical ESA, an AMS switching magnet and an Energy-Loss Gas Ionization detector. The system incorporates other elements that are used to control the transport of the desired ions throughout the system, such as sets of electrostatic steerers, electric quadrupole triplets and magnetic quadrupole doublets. Figure 3.13 shows the new HE AMS system of the iThemba LABS Tandem accelerator.

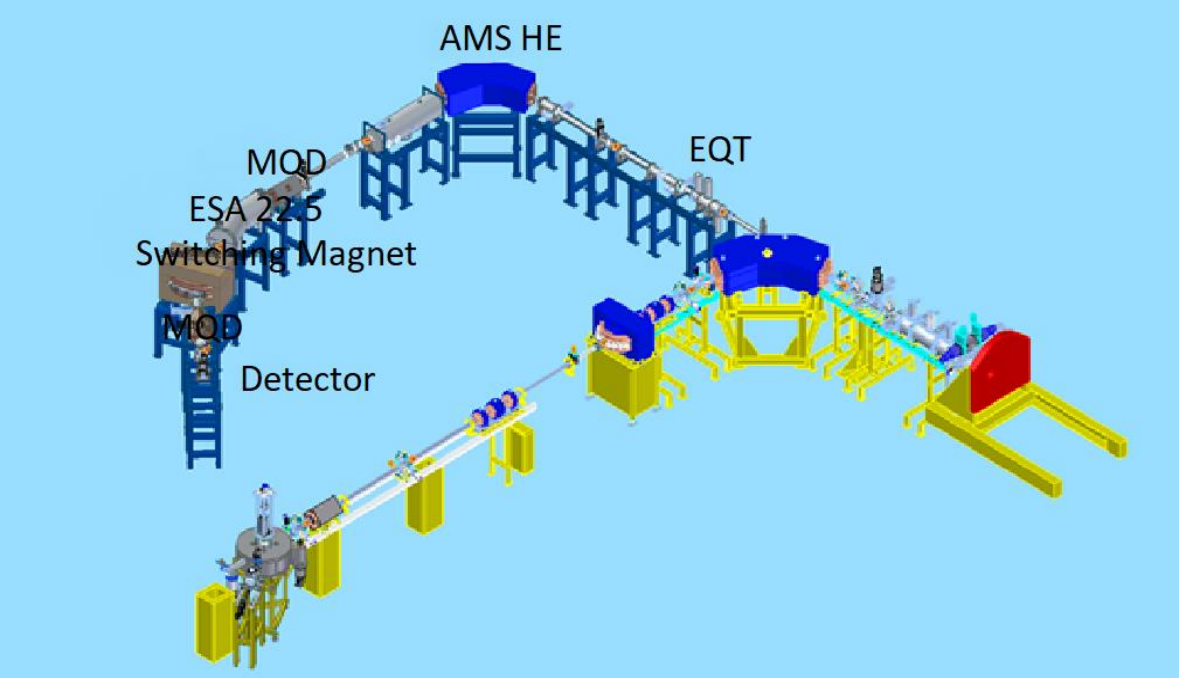

Figure 3.13: High energy AMS system of iThemba LABS.

Electrostatic Quadrupole Triplets

The first elements of the HE AMS system are two Electrostatic Quadrupole Triplet (EQT) lenses that are used to provide mass independent cylindrically symmetrical focusing of the ions exiting the accelerator.

An EQT is simply a sequence of three quadrupoles. This section of the AMS HE system is designed to have the first EQT focus the cylindrically symmetric and divergent ion beam exiting the Tandem to a horizontal and vertical waist at an appropriate position before the second EQT, and the second EQT is positioned to subsequently focus the divergent ion beam coming from that waist to a cylindrically symmetric waist at the object position of the AMS HE 90° bend dipole magnet. Figure 3.14 shows a picture of the first EQT of iThemba LABS AMS system.

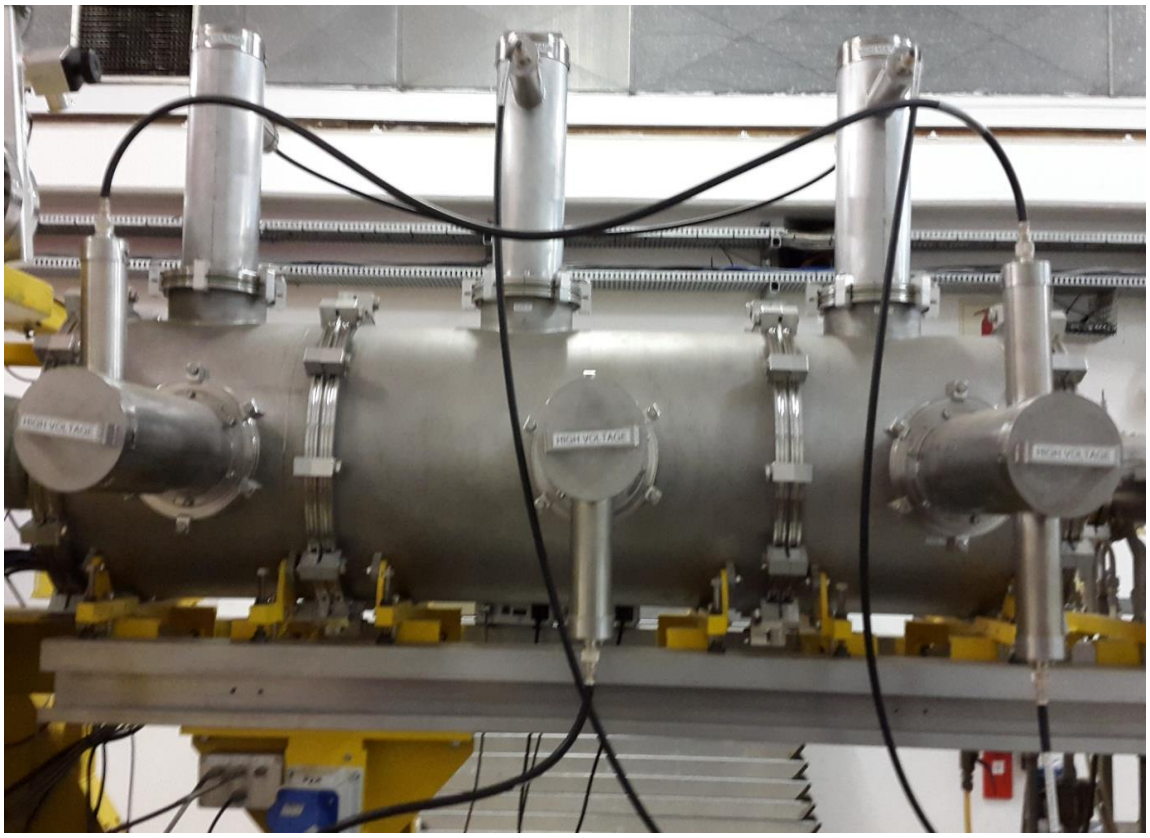

Figure 3.14: The first EQT after the tank of iThemba LABS.

AMS HE 90° Magnet

The new AMS HE 90° bend dipole magnet has a bending radius of curvature of 1270 mm, a field of 1.51 T, a pole gap of 34 mm, and the entrance pole face angle of 26.7° and the exit pole face angle of 26.6° are indicative of the double focusing design of the magnet.

At a given magnetic field strength this analyzing magnet bends ions in the horizontal plane on radii determined by their magnetic rigidity. During AMS operations, the magnetic field of the 90° analyzing magnet is set to bend ions of the radioisotope of interest through 90° on the magnet's designed radius of curvature and, hence, to transport the ions on the design trajectory into the following sections of the HE AMS system. This selection of the ions of the

radioisotope of interest that have the desired charge state and energy effectively eliminates many potential interfering ions from transport into the following sections of the HE AMS system; in the case of $^{14}C^{4+}$ measurements these eliminated ions species include 1^+, 2^+, 3^+ and 5^+ ^{14}C ions, essentially all ^{13}C and ^{12}C ions, all H+ ions, etc.. As with the LE analyzing magnet, the exit of the AMS HE 90° magnet vacuum box is wide enough to allow the measurement of ions of other radioisotopes in off-axis Faraday cups; in the case of $^{14}C^{4+}$ measurements, $^{13}C^4$ ion currents are measured in such an off-set Faraday cup. One point that is of significance in the design of the HE AMS system is that other ions with the same magnetic rigidity as the ions of the radioisotope of interest will also bend through 90° on the magnet's designed radius of curvature and, hence, will be transported into the following sections of the HE AMS system. The elimination of such other ions with the same magnetic rigidity is accomplished in the following Cylindrical ESA. Fig. 3.15 shows the picture of AMS analyzing magnet of iThemba LABS.

Figure 3.15: HE AMS 90°analyzing magnet of the iThemba LABS

Cylindrical ESA

In the iThemba HE AMS system a cylindrical electrostatic analyzer (ESA) has been installed 6.51 m downstream of 90° AMS magnet. An ESA is used to achieve further rejection of unwanted ions or "clones"; "clone-ions" are ions with the same magnetic rigidity as the desired ions of the isotope of interest, and hence the clone-ions are bent through 90° in the HE AMS 90° magnet just as the ions of interest. These clone-ions can be formed downstream of the stripping canal through charge exchange collisions with residual gas in the HE accelerator tubes. In order to filter them out, one has to exploit some characteristic of the ions other than magnetic rigidity; in the iThemba HE AMS system an electrostatic bend provides second stage of filtering based on the energy/charge ratio (E/q) of the ions, rather than their magnetic rigidity.

In the iThemba HE AMS system a cylindrical electrostatic analyzer (ESA) 6.51 m downstream of 90° AMS magnet provides sufficient energy resolution to remove most, if not all, "clone-ions" components that are present due to charge exchange or scattering processes. The ESA was procured from NEC and is composed of two cylindrical section electrodes having a central radius of 3.81 mm, a 30 mm electrode-to-electrode gap, and a 22.5° bend angle. Figure 3.16 shows the picture of cylindrical ESA.

The ion selection takes place according to:

$$E = \frac{\Delta q K r_0}{2d} \tag{3.5}$$

where E is the electric field between the ESA plates, q is the charge state of the ion, K is the energy of the ion and r_o is the radius of curvature of the ESA. By using the K_{total} calculated for the isotope of interest the desired E for the ESA can be calculated.

The 22.5° ESA provides an almost impenetrable barrier for residual magnetic rigidity ambiguities. Unwanted $^{13}C^{3+}$ and $^{12}C^{3+}$ ions strike the ESA plates and cannot be re-injected into the $^{14}C^{4+}$ ESA unless they have either been deflected through a substantial angle, which will usually cause them to leave the ESA later, or have suffered two charge changes (3^+ to 4^+ followed by 4^+ to 3^+) at symmetrical locations around the center of the ESA (Purser, 1992). To minimize such effects, a high-speed cryopump, at the center of ESA, maintains vacuum pressures in the range of 10^{-8} Torr.

Ions that are not ^{14}C but have the desired magnetic rigidity will have the wrong E/q. The ESA filters out (almost) all of the remaining backgrounds, except for isobars, of course. An issue that can be encountered during the measurements of $^{14}C^{4+}$ is $^{7}Li^{2+}$ ions getting to the detector. Although conducting measurements at higher operating voltages of 6-7 MV allows the lithium contamination detector pulses to be easily discriminated from the true ^{14}C pulses in the Energy-Loss Gas Ionization detector (Loyd et. al., 1991), under some circumstances the $^{7}Li^{2+}$ ion count rate may overwhelm the detector and electronics. This issue can be avoided through the elimination of Li containing materials during sample processing. The M and q based analysis of the positive ions provided by a HE 90° bend magnet eliminates the $^{7}Li^{2+}$ ions in AMS systems using the $^{14}C^{3+}$ or $^{14}C^{5+}$ charge states.

Figure 3.16: Cylindrical ESA on the higher energy system of iThemba LABS.

Magnetic Quadrupole Doublet

Two identical Magnetic Quadrupole Doublets (MQD), have been placed just before and after the ESA (this positioning is based on Fig. 3.13 above). Each of these MQD have effective element lengths of 281 mm, an effective separation length of 119 mm, maximum gradient of 170 gauss/mm and an aperture of 53 mm. The first MQD is used to focus the beam coming from the HE AMS magnet to the switching magnet. The second MQD is focusing the beam coming out of the switching magnet to form a waist at the detector position. Figure. 3.17 shows a picture of one of the MQD of iThemba LABS AMS system. The magnet poles are made to be hyperbolic and the windings are coiled in such a way that the poles alternate having

the magnetic flux into or out of the beam. The magnetic field within the central section through which the ion beam passes i.e. between the poles, can be described by the equation:

$$B = \frac{B_T}{a} y\hat{x} + \frac{B_T}{a} x\hat{y} \tag{3.6}$$

where B_T is the magnetic field density at pole tip and, a is the radius of the quadrupole gap.

Figure 3.17: Photograph of one of the MQD of iThemba LABS.

Switching Magnet

A Switching Magnet with four exit ports was mounted following the ESA exit beam line; the Switching Magnet acts as an additional stage of background suppression. The exit ports can accommodate different detectors for the detection of different isotopes, such as ^{14}C

versus ^{236}U. The radiocarbon gas ionization detector is mounted at the 25° left exit port on the east in the switching magnet. Fig. 3.18 shows a picture of AMS switching magnet of iThemba LABS.

The Switching Magnet has pole gap of 34 mm, and mass energy product of ME/Z^2 =176 MeV amu. The Switching Magnet is double focusing, more or less, due to the 0° entrance and the variable exit angle (i.e. depending on bending angle). On this type of Switching Magnet the pole on the exit side is circular, but with a radius which is the effective length of the entire pole piece along the 0° axis. The radius of curvature of the ions will be different depending on the exit port chosen; for radiocarbon beamline with pole radius (R_p of 0.642 m, the radius of curvature is 1.48 m as calculated from Eq. (3.7). The bending radius, R, for any bending angle, φ by:

$$R = \frac{R_p}{(2 * \sin(\varphi / 2))} \tag{3.7}$$

Figure 3.18: Photograph of AMS switching magnet of iThemba LABS.

3.1.1.5 Detectors for AMS

Finally, the ions are detected in an Energy-Loss Gas Ionization detector. The NEC-made detector consists of a gas filled chamber containing a set of five flat-plate metal anodes and a thin Mylar ($(C_{10}H_8O_4)_n$) foil entrance window (through which the ions enter the detector) at the end of the detector's housing. In ^{10}Be measurements a Havar window is used. In routine radiocarbon measurements, the information regarding the differential energy loss was not necessary and just the ΔE signal was typically acquired.

The ions are slowed down and come to rest in the gas by and electrons are knockoff the gas atoms losing energy through ionization of the gas molecules. These electrons are collected onto segmented metal plate anodes by an applied electric field within the detector; the pulse of electrons for each ion is amplified and shaped, digitized and then read into the data acquisition system (computer). Through the signals from the series of the anodes in the detector, an ion's spatial distribution of energy loss in the gas can be measured, as well as the total energy of the ion. For each ion the computer determines the rate of energy-loss and from that one can deduce the nuclear charge i.e. atomic number of the element. Figure. 3.19 shows the detection system of iThemba LABS AMS system.

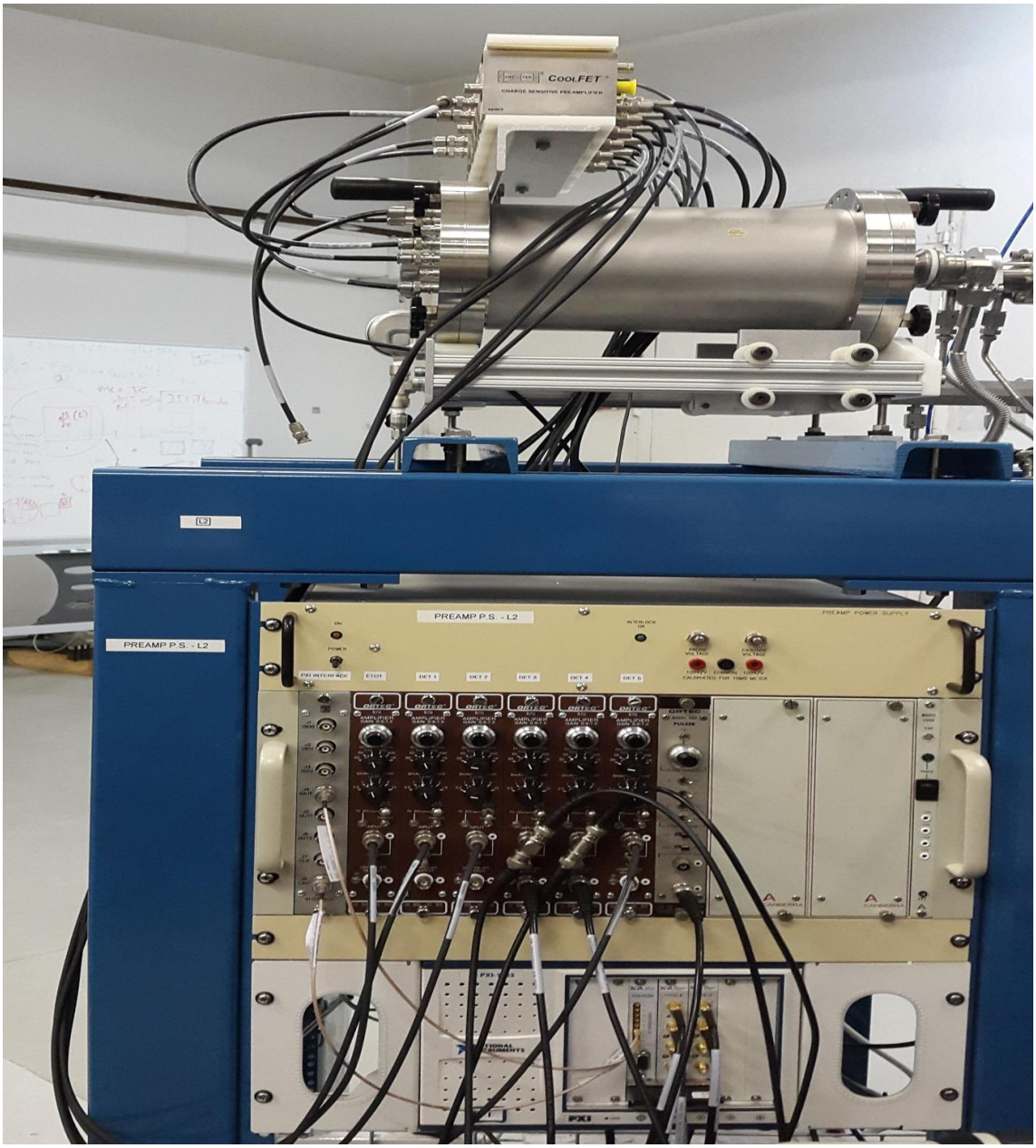

Figure 3.19: AMS detector of iThemba LABS.

CHAPTER 4
BEAM OPTICS OF THE TANDEM ACCELERATOR AT ITHEMBA LABS

4.1 Introduction to Ion Beam Optics

The development and optimization of the design of the new high performance AMS system in terms of high mass/momentum/energy resolution for high-precision and high-throughput measurements, has, to a significant degree, been based on ion beam optics calculations run on desktop computers. These calculations provided guidance on the theoretical performance of planned sections of the system and, hence, provided a method to evaluate the sections functionality and to optimize the characteristics of the various optical elements involved.

The ion beam optics calculations presented here were based on particle beam optics as described via the matrix (beam-envelope) formalism. The calculations were run within the Shell for Particle Accelerator Related Codes (S.P.A.R.C.), and, in particular, utilized the POWERTRACE module (Gillespie and Hill, 1992; AccelSoft, 2013). The POWERTRACE module provides a graphical user interface for the entry of parameters, control of execution and structured output of the TRACE 3-D ion beam transport program.

TRACE 3-D is a program that calculates the evolution of the envelope of a bunched beam, as it is transported through a user-defined ion beam transport system (Crandall and Rusthoi, 1997). TRACE-3D uses 6 x 6 transfer matrix formalism (which includes a linear space-charge model) to calculate, the first-order, vertical, horizontal and longitudinal beam envelopes along the length of the ion-transport system.

The approach is to simulate the whole AMS and the emittance of the ion beam is defined as the ‘‘volume’’ in the six dimensional phase space (x, y, z, p_x, p_y, p_z) that is occupied by the ion beam. As a result, ion beams with uniform charge distribution of ellipsoid symmetry, the root mean squared (rms) properties can be replaced by an equivalent uniform beam (Gillespie, 1998). The transport system elements are also represented by matrices. The symmetry considerations allow the focusing and transport properties of an ion-optical element contained in its 6 x 6 transfer matrix to be equivalently expressed using two independent 2 x 2 matrices (AccelSoft, 2013). The beam ellipsoid matrix is propagated through the accelerator elements by a process of transformations involving the element matrices. The elements can be represented by first-order. This matrix model allows us to divides each element into a series of small (longitudinal) segments and the calculation then steps through the beamline one segment at time (Gillespie and Brown, 1997). The effective transfer matrix may be modified in each segment.

Almost the entire range of optical elements used in an AMS system can be modeled with the TRACE-3D, namely drifts, Einzel lenses, thin lenses, magnetic quadrupoles, electrostatic quadrupoles, bending magnets, edge angles for bending magnets, accelerator tubes, and ESAs.

For practical reasons related to certain constrains within the code, two major sections of the total system/spectrometer were modeled separately; first, the LE injection system through to the gas stripping canal, and, second HE system from the stripping canal through to the Energy-Loss Gas Ionization detector.

A charged particle beam is specified by its energy and its emittance. The emittance of the ion beam is defined as the ‘‘volume’’ in the six dimensional phase space (x, y, z, p_x, p_y, p_z) that is occupied by the ion beam. A brief description of the matrix formalism with respect to the ion optical elements used in the iThemba LABS AMS system is given below:

Emittance

The emittance of the beam leaving the ion source is partly determined by the processes occurring in the ion source and partly by the design of the source. A low numerical value of the emittance is desirable as it means low transverse dimensions of the beam after it has passed some distance along a drift section. Figure 4.1a shows the emittance as the area A of the ellipse (π. *ab*) where *a*, *b* are the semiaxes of the ellipse,

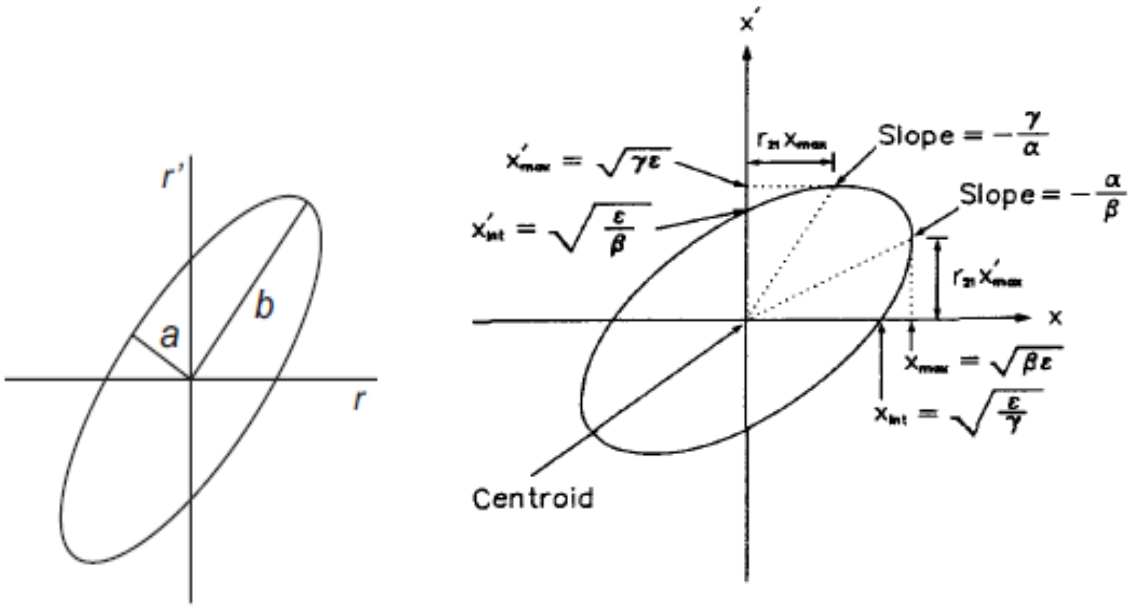

Figure 4.1: Emittance diagram. a) The area of the ellipse is given by A = π.ab mm mrad. b) Emittance ellipse geometry and Twiss parameters (Jo et al., 1991).

The emittance, ε, in an ion beam envelope in the phase space is expressed as the area of the phase ellipse in terms of the so-called Twiss parameters α, β, and γ. The maximum values of x and x', as seen in the Fig. 4.1b, are defined as;

$$x_{\max} = \sqrt{\beta\varepsilon} \tag{4.1}$$

$$x'_{max} = \sqrt{\gamma\varepsilon}\ . \tag{4.2}$$

If vector X and σ are beam matrixes defined as follows:

$$X = \begin{bmatrix} x \\ x' \end{bmatrix} \tag{4.3}$$

$$\sigma = \begin{bmatrix} \sigma_{11} & \sigma_{12} \\ \sigma_{21} & \sigma_{22} \end{bmatrix} = \varepsilon \begin{bmatrix} \beta & -\alpha \\ -\alpha & -\gamma \end{bmatrix} \tag{4.4}$$

then the phase ellipse shown at Fig. 4.1b is expressed as

$$X^{\mathrm{T}} \sigma^{-1} X = 1 \tag{4.5}$$

where X^{T} is the transpose of X. For this to represent an n-dimensional ellipsoid, all the diagonal elements of the σ^{-1} must be positive. Single column matrix X, of specified position in the system of an arbitrary charged particle whose components are positions, angles, and momentum of particle with respect to the reference trajectory is given by:

$$X = \begin{bmatrix} x \\ x' \\ y \\ y' \\ l \\ \delta \end{bmatrix} \tag{4.6}$$

and X_0 is represented by

$$X_0 = \begin{bmatrix} x_0 \\ x_0' \\ y_0 \\ y_0' \\ l_0 \\ \delta_0 \end{bmatrix}. \tag{4.7}$$

The *R*-matrix is defined as follow:

$$R = \begin{bmatrix} R_{11} & R_{12} & R_{13} & R_{14} & R_{15} & R_{16} \\ R_{21} & R_{22} & R_{23} & R_{24} & R_{25} & R_{26} \\ R_{31} & R_{32} & R_{33} & R_{34} & R_{35} & R_{36} \\ R_{41} & R_{42} & R_{43} & R_{44} & R_{45} & R_{46} \\ R_{51} & R_{52} & R_{53} & R_{54} & R_{55} & R_{56} \\ R_{61} & R_{62} & R_{63} & R_{64} & R_{65} & R_{66} \end{bmatrix} . \quad (4.8)$$

The ion beam current, Twiss parameters and emittance in the longitudinal plane of this extended beam bunch are then defined as prescribed in (Gillespie, 1998).

Twiss parameters a waist are given by

$$\varepsilon = xx' \, , \beta = \frac{x_m}{x_m'} \quad (4.9)$$

where β is the relativistic parameter (v/c) for the initial beam.

Transfer matrices

In Transport, a beamline is described as a sequence of elements. Such elements may consist not only of magnets and the intervals between them, but also of specifications of the input beam, calculations to be done, or special configurations of magnets. The input is given in terms of semi-axes of a six-dimensional beam ellipsoid representing the phase space variable x, x', y, y', l, δ. The transfer matrices of 6 X 6 will be partitioned into nine (2 X 2) matrices. The calculation of a beam envelope at any point along a beam line involves the operation of any intervening transfer matrices upon the starting beam's phase space coordinates. Beam matching occurs when an initial ion beam is transported to desired final focus through any limiting apertures.

$$\begin{bmatrix} x \\ x' \\ y \\ y' \\ l \\ \delta \end{bmatrix} = R \begin{bmatrix} x_0 \\ x_0' \\ y_0 \\ y_0' \\ l_0 \\ \delta_0 \end{bmatrix} = \begin{bmatrix} [R_{xx}] & [R_{xy}] & [R_{xz}] \\ [R_{yx}] & [R_{yy}] & [R_{yz}] \\ [R_{zx}] & [R_{zy}] & [R_{zz}] \end{bmatrix} \begin{bmatrix} x_0 \\ x_0' \\ y_0 \\ y_0' \\ l_0 \\ \delta_0 \end{bmatrix} = \begin{bmatrix} R_{11} & R_{12} & R_{13} & R_{14} & R_{15} & R_{16} \\ R_{21} & R_{22} & R_{23} & R_{24} & R_{25} & R_{26} \\ R_{31} & R_{32} & R_{33} & R_{34} & R_{35} & R_{36} \\ R_{41} & R_{42} & R_{43} & R_{44} & R_{45} & R_{46} \\ R_{51} & R_{52} & R_{53} & R_{54} & R_{55} & R_{56} \\ R_{61} & R_{62} & R_{63} & R_{64} & R_{65} & R_{66} \end{bmatrix} \begin{bmatrix} x_0 \\ x_0' \\ y_0 \\ y_0' \\ l_0 \\ \delta_0 \end{bmatrix} \tag{4.10}$$

Only the non-zero will be defined as most of the elements are zero.

The transfer matrices generated for each element or for each segment of length L are defined below. β and γ are the relativistic parameters.

Drift space

A drift space is a field free region through which the beam passes, where there is no force acting on the particle, and there is no change in the momentum of the particle, as illustrated in Fig. 4.2. For a drift, the non-zero R-matrices are as follows:

$$\boldsymbol{R}_{11} = \boldsymbol{R}_{22} = \begin{bmatrix} \mathbf{1} & \boldsymbol{L} \\ \mathbf{0} & \mathbf{1} \end{bmatrix}$$

$$\boldsymbol{R}_{33} = \begin{bmatrix} \mathbf{1} & \boldsymbol{L}/\gamma^2 \\ \mathbf{0} & \mathbf{1} \end{bmatrix}, \tag{4.11}$$

where γ is non-relativistic element, $\Delta v/v=(\Delta p/p)/\gamma^2$.

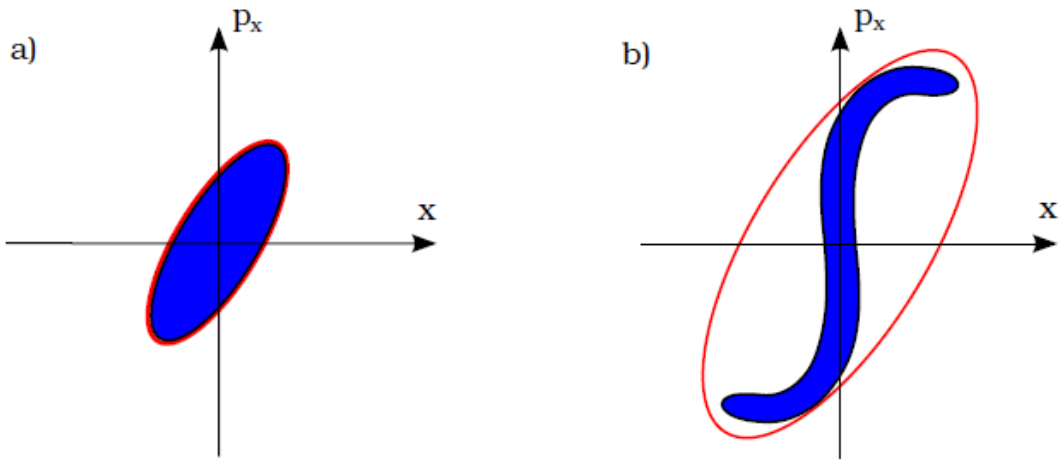

Figure 4.2: A two-dimensional projection of an ensemble of particles (a) before going through a nonlinear optical system and (b) after it. The area of the particle distribution (shown in blue) is conserved but the area of the elliptical envelope (shown in red) increases.

Thin lenses

The action of a thin lens on a point (r_1, r_1') in phase space is given by linear transformation:

$$R_{11} = R_{22} = \begin{bmatrix} 1 & 0 \\ -\frac{1}{f} & 1 \end{bmatrix}$$

$$R_{33} = \begin{bmatrix} 1 & 0 \\ -\frac{\gamma^2}{f} & 1 \end{bmatrix}. \qquad (4.12)$$

Einzel lens

Einzel lens is an axially symmetric ion optical element and is made by combining two gap lenses into three-electrode system with first and last electrodes at the beamline potential U_1 and the center electrode at different potential U_0. The parameters of the beam transport for

the Einzel lens element are mainly the beam energy, the voltages on the electrodes as well as the distances between the electrodes (the radii of the electrodes and the length of the center electrodes are also of crucial importance). The Einzel lens, which is typically cylindrically symmetric for round beams, is the main tool for beam focusing in many electrostatic extraction systems Fig. 4.3 is the schematic drawing of an Einzel lens.

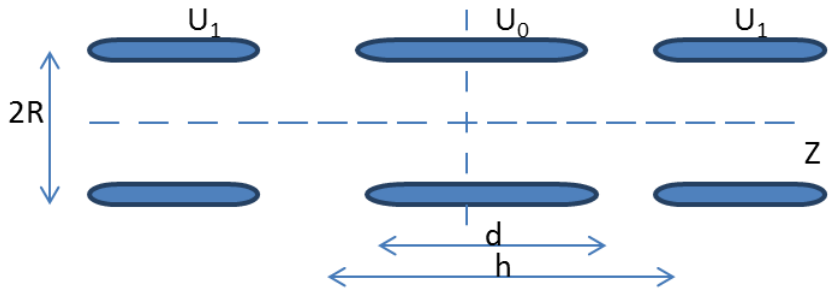

Figure 4.3: A schematic drawing of an Einzel lens with its parameters R, d and h. There are three-electrode on the Einzel lens. The two outermost electrodes are kept at the ground potential and the central one in some desired, that is either positive or negative voltage.

Usually the voltage U_1 is set to ground. The Einzel focusing power is dependent on the geometry and the voltage ratio $R = (U_0 - U_1)/U_1$, assuming that zero potential is where the beam kinetic energy is zero. The Einzel lens may have the first gap accelerating and the second gap decelerating (known as accelerating Einzel lens, $R > 0$) or vice versa (known as decelerating Einzel lens, $R < 0$). Both configurations are focusing, but the refractive power of the Einzel in decelerating mode is much higher than in accelerating mode with the same lens voltage.

The 6 X 6 *R*-matrix for Einzel lens reduces to the following equation (Brown and Gillespie, 1999):

$$R = \begin{bmatrix} 0 & 0 & R_{13} & 0 & 0 & 0 \\ 0 & R_{22} & 0 & R_{24} & 0 & 0 \\ 0 & 0 & R_{33} & R_{34} & 0 & 0 \\ 0 & 0 & 0 & R_{44} & 0 & 0 \\ 0 & 0 & 0 & 0 & 0 & R_{56} \\ 0 & 0 & 0 & 0 & 0 & R_{66} \end{bmatrix} , \qquad (4.13)$$

where $R_{13} = R_{24}$ and $R_{22} = R_{44}$

The optics of particles near the axis of cylindrically symmetric electrostatic elements is determined by axial potential distribution *U(z)* (Gillespie and Brown, 1999). The near axis electric fields, which satisfy Maxwell's equation $\nabla.E = 0$, for any *U(z)*, are given by:

$$E_x(x, y, z) = \frac{\partial U}{\partial x}(x, y, z) \approx + \frac{x}{2} U''(z) \qquad (4.14)$$

$$E_y(x, y, z) = \frac{\partial U}{\partial y}(x, y, z) \approx + \frac{y}{2} U''(z) \qquad (4.15)$$

$$E_z(x, y, z) = \frac{\partial U}{\partial z}(x, y, z) \approx - U''(z) \qquad (4.16)$$

The first *R*-matrix, together with an increase in beam energy, computes the effects of uniform electric field acting over a distance of Δz. The non-trivial *R*-matrix elements are:

$$R_{13} = R_{24} = 2\Delta z / [1 + (\eta_-)^{1/2}] \qquad (4.17)$$

$$R_{22} = R_{44} = R_{66} = 1/(\eta_-)^{1/2} \qquad (4.18)$$

$$R_{56} = \Delta z / \gamma^2 , \qquad (4.19)$$

where $\eta_- = U(z)/U(z - \Delta z)$ and γ is the relativistic energy factor of the beam at *z*.

The 6 X 6 *R*-matrix for thin lens reduces to the following equation:

$$R = \begin{bmatrix} R_{11} & R_{12} & R_{13} & 0 & 0 & R_{16} \\ R_{21} & 0 & 0 & R_{24} & 0 & R_{26} \\ 0 & 0 & R_{33} & R_{34} & 0 & 0 \\ 0 & 0 & R_{43} & 0 & 0 & 0 \\ R_{51} & R_{52} & 0 & 0 & R_{55} & R_{56} \\ 0 & 0 & 0 & 0 & 0 & R_{66} \end{bmatrix} \tag{4.20}$$

The second *R*-matrix computes an effective thin lens for the incremental focusing effect of the field applied as an impulse. The non-trivial elements of the *R*-matrix are:

$$R_{21} = R_{43} = -\left[\eta_{-}\eta_{+} - 2\eta_{-} + 1\right]/\left(4\eta.\Delta z\right) \tag{4.21}$$

where $\eta_{+} = U(z + \Delta z)/U(z)$. The formulae given can be used to model any electrostatic element whose potential is given at discrete positions along the *z*-axis.

Electrostatic quadrupoles

A sketch of an electrostatic quadrupole triplet is shown in Fig. 4.4. An ideal EQT has hyperbolically shaped electrodes. Since the production of hyperbolically shaped electrodes is rather trying compared to cylindrically shaped ones the hyperbola is often approximated by circle (Meier, 2007), It turns out that the best approximation is obtained if the radius of the electrodes is approximately 1.147 times the aperture radius as can be seen on Fig. 4.5 (Wollnik, 1987). The approximation is only valid close to the *z*-axis. The beam profile should not exceed half the aperture of the quadrupole in order to maintain a good quadrupole approximation.

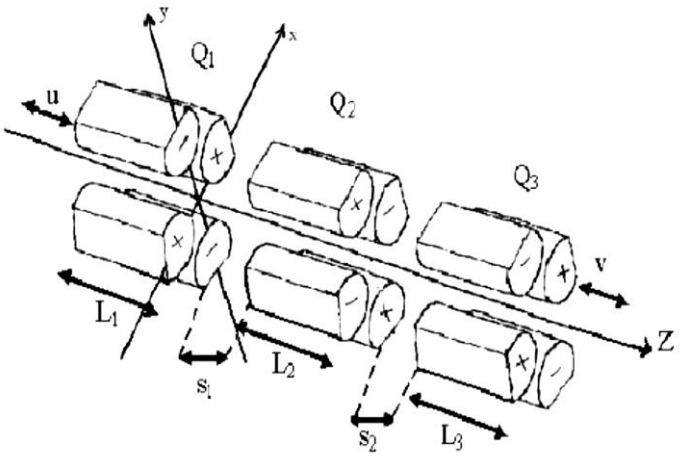

Figure 4.4: Sketch of a electrostatic quadrupole triplets (Juma et al., 2007).

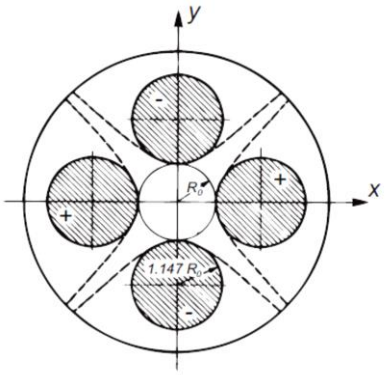

Figure 4.5: The electrodes of a quadrupole are often approximated by cylindrical rods.

EQT model use in TRACE 3-D for iThemba LABS AMS system is Hard-Edge where the magnitude of the quadrupole field is constant over the quadrupole length and zero elsewhere. The first order optics for a particle moving in the field of a Hard-Edge EQT is the same as for the motion in magnetic quadrupole using an equivalent field gradient *B*:

$$B = 2V_0/(a^2\beta c), \tag{4.22}$$

where V_0 is the electrode voltage of the EQT, a is the radial aperture of the EQT, and βc is the velocity of the particle.

Electrostatic Analyzers

The ESA is assumed to have mid-plane symmetry and the deflection plane is taken to be the *x*-*z* plane ("horizontal") (Brown and Gillespie, 1999). The geometry for the first-order optics can be defined in terms of two radii: r_{e0}, the (horizontal) radius of curvature of a particle (reference particle) moving on the equipotential surface between the two deflector plates corresponding to the initial beam voltage, and R_{e0}, the vertical radius of curvature of the equipotential surface, as shown in Fig. 4.6. The ESA model options in TRACE 3-D allow the first-order modeling of cylindrical, spherical, and toroidal ESA. For the electrostatic deflector the R-matrices are based on results from Wollnik (1967).

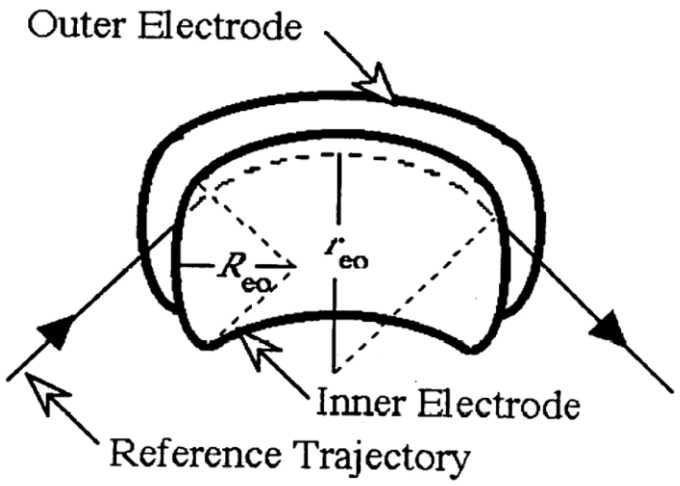

Figure 4.6: The ESA electrode and ion trajectory geometry used for the ESA model (Brown and Gillespie, 1999)**.**

The 6 X 6 *R*-matrix for static systems with mid-plane symmetry reduces to the following equation (Brown and Gillespie, 1999):

$$R = \begin{bmatrix} R_{11} & R_{12} & 0 & 0 & 0 & R_{16} \\ R_{21} & R_{22} & 0 & 0 & 0 & R_{26} \\ 0 & 0 & R_{33} & R_{34} & 0 & 0 \\ 0 & 0 & R_{43} & R_{44} & 0 & 0 \\ R_{51} & R_{52} & 0 & 0 & 1 & R_{56} \\ 0 & 0 & 0 & 0 & 0 & 1 \end{bmatrix}. \tag{4.30}$$

The central path length through the ESA is divided into an integral number of steps each of length Δz. The non-trivial elements of the *R*-matrix can then be expressed in terms of the step size $\Delta z/2$, since ESA is assumed to have mid-plane symmetry and deflection plane is taken to be the horizontal plane, the reference trajectory curvature $h = 1/r_{e0}$, the reference trajectory's relativistic energy variable γ, and two dimensionless parameters p and q:

$$R_{11} = R_{22} = \cos[ph(\Delta z/2)] \tag{4.31}$$

$$R_{12} = \sin[ph(\Delta z/2)]/(ph) \tag{4.32}$$

$$R_{21} = -ph\sin[ph(\Delta z/2)] \tag{4.33}$$

$$R_{33} = R_{44} = \cos[qh(\Delta z/2)] \tag{4.34}$$

$$R_{34} = \sin[qh(\Delta z/2)]/(qh) \tag{4.35}$$

$$R_{43} = -qh\sin[qh(\Delta z/2)] \tag{4.36}$$

$$R_{16} = -R_{52} = \{1-\cos[ph(\Delta z/2)]\}/(p^2h) \tag{4.37}$$

$$R_{26} = -R_{51}\sin[ph(\Delta z/2)]/p \tag{4.38}$$

$$R_{56} = \{ph(\Delta z/2) - \sin[ph(\Delta z/2)]\}/(ph) + (\Delta z/2/\gamma^2) \tag{4.39}$$

The dimensionless parameters p and q for spherical and cylindrical. The relativistic formulations are:

p is $(1 - \beta^2)^{1/2}$ for spherical and $(2 - \beta^2)^{1/2}$ for cylindrical and q is 1 for spherical and 0 for cylindrical.

Bending magnets

A bending magnet (α', ρ, n, vf) with a positive bend (denoted $\alpha' > 0$), bends the particle to the right in the horizontal plane (or upwards for vertical bend), regardless of the sign of the charge on the particle; a negative α bends particle to the left (or downwards for a vertical bend) (Crandall and Rusthoi, 1997). The parameter α' is bending angle in (deg), ρ is radius of curvature of central trajectory in (mm), n is field-gradient index, and vf is vertical flag (it is zero for horizontal bend). Figure 4.7 shows the beam trace around a bending magnet as well as the pole face angles (edges) with respect to the entrance and exit ports. Figure 4.8 illustrates the focusing of the magnet (a) for 0° edge angles and (b) positive edge angles.

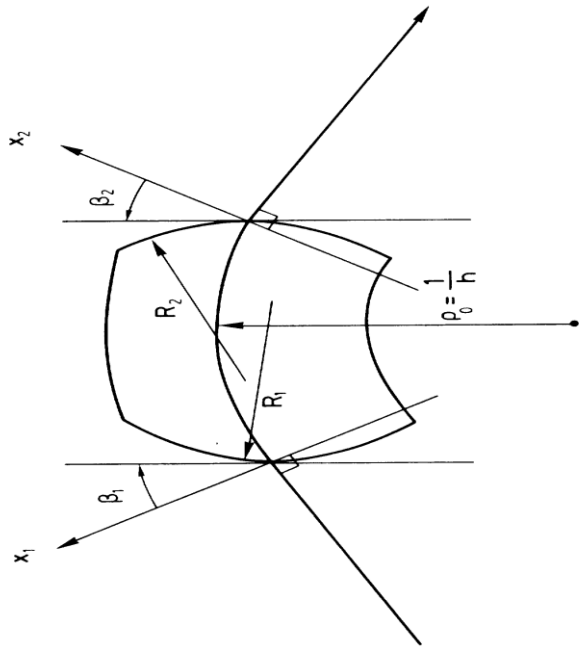

Figure 4.7: Field boundaries for bending magnets. Definition of the quantities β_1, β_2, R_1 and R_2 used in the matrix elements for field boundaries of bending magnets (Brown, 1975).

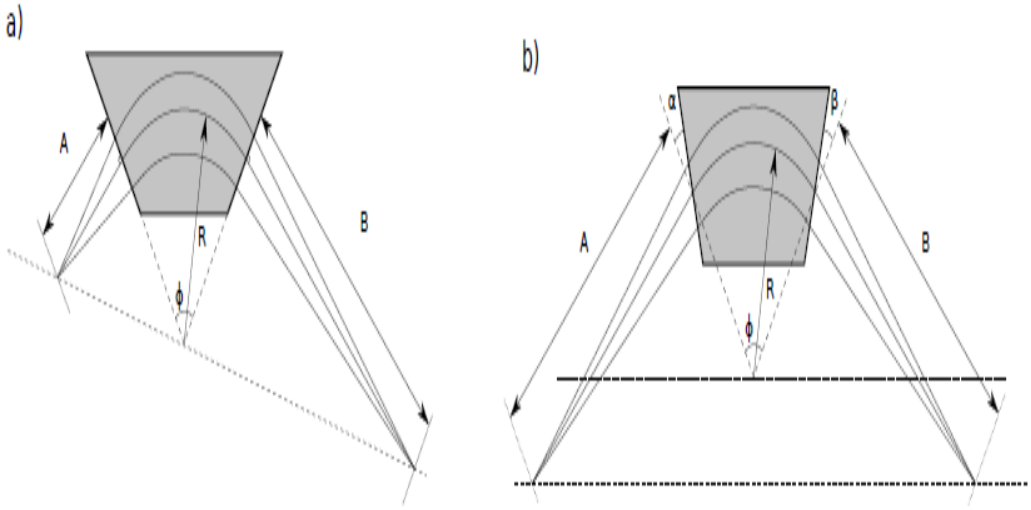

Figure 4.8: Focusing of a magnetic dipole in the bending plane (a) the case where the magnet has 0^0 edge angles can be described by Barber's rule: the center of curvature of optical axis and the two focal points are on a straight line. (b) if the edge angles are positive, as shown, the focusing power is decreased. If the angle is negative, there is stronger focusing in the horizontal direction. Changing the edge angle also has important effect in the y direction: If the angles are positive, the fringing field of the magnet will focus the beam in the vertical direction.

If the magnet edge angles deviate from 90^o, the focusing power in the horizontal direction can be adjusted. If the edge angle is made positive as shown in Fig. 4.8b, there is weaker focusing in the horizontal direction. If the angle is negative, there is stronger focusing in the horizontal direction. Changing the edge angle also has important effect in the y direction: If the angles are positive, the fringing field of the magnet will focus the beam in the vertical direction, as shown in Fig. 4.8. Overall, this means the focusing in the horizontal direction can be traded for vertical focusing. The focal length from the edge focusing is given by

$$f_y = \frac{R}{\tan\alpha'}. \tag{4.40}$$

In a symmetric double-focusing dipole (where there is the same focal length in horizontal and vertical directions), the angles and distances are given by

$$2\tan\alpha' = 2\tan\beta = \tan(\phi/2) \tag{4.41}$$

$$A = B = \frac{2R}{\tan(\phi/2)}. \tag{4.42}$$

For a ϕ = 90° bending magnet, the edges angles becomes α' and β = 26.6° and the focal distances $A = B = 2R$.

The bending radius of the equilibrium orbit is ρ, and n is the field index, given by:

$$n = \left[\frac{\rho}{B_y}\ \frac{\partial B_y}{\partial x}\right]_{x=0,\,y=0} \tag{4.43}$$

where B_y is the vertical component of the magnetic field strength. The bending radius ρ is related to B_y by the following equation:

$$\rho = \frac{m_0 c\beta\gamma}{qB_y}. \tag{4.44}$$

Then the transfer matrix for a horizontal sector magnet is as follows:

$$R_{xx} = \begin{bmatrix} C_x & \frac{1}{k_x}S_x \\ -k_x S_x & C_x \end{bmatrix} \tag{4.45}$$

$$R_{yy} = \begin{bmatrix} C_y & \frac{1}{k_y}S_y \\ -k_y S_y & C_y \end{bmatrix} \tag{4.46}$$

$$R_{xz} = \begin{bmatrix} 0 & h(1-C_x)/k_x^2 \\ 0 & hS_x/k_x \end{bmatrix} \tag{4.47}$$

$$R_{zx} = \begin{bmatrix} hS_x/k_x & -h(1-C_x)/k_x^2 \\ 0 & 0 \end{bmatrix} \tag{4.48}$$

$$h = \frac{1}{|\rho|}\frac{\alpha}{|\alpha|} \tag{4.49}$$

$$k_x = \sqrt{(1-n)h^2} \tag{4.50}$$

$$k_y = \sqrt{nh^2} \tag{4.51}$$

$$C_x = \cos(k_x \Delta s) \tag{4.52}$$

$$S_x = \sin(k_x \Delta s) \tag{4.53}$$

$$Cy = \cos(k_y \Delta s) \tag{4.54}$$

$$S_y = \sin(k_y \Delta s) \tag{4.55}$$

$$\Delta s = |\rho| \Delta \alpha \tag{4.56}$$

Magnetic Quadrupoles

Magnetic Quadrupole Doublets are used in the HE iThemba AMS system to focus the beam. The focal length of a magnetic quadrupole depends on the gradient of the magnetic field inside the quadrupole, ΔB, the relativistic momentum of the particles passing through it, p, and also on its length, L. Figure 4.9 shows sketches of the major components of a magnetic quadrupole.

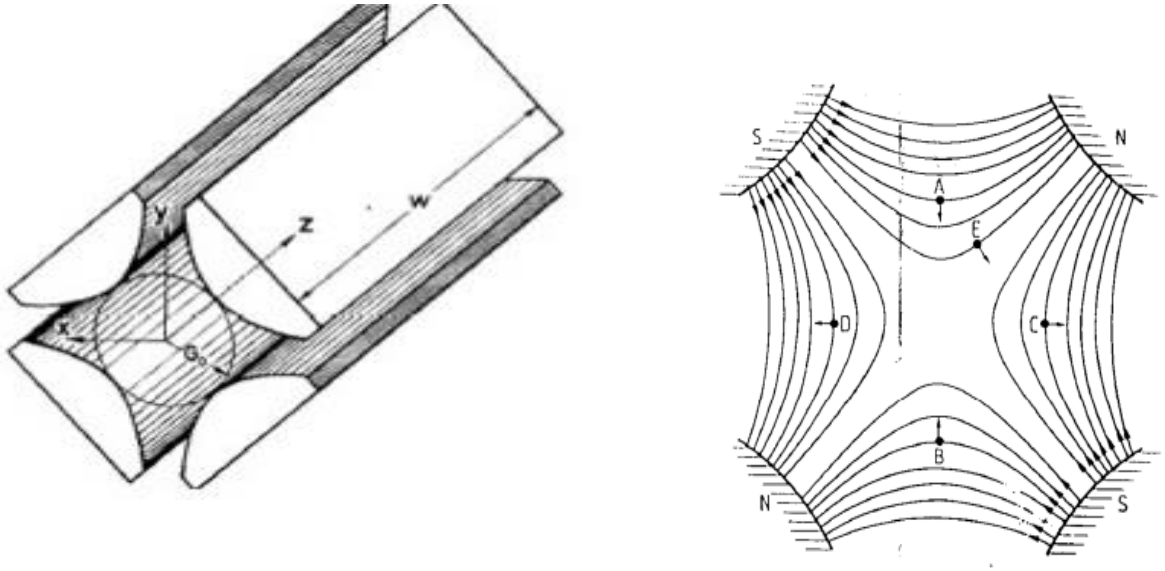

Figure 4.9: Magnetic quadrupole lens. The lines of field in a magnetic quadrupole, also shown are the forces acting on positively charged particles travelling into the plane of the paper at various points in the quadrupole aperture (A to E). A and B lie in the converging plane, while C and D are in the diverging plane.

A magnetic quadrupole can be described with matrix formulation similar to the one used for EQT. The magnifications and the demagnifications can be obtained from the first order transfer matrix of the complete magnetic quadrupoles system. The cardinal elements from Eq. (4.6) and Eq. (4.7) are defined for a lens system in which there is no coupling between the xoz and yoz plane; that is

$$(x/y)=(x/\phi)=(\theta/y)=(\theta/\phi)=(y/x)(y/\theta)=(\phi/x)=(\phi/\theta)=0 \qquad (4.57)$$

This condition applies in system consisting of quadrupoles and drift spaces in which the quadrupoles are correctly aligned. The magnification and demagnification of magnetic quadrupoles, expressed in terms of the elements of transfer matrix and defined by Eq. (4.58) and Eq. (4.59) provides the system is stigmatic with $(x/\theta) = (y/\varphi) = 0$.

$$M_x=(\theta/\theta)^{-1}=R_{22}{}^{-1}, M_y=(\phi/\phi)^{-1}=R_{44}{}^{-1} \qquad (4.58)$$

$$D_x=(\theta/\theta) \ =R_{22} \ , D_y=(\phi/\phi)=R_{44} \qquad (4.59)$$

If the quadrupole gradient B', the 2x2 transfer matrices in the focusing and defocusing planes can be expressed as (Crandall and Rusthoi, 1997):

$$F = \begin{bmatrix} \cos(kL) & k^{-1}\sin(kL) \\ -k\sin(kL) & \cos(kL) \end{bmatrix} \tag{4.60}$$

$$D = \begin{bmatrix} \cosh(kL) & k^{-1}\sinh(kL) \\ k\sinh(kL) & \cosh(kL) \end{bmatrix}, \tag{4.61}$$

where the parameter $k = \left[\left| \frac{\partial B_y / \partial x}{B_\rho} \right| \right]^{1/2}$. B_ρ is called the magnetic rigidity of the particle, defined as

$$B\rho = \frac{m_0 c \beta \gamma}{q}, \tag{4.62}$$

where q and m_0 are the charge and rest mass of the particle, and c is the velocity of light. When $B/B\rho$ is positive $R_{11} = F$ and $R_{22} =$ D; when negative $R_{11} = D$ and $R_{22} = F$. R_{33} is the same as for a drift in either case:

$$R_{33} = \begin{bmatrix} 1 & L/\gamma^2 \\ 0 & 1 \end{bmatrix} \tag{4.63}$$

4.2 Beam Optics Simulations for the Low Energy Injection System

The LE Injection System, as described in Chapter 3, has been modeled using PowerTrace/TRACE-3D calculations. The beam envelope was reproduced for ^{14}C isotopes in many calculations which guided the optimization of the design in order to obtain maximum

transmission and beam quality. The PowerTrace sequence of elements modeling the LE beamline is shown in Fig. 4.10 and Fig. 11 shows injection system for 6 MV Tandem accelerator at iThemba LABS.

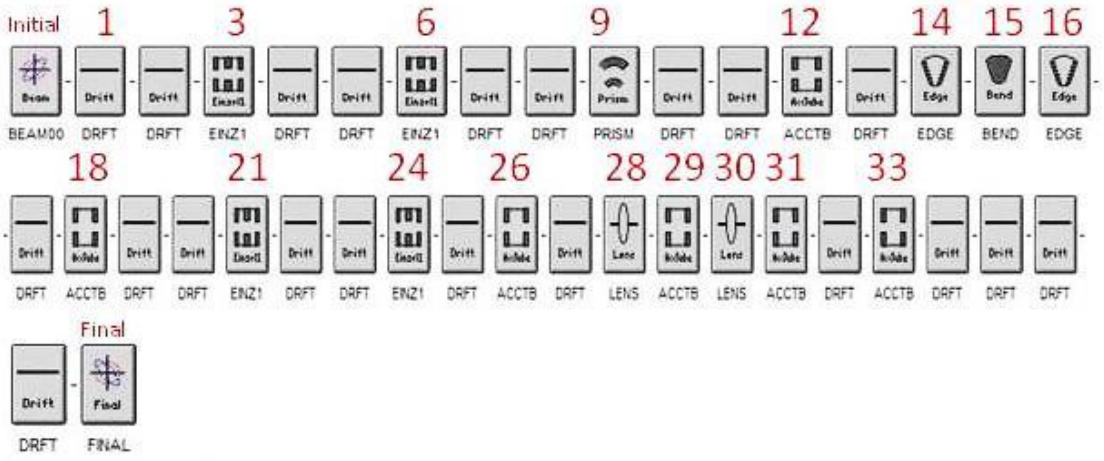

Figure 4.10: The Lower Energy palettes of 6 MV Tandem accelerator of iThemba LABS.

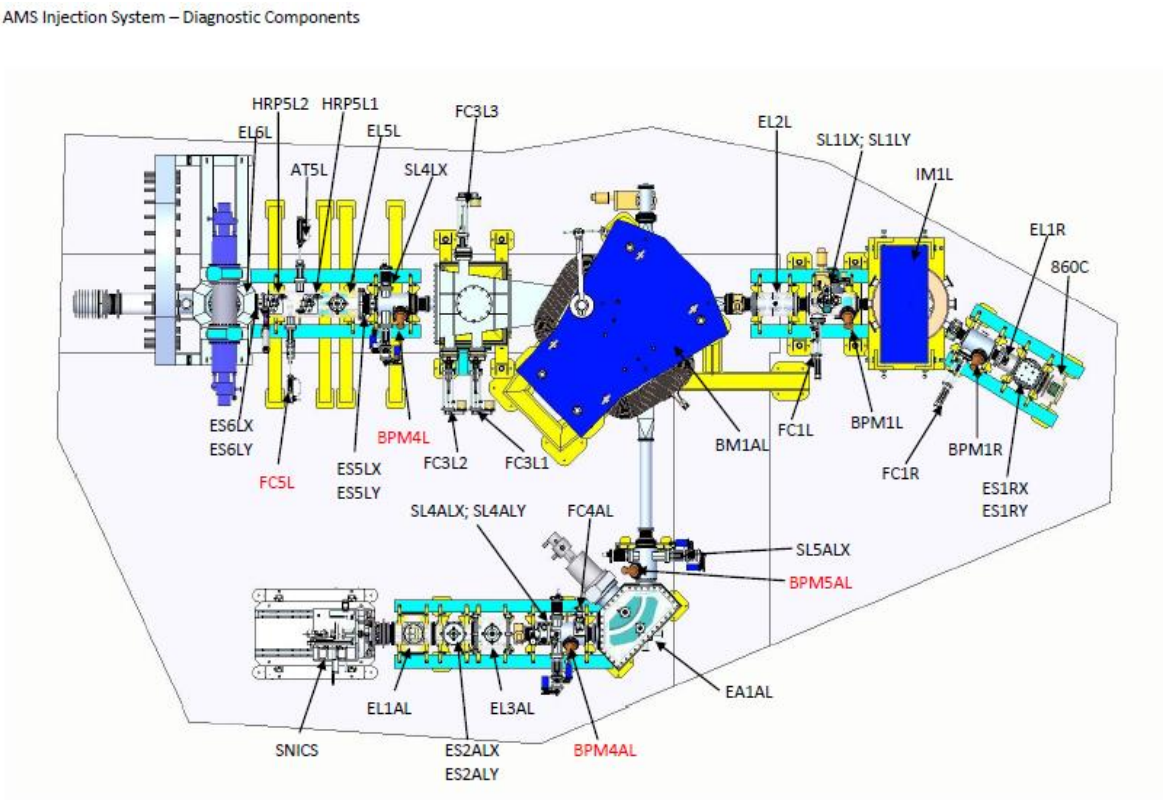

Figure 4.11: Injection system for 6 MV Tandem accelerator at iThemba LABS(Gauteng).

The sequence of elements in Fig. 4.10 was modeled according to the alignment of elements in the LE beamline configuration of iThemba LABS. Beamline models are constructed graphically using palette bar of accelerator element icons. The model takes the following into consideration:

- The CAMS/LLNL source and its specifications define the original emittance of the beam. The sputtered beam on the cathode has a diameter of the order of 0.7 mm and after the spherical ionizer and the extraction electrode it comes out of the ion source with approximately a circular shape with radius of 5 mm, a divergence of 10 mrad, and energy of 39 keV. Hence the ion source emittance is π x 5 mm x 10 mrad x $\sqrt{0.039}$MeV ~9.874π mm mrad MeV$^{1/2}$. The aim of the modeling effort is to arrange the beamline elements such that, given the ion source emittance, the ion beam falls within the

acceptances of the various elements as the beam is transported through the system, and hence, to achieve maximum beam transmission, with the most restrictive element being the stripping canal at the central terminal.

The original stripping canal had a 4 mm radius and it was replaced with one of 5.25 mm radius. The LE tube acceptance for forming a waist at the stripper is given by Larson and Jones (1977):

$$A_{\mathrm{LE}} = \pi \frac{r_1 r_2}{L} \sqrt{\left[1 - \left(\frac{r_2}{r_1}\right)^2\right]} \left[\frac{1}{2}\left(\sqrt{E_{\mathrm{T}}} + \sqrt{E_i}\right)\right] \qquad (4.64)$$

where r_1 = 12.69 mm is the tube aperture radius, r_2 = 5.25 mm is the radius of gas stripper canal-tube, L = 5191.5 mm is the distance from the entry of the accelerating tube to the gas stripper, E_{i} = 39 keV is the injection energy; and E_{T} is the energy of ion at terminal. For $E_{\mathrm{T}} = 1$, A_{LE} is calculated as follows:

$$A_{\mathrm{LE}} = \pi \frac{12.7mm \times 5.25mm}{5191.5mm} \sqrt{\left[1 - \left(\frac{5.25mm}{12.7mm}\right)^2\right]} \left[\frac{1}{2}\left(\sqrt{1} + \sqrt{0.039MeV}\right)\right]$$

$$= \pi(0.013mm)\sqrt{[1-0.171]}\left[\frac{1}{2}(1+0.1974)MeV^{\frac{1}{2}}\right]$$

$$= \pi(0.013mm)(0.91)\left[0.5987MeV^{\frac{1}{2}}\right]$$

$$= 0.0071 \ \pi \ mm \ MeV^{\frac{1}{2}}$$

$$= \ 7.1 \ \pi \ mm \ mrad \ MeV^{\frac{1}{2}}$$

Table 4.1 shows the acceptance of the LE tubes for various E_T values.

Table 4.1: Low Energy acceptance.

E_T (MeV)	A_{LE} (π mm mrad $MeV^{1/2}$)
1	7.1
2	9.5
3	11.4
4	13
5	14.4
6	15.7

Therefore, the measured emittance from the CAMS/LLNL, ~9.87 π mm mrad $MeV^{1/2}$, which is used in the beam optics simulations, is less than the A_{LE} (as for $E_T \geq 3$) (as calculated from the formula above) for terminal ion energies greater than about 1.5 MeV.

- A set of two Einzel lenses immediately downstream of the ion sources is used to focus the divergent ion beam coming from ion source. These Einzels (positions 3 and 6 in Fig. 4.10, with voltage of -22 kV and -24 kV, respectively) are positioned to act as a zoom lens set that allows control of both the z-axis position of, and the ion-beam divergence at the beam waist being formed before the LE ESA. The Einzel lenses that we use are 3-tube acceleration columns. The following two Einzel lenses (positions 21 and 24 in Fig. 4.10, with voltage of 23 kV and 27 kV, respectively) are used to focus the beam properly for efficient transport to the entrance of the accelerator tubes. As TRACE 3-D is a beam transport program that calculates the beam envelope around the

central transport axis, the sets of vertical and horizontal electrostatic steerers that are used to correct for misalignments of beamline elements, and thereby to keep the beam running along the central transport axis, have not been included in the model.

- The 90° electrostatic analyzer (ESA) functions as 1R-1R double focusing element (position 9 in Fig. 4.10) (Brown and Gillespie, 1999). The ESA has been positioned so that its image position coincides with the object position of the 90° bending magnet as shown in Fig. 4.10. Then the beam line components were constructed so that the upstream bouncer gap would end up located as close as possible to that ESA image/90° magnet object position i.e. it was the position of the object of the 90° bending magnet that determined where the ESA would be positioned. The most important function of the ESA is that, in combination with low-energy analyzing magnet, it forms a mass-dispersive energy dispersive system that compensates for the energy spread in the beam arising from energy loss in the ion source.

- The 90° bending magnet (position 14, 15 and 16 in Fig. 4.10) rejects unwanted ions from the AMS system. The value of ME/q^2 = 15.6 MeV amu is the maximum capability of iThemba bending magnet in LE system, (where M is the mass, E is the kinetic energy, and q is the charge) are correctly deflected and continue to the next stage. At this point, q = -1, and the kinetic energy E is set by the previously applied accelerating potential. The bending magnet has a 608 mm radius, a mass energy product of 15.6 MeV, a 94 mm pole gap, an entry angle of 30° and an exit angle of 28°. The second bouncer gap was located as close as possible to the position of the image waist of the magnet in order to minimize possible isotope dependent focusing and steering effects that might be introduced by the changing bouncer voltages during isotope switching. The last Einzel lens (positions at 21 and 24 in Fig. 4.10) is used to match the ion-beam diameter to the acceptance of the low energy accelerator tubes.

- In a sequential injection system, isotopes are injected one after the other. The vacuum chamber of the 90° bending magnet is electrically isolated. A voltage applied to the vacuum chamber changes the energy of the ions that pass through the magnetic field. The voltage determines the mass of the injected ions. Bouncing is the cyclic change of this voltage for the injection of a sequence of isotopes. The bouncer gaps are two-tube acceleration columns that have been used to simulate the insulating gaps that electrically isolate the magnet vacuum chamber from the upstream and downstream beamlime components (Gillespie and Brown, 1999). The first bouncer gap, at position 12, is used for acceleration (at 2 kV) and the second bouncer gap, at position 18, is used for deceleration (at -2 kV), as illustrate in Fig. 4.10.

- A Q-snout at the entrance of the accelerator is a two-tube column element (position 26 in Fig. 4.10) that was set to give a 20 kV acceleration to the ions as they transited across its voltage gap. The Q-snout was designed to be at the position of a beam waist that the upstream Einzel lens formed at the entrance of the accelerator. The positioning of the Q-snout at this waist is intended to allow the ions to go through an initial acceleration step at the entrance of the accelerator and reduce the strong focusing effects of the change in potential gradient at the entrance to the acceleration tubes.

- The final optical elements of our LE system are the two LE accelerator tubes. The entrance to the low energy accelerating tubes behaves as a strong converging lens. The entrance lens is the most critical optical element in the tube. It is a strong lens with high acceptance. The first of the two LE tubes has 74 active gaps, with the first two gaps each being spanned by 100 MΩ, the next 9 gaps by 400 MΩ ("1/2 value resistors") and remaining 63 gaps by 800 MΩ ("full value resistor"). The second tube has 74 active gaps, all spanned by full value resistors. The effect of the reduced value resistors is a "softer/gentler" acceleration of the incoming ions, and ultimately better beam

transmission through the stripper canal (Roberts et al., 2010). The voltage across each of the first two resistors is 10.525 kV, the voltage across each ½ value resistor is 21.05 kV, in total across all 9 gaps is 231.55 kV. Each full value resistors has 42.1 kV, in total across 63 + 74 gaps has 5767.7 kV. The resistors allow charge flow from the terminal to ground and are used to create and sustain a uniform electric potential gradient along the tube and column from electrical ground at the LE entrance to the terminal at voltage. A well-controlled essentially uniform gradient is required to uniformly accelerate the ions and control their focusing on the stripper. The gap width for 9 gaps is 25.38 x 9 = 228.42 mm, for 63 gap is 25.38 x 63 = 1598.94 mm and for 74 gap is 74 x 25.38 = 1878.12 mm. A waist is desired at the terminal stripper, which is at a distance of 700 mm past the end of the second LE, that can be obtained by varying the voltage of the extractor and Einzel lens of the ion source, depending on the voltage applied to the pre-accelerating tube and cathode of the source. The strongest focusing lens in the column is the fringe field region that exists outside the first accelerating plane. Fringing fields dominate the beam optics of electrostatic accelerating tubes. Whenever the field changes, a single-aperture type lens appears (Zworykin et al., 1945). The effect is pronounced where the fields rise from zero at the entrance (converging lens) and return to zero at the exit (diverging lens) of a normal accelerating tube. The first approximation is that the focal length of an aperture lens (a single circular aperture in a plane electrode separating two regions of different electric field) is given by (Davisson and Calbrick, 1932 and 1931)

$$F = \frac{4V_i}{E_1 - E_2} = \frac{V_i}{\Delta E}, \tag{4.65}$$

where V_i is the potential corresponding to the ion energy. E_1 and E_2 are the fields preceding and following the aperture. The model focal lengths closely matched the formula (Ognibene et al., 2000 and Brown, 2013):

$$F = \frac{2(V_{ex} + V_{ap}) + \sqrt{4(V_{ex} + V_{ap})^2 + 2.28d(V_{ex} + V_{ap})(G\text{ds} - G\text{us})}}{G\text{ds} - G\text{us}} \tag{4.66}$$

where F is the lens focal length in mm, V_{ex} = 39 keV + 20 keV = 59 keV and the second V_{ex} = 39 keV + 20 keV + 94.77 keV=153.77 keV, is the extraction potential, V_{ap} is aperture potential (i.e. 10.53 kV for the first and is 21.05 kV for the second, d = 80 mm, the diameter of the entrance tube, G_{ds} is voltage gradient downstream of aperture and G_{us} is voltage gradient upstream of aperture Therefore, focal lens is F = 720 mm for 10.53 kV aperture potential and F = 1723.3 mm for 21.05 kV.

Figure 4.12 shows the palettes for the LE system. Figure 4.13 shows the results of the beam optics calculations for the LE system along with the beamline elements used in the model and aperture data produced. The results of the beam optics calculations for LE injection system are shown in Fig. 4.13. The two plots at the right and left top are phase plots of the beam profile at both the initial and final positions (in mm). The calculated beam envelope half-widths in both the horizontal (x) and vertical (y) directions are plotted in the bottom half of Fig. 4.13. Note that the sizes of the optical elements are not drawn to scale and in no instance does the beam extend beyond the acceptance of any aperture in the system.

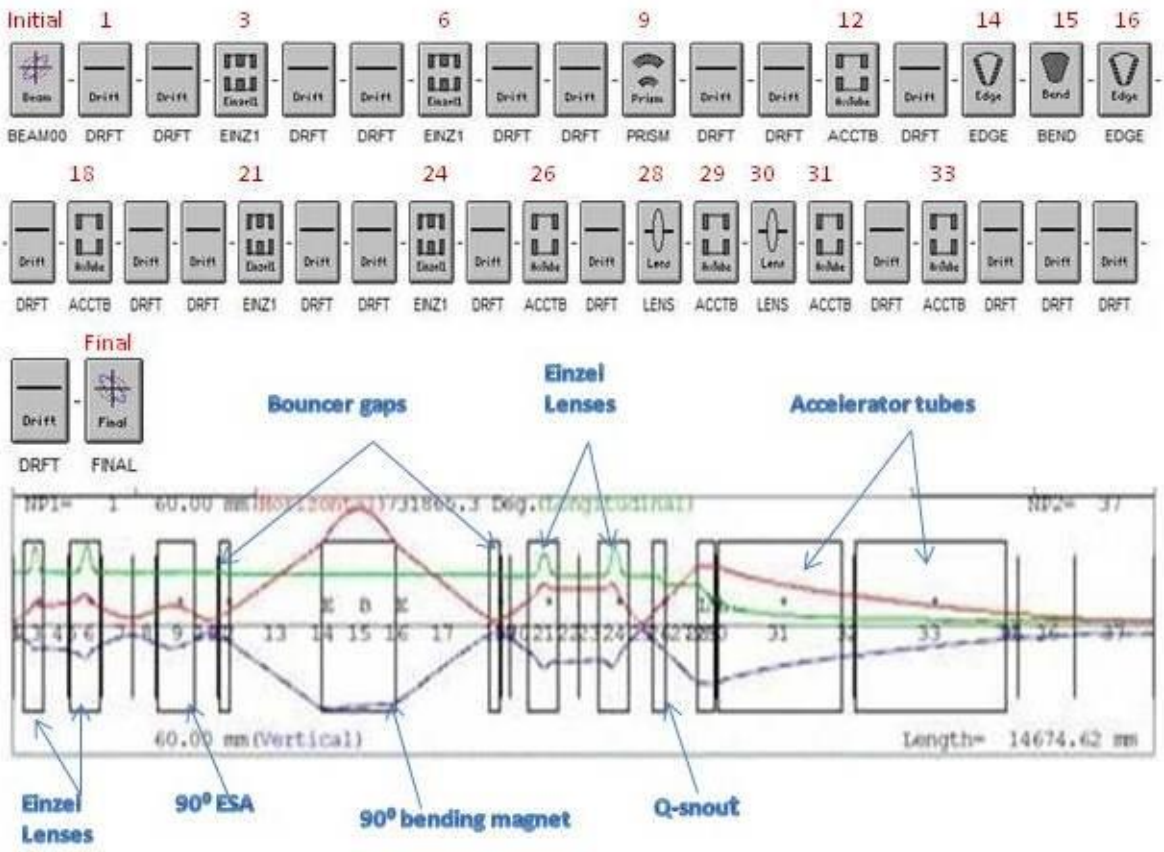

Element	X	Y
1 Drft	2.86	2.86
2 Drft	5.47	5.47
3 Ezl1	11.08	11.08
4 Drft	11.58	11.58
5 Drft	11.59	11.59
6 Ezl1	14.94	14.94
7 Drft	8.87	8.87
8 Drft	8.42	8.42
9 Prsm	10.19	10.19
10 Drft	6.42	6.42
11 Drft	4.67	4.67
12 Tube	8.13	8.13
13 Drft	40.46	40.46
15 Bend	57.12	39.09
17 Drft	40.34	37.67

Element	X	Y
18 Tube	40.34	37.67
19 Drft	6.34	6.27
20 Drft	12.69	12.15
21 Ezl1	21.40	20.31
22 Drft	16.55	15.63
23 Drft	13.86	12.99
24 Ezl1	13.86	12.99
25 Drft	8.76	8.41
26 Tube	12.84	12.17
27 Drft	23.71	22.29
28 Lens	23.71	22.29
29 Tube	23.71	22.29
30 Lens	23.71	22.29
31 Tube	23.71	22.29
32 Drft	9.89	9.23

Element	X	Y
33 Tube	9.89	9.23
34 Drft	3.05	3.14
35 Drft	3.03	3.17
36 Drft	4.17	4.35
37 Drft	7.14	7.16

Figure 4.12: Palettes of LE beam parameters, graphical and aperture data of LE injection of iThemba LABS AMS system.

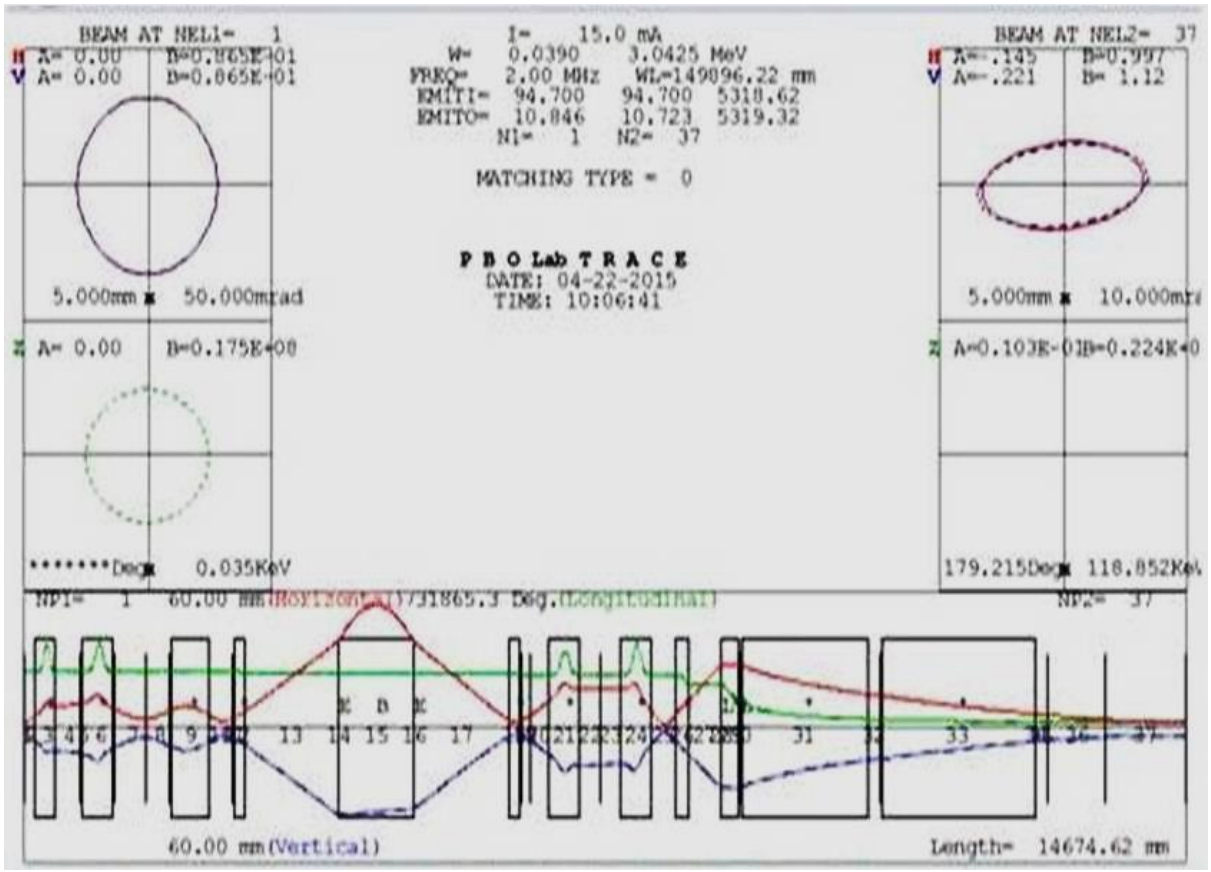

Figure 4.13: Beam optics calculation of beam from ion source to middle of Tandem (LE).

A ^{14}C-carbon beam with ion of charge -1, LE extraction energy of 39 keV and terminal voltage of 3 MV was used in these beam optics calculations for the assessment of the LE beam line. In addition, physical diagnostic tests was performed and compared to the ion optics calculation.

The position of the final beam waist of the LE transport system was defined to be at the midpoint of the gas stripper canal. The negative ion beam from the CAMS/LLNL source is focused to a beam waist 30 cm before the ESA which produces a beam waist 30 cm downstream of the ESA, which is at the object position of LE 90^{o} bending magnet. The 90^{o} bending magnet then forms a beam waist at the image position about ~1.2 m downstream for the magnet and just before the second acceleration gap and a pair of Einzel lenses. The field B in the 90^{o}

bending magnet is set to transmit the mass of ^{13}C without any voltage on the bouncer; for the other masses, the applied voltage to the vacuum chamber change the energy of the ions that pass through the magnetic field are:

$$V_{bouncer} \sim 2.4 \text{ kV for } ^{12}C$$

$$V_{bouncer} \sim -2.5 \text{ kV for } ^{14}C$$

The extraction voltage was 39 kV.

For ^{14}C of 2.5 kV pilot beam with 39 kV extraction voltage, the applied voltages for other masses are:

$$V_{bouncer} \sim 0.3 \text{ kV for } ^{12}C$$

$$V_{bouncer} \sim 3.75 \text{ kV for } ^{13}C$$

The values for x and y radial dimensions of the beam, as measured by the beam profile monitors, positioned at the same places as the predicted waists according to the beam optics calculations, are shown in Fig. 4.14. The calculated trend is very similar to the one measured during the beam tests and the beam envelope seems to be smaller than the calculated one, indicating a rather overestimation of the source emittance in the calculations. An ion source emittance of about 94.7 π mm mrad at 39 keV energy was used in both the horizontal and vertical planes.

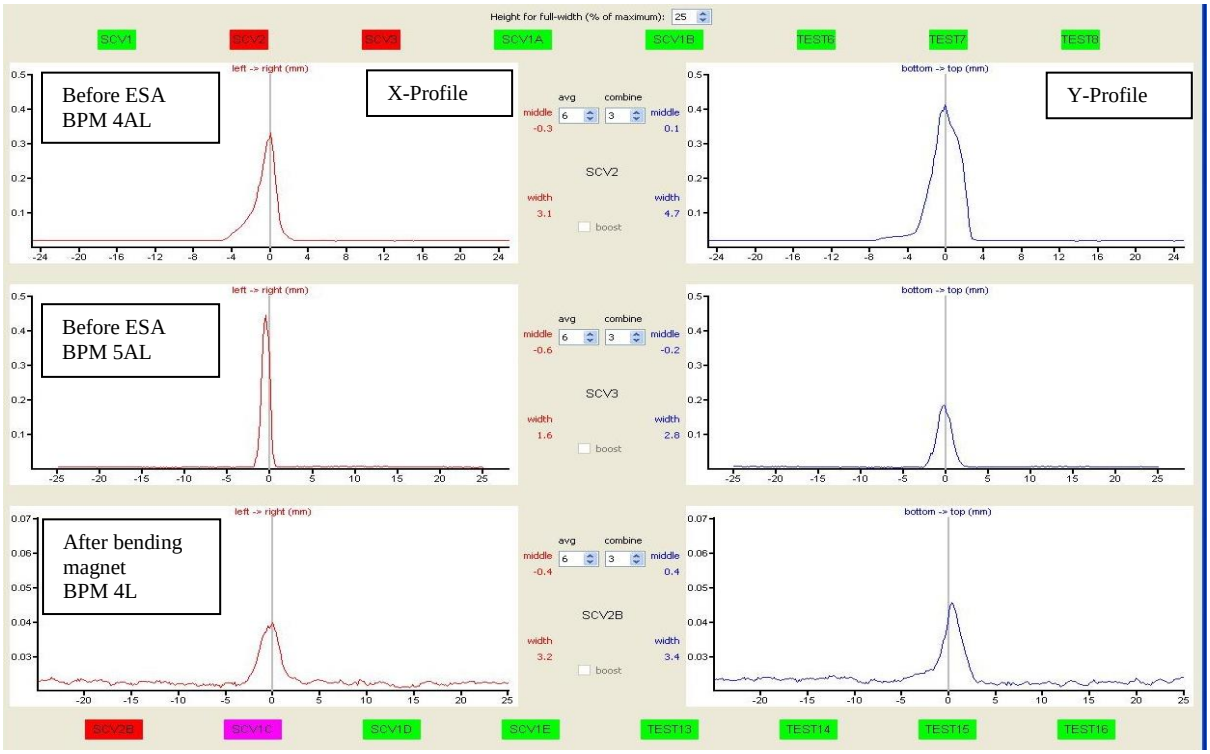

Figure 4.14: Beam profile for the lower energy test.

4.3 Beam Optics Simulations of the HE AMS System

The iThemba LABS HE AMS system is illustrated in Fig. 4.15. The electron-stripped positively charged ions coming out of the high voltage terminal are accelerated towards the ground potential through the HE beam tubes, and then on exiting the accelerator focused by two EQTs and momentum analyzed by the HE analyzing magnet, then focused by MQDs, and analyzed by an ESA, and a second magnet before finally being measured in the detector.

With electrostatic quadrupole triplet, ion beam can be tuned in order to match the acceptance of vacuum chamber and/or ion optical elements to maximize the transported beam current. An electrostatic quadrupole triplet immediately following the accelerator will provide mass independent focusing of the beam, where the stripping to higher

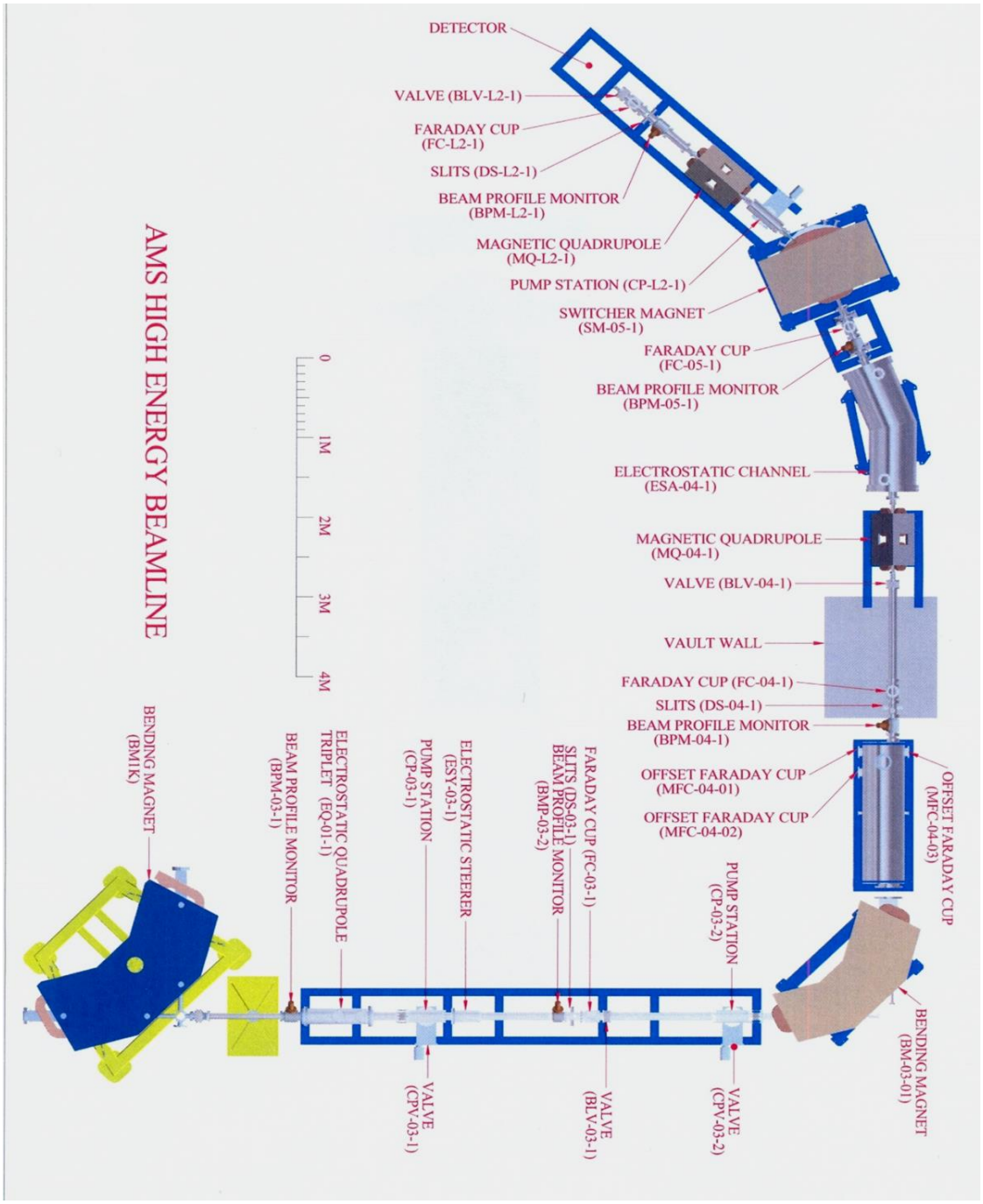

Figure 4.15: HE system for 6 MV Tandem accelerator at iThemba LABS.

charge states will allow rejection of molecular fragments having similar *M/Q*. Momentum and *E/Q* analysis will be performed with magnet and electrostatic analyzer, respectively. The

sequence of the beam line elements that were included in the PowerTrace model of the HE AMS system are shown in Fig. 4.16.

- The high energy accelerating tube has a converging lens effect at the entrance which ordinarily is much weaker than the lower energy. The first tube has 74 active gaps with full resistors, each with the value of 800 MΩ. The second tube has 79 active gaps with full resistors value of 800 MΩ. Each full potential value on a resistor is 21.56 kV, and in total across 74 + 79 gaps is 6598.38 kV. The gap width for 74 gaps is 74 x 25.38 = 1878.12 mm and for 79 gaps is 79 x 25.38 = 2005.02 mm.

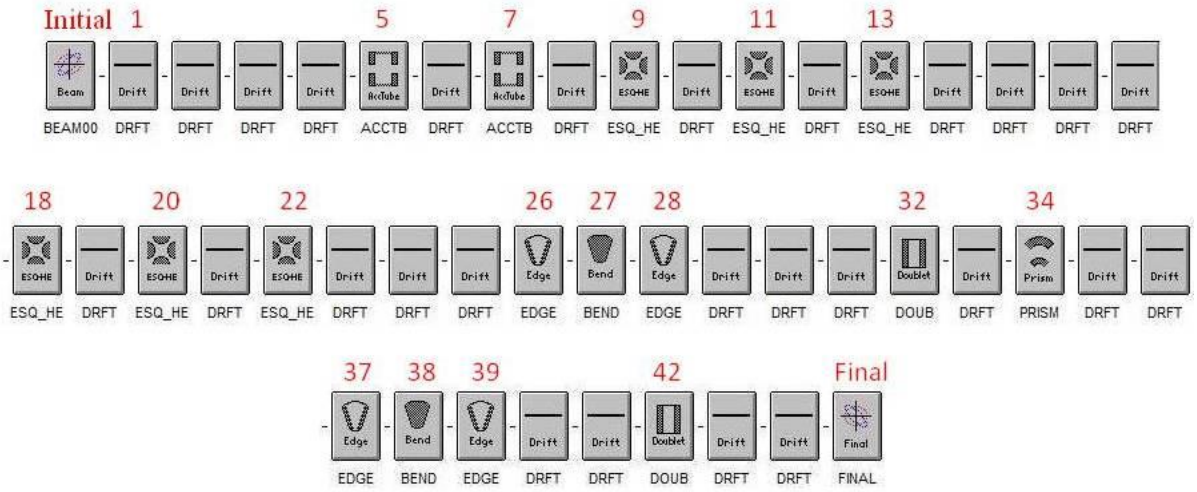

Figure 4.16: The HE palettes of 6 MV Tandem accelerator of iThemba LABS.

A set of two EQT are installed immediately after the exit from the accelerator tank to provide mass independent focusing of the beam. The EQT is used to focus the beam with cylindrical symmetry into a waist forming an object for the AMS analyzing magnet. The first EQT is used to focus the beam through the constriction presented by

the older analyzing magnet for the non-AMS beam lines; the beam then blows up into the second EQT and is focused to form a waist at the object position of the HE AMS 90° Analyzing Magnet. The first EQT has an overall length 1470 mm and a beam aperture radius of 20 mm. The length of the end and mid quad elements are $l_1 = l_3 =$ 288.5 mm, $l_2 = 355.5$ mm, respectively and the separations between the quad elements are $S = 19$ mm. The second EQT has an overall length 640 mm and a beam aperture radius of 22 mm. The length of the end element and mid quad element, are $l_1 = l_3 =$ 162.6 mm, $l_2 = 281$ mm, respectively, and the separation between the quad elements are $S = 14.3$ mm. EQT is uses the following parameters in TRACE 3-D: B'_0 is the magnetic-field gradient measured in Tesla per meter (T/m) in both outer quadrupoles, l_0 is the effective length of outer quadrupole in mm, d is the distance between inner and each outer quadrupole in mm, l_i is the effective length of inner quadrupole in mm and B'_1 is the effective length of inner quadrupole in mm.

- The AMS analysis magnet is a double focusing element with deflection angle of 90°. The magnet has a bending radius of 1.27 m, $ME/Z^2 = 176$, a mass resolution $M/\Delta M =$ 725, a design maximum magnetic field of 1.51 T and a pole gap of 34 mm. The entrance pole face rotation angle is 26.7° and the exit pole face rotation is 26.6° which were set in order to obtain the object and image distance of 2 times bending radius. A chamber immediately following the 90° magnet contains position adjustable Faradays cups that are used to measure the intensity of the abundant isotopes ($^{13}C^{3+}$ and $^{14}C^{3+}$). The stable isotopes are measured in shielded Faraday cups with secondary electron suppression. One of the cups (^{13}C in case of ^{14}C dating) is internally equipped with 2 slits providing information on the beam position.

- Two MQDs lenses are arranged to provide control of the ion beam profiles during transport through the ESA, and switching magnet to the detector. The accelerated beam

leaving the analyzing magnet is diverging and is focused through the ESA by the first MQD of our HE system to a beam waist near the Switch Magnet as shown in Fig. 4.17. It can focus ions with mass-energy product (ME/q^2) up to 50. The pole shapes of the magnetic quadrupole are similar to that of the electrostatic quadrupoles. The effective length of element and the distance of separation between the two quadropoles singlets that make up the doublet are l_e =281 mm, and S = 119 mm, respectively. The aperture diameter of the *MQD*s is 53 mm and uses the following parameters in TRACE 3-D: B'_0 is the magnetic-field gradient measured in (T/m) in both outer quadrupoles, l_0 is the effective length of each quadrupole in mm, d is the distance between inner and each outer quadrupole in mm

- The 22.5° ESA is an energy stigmatic analyzing system and it was placed on the HE beamline to filter out undesirable ions that happen to have the same magnet rigidity as the ions of interest, but don't have the correct mass, or charge state, or energy,etc.. The ESA filters on the basis of E/q and hence it will filter out ions that get around the magnet with the desired $(2mE)^{0.5}/q$ but will not have the desired E/q. It focuses the beam only in the horizontal bend plane because it has cylindrical cross-section electrodes (as opposed to the spherical cross-section electrodes in the double-focusing ESA of the LE injection system). ESA provides non-energy dispersive beam transport. The ESA has a horizontal bend radius of 3.81 m, a 30 mm gap and an energy resolution $E/\Delta E$ = 200. The electric field E required to bend the ions of charge q along the bending radius R, is given by:

$$\frac{mv^2}{R} = qE\,, \tag{4.67}$$

where the kinetic energy, $\frac{1}{2}mv^2 =$ 12.9 MeV, R is bending radius = 3.81 m, and q = 3e. So, the required electric field E is equal to 22.6 kV/cm and since the gap is 3 cm, the voltages on the two plates would have to be ± (22.6 x 3/2) = ±33.8 kV. The input parameters of ESA in TRACE 3D are the following: Bend angle in horizontal, bending angle is 90º degrees and central trajectory radius is 306 mm.

- Lastly, the AMS Switching Magnet was purchased from NEC and has a pole gap of 34 mm and a radius of 1.48 m and mass-energy product of ME/Z^2 = 176. The ^{14}C port is at 25°. The switching Magnet have the beam entering on the straight edge pole face with a pole face angle of 0° and exiting on a curved pole face where the exit pole face angle is about 12.5° pole face angle.

The results of the beams optics calculations for the high energy system are shown in Fig. 4.17 below. Figure 4.18 illustrates the beam optics calculations of higher energy system with the palettes and aperture data included.

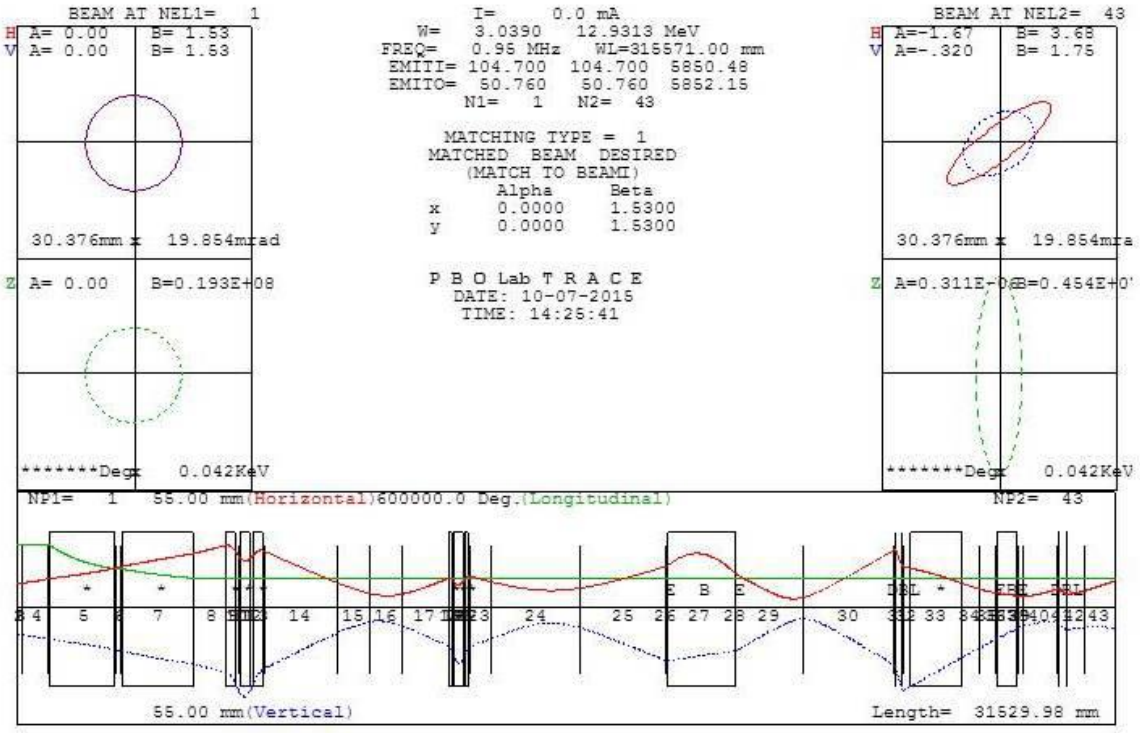

Figure 4.17: Beam optics calculation of beam from middle of Tandem to detector (high energy).

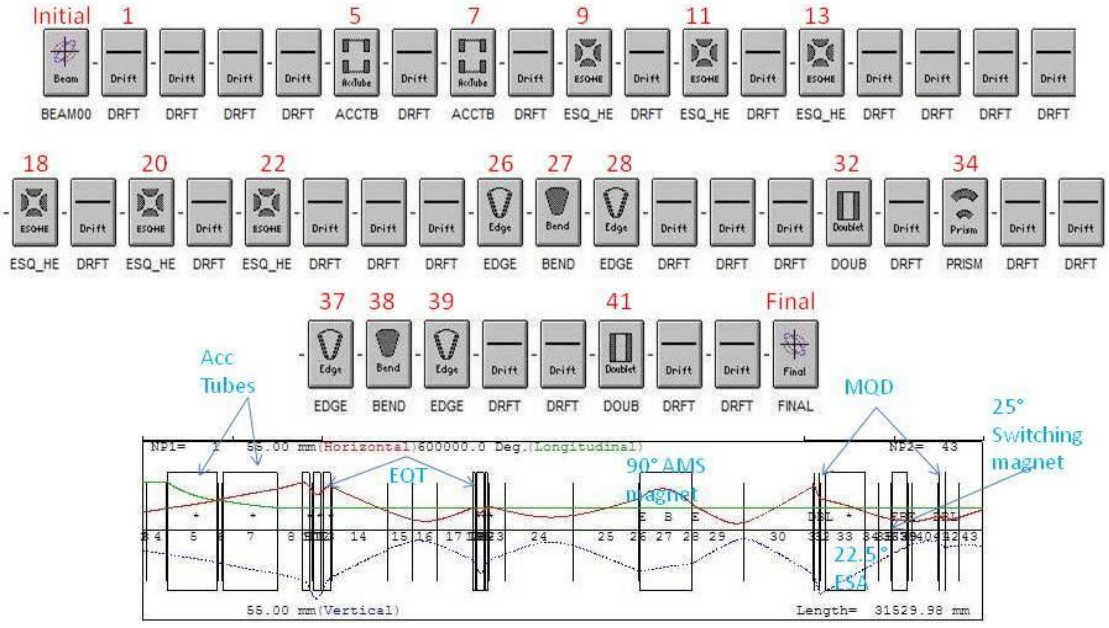

Element	X	Y	Element	X	Y	Element	X	Y	Element	X	Y
1 Drft	12.66	12.66	12 Drft	24.81	37.98	23 Drft	15.87	18.13	40 Drft	9.88	6.6
5. Tube	19.68	19.68.	13 Esq2	26.41	34.75	27 Bend	26.48	23.01	41 Doub	7.3	10.17
6 Drft	20.81	20.81	17 Drft	14.86	17.87	30 Drft	28.36	26.64	42 Drft	8.92	9.2
7 Tube	26.64	26.64	18 Esq2	13.68	22.08	31 Doub	20.41	38.79	43 Drft	13.67	9.43
8 Drft	30.4	30.4	19 Drft	13.4	22.68	32 Drft	20.24	38.67			
9 Esq	27.51	35.92	20 Esq	12.09	25.95	33 Prsm	19.64	37.04			
10 Drft	25.48	38.88	21 Drft	14.07	22.52	35 Drft	9.81	18.9			
11 Esq2	23.26	41.87	22 Esq2	14.46	21.82	37 Bend	7.87	14.56			

Figure 4.18: Palettes of HE beam parameters, graphical and aperture data of HE of iThemba LABS AMS system.

Beam profile dimensions at various points of the HE AMS system were measured and compared to the ion optics calculation with carbon ions of charge +3 at terminal voltage of 3.0 MV; the results are shown in Fig. 4.19. The values for x and y radial dimensions of the beam, as measured by the beam profile monitors, positioned at the same places as the predicted waists according to the beam optics calculations, are shown in Fig. 4.19. The calculated trend is very similar to the one measured during the beam tests. The ion source emittance of 104.7 π mm mrad (rms) at 3.039 MeV and Twiss parameters of $\alpha_x = \alpha_y = 0$ and $\beta_x = \beta_y = 1.53$ m/rad were defined based on results of tests and modeling conducted on an identical source at LLNL.

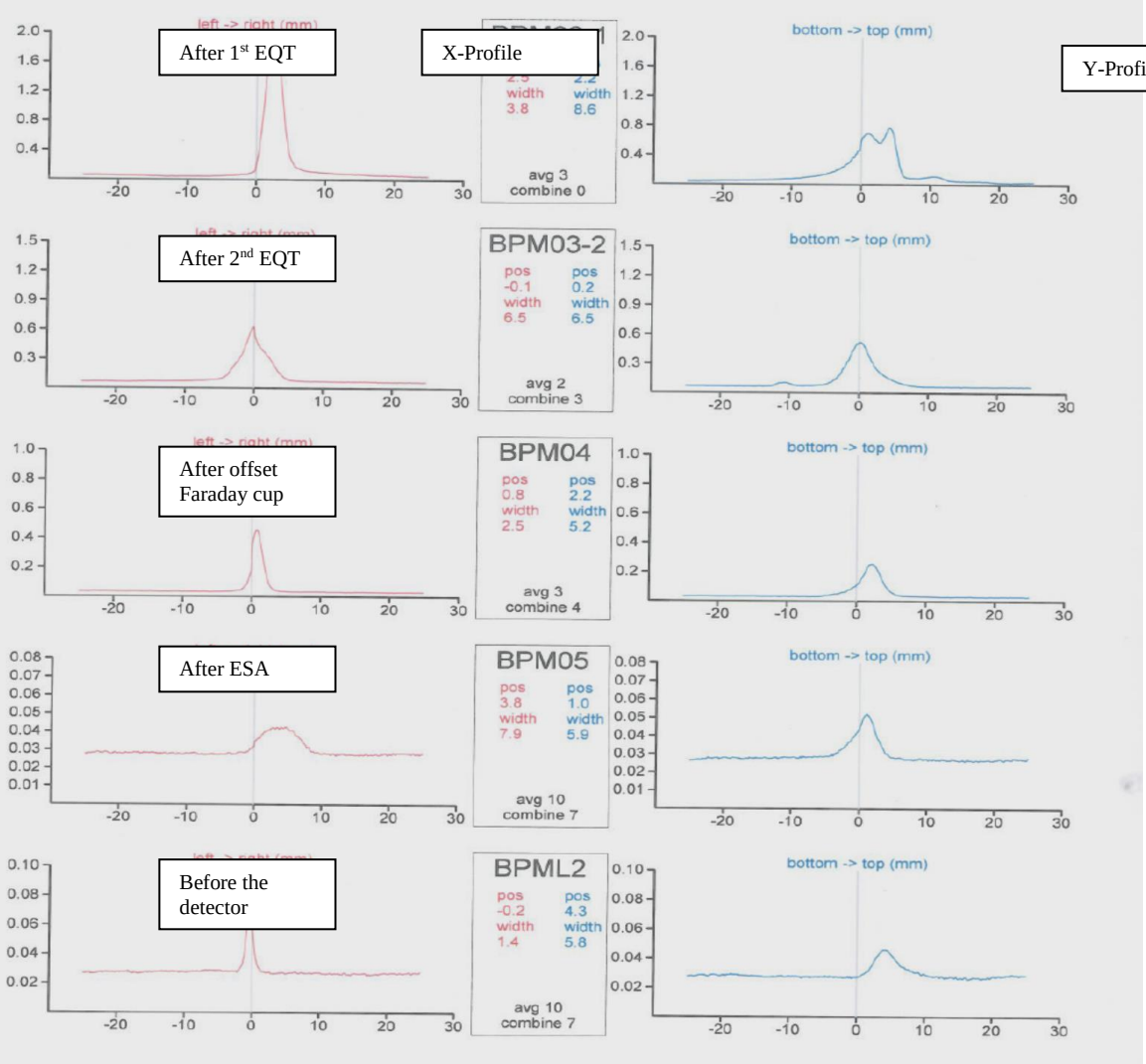

Figure 4.19: Beam profile for the higher energy test.

4.4 Results and discussion

The newly developed AMS system at iThemba LABS has been modeled in terms of its beam optics using the TRACE-3D beam transport code. In this, the initial longitudinal phase space parameters and beam current were adjusted to accurately represent the space-charge fields of the continuous beam in this system. Each particle in a beam is represented by a point in 6-coordinate space of positions and momenta (x, y, z, p_x, p_y, p_z). Only the transverse coordinates (x, y, p_x, p_y) are of interest in matching a beam, propagated along the z-axis without time structure, to ion-optical components.

It is important to note that in the LE injection system starting from the beam source, the first two Einzel lenses are arranged as to form a zoom lens and the other set of Einzel lens is used to match the beam envelope to the acceptance of the accelerator tubes. The first two Einzel lenses allow flexibility in the precise placement of the waist to accommodate changes in the ion source's emittance. Beam profile monitors have been placed through the beam line and a Faraday cup has been inserted between the Einzel lens, just after the beam profile monitor and the 90° ESA to measure total unanalyzed source output. The modeled ESA acts as double focusing beamline element. The ESA image position falls near the first of two 2-tube acceleration column that have been used to simulate the insulating gaps that electrically isolate the magnet vacuum chamber from upstream and downstream beamline components. The energy changes of desired isotope are accomplished by changing the voltage to ground of the magnet vacuum chamber which is electrically insulated. At the gaps between ground and the magnet vacuum chamber, there is an unavoidable gap lens effect so the beam focusing optics is different for the different masses which, in principle could introduce a confounding mass selectivity (Weisser et al., 2014). This focusing effect however, is adequately minimized by locating the gap lens where there beam is small i.e. at beam waists at the object and image of the magnet (Weisser et al., 2014). The potentials 2 kV and – 2 kV are chosen so that the

acceleration in the first gap and subsequent in deceleration the second gap allows the 90° inflection magnet to select mass to be alternated between short pulses of the $^{13}C^-$ ions and longer pulses of the $^{14}C^-$ radioisotopes (Brown and Gillespie, 1999). The highest transmission is obtained by using the Einzel lens to focus the beam to rather broad waist before 90° ESA and keeping the beam wide as it enters the magnet before being focused down to narrower waist at the magnet focal plane.

The accelerator tubes that is two-aperture columns have been used to simulate the section of the beam tubes of the iThemba LABS AMS system. The potentials across these tubes sections are determined by the potential on the central terminal of the accelerator and resistor values between the planes of the accelerator tubes within the section (Brown and Gillespie, 1999).

The magnet image falls near the second acceleration columns and the final Einzel lens (position 21) is used to match the ion-beam diameter to the acceptance of the low energy accelerator tubes. The waist after the low energy 90° magnet must also be far enough away

(for iThemba LABS system, the waist is at 1.197 m) to allow for adequate separation of the $^{12}C^-$ ion beam to enable accurate quantification. The magnet chamber is biased so that the two different mass isotopic beams (^{13}C, ^{14}C) can be sequentially injected into the accelerator at a cycle repeat rate of 100 ms (i.e. 10 Hz) for the new iThemba LABS AMS system. An offset Faraday cup is located near the magnet's image position to measure the beam intensities of lower mass beams (^{12}C, ^{13}C) during higher mass beam injection.

The virtual source position was defined to be midway between the sample and the cesium ionizer. A source emittance of 94.7 π mm mrad at 39 keV and Twiss parameters of $\alpha_x = \alpha_y = 0$ and $\beta_x = \beta_y = 0.0865$ mm/rad were defined for modeling the lower energy side. The final beam emittance of 28.140 π mm mrad at 1.03425 MeV and Twiss parameters of $\alpha_x =$

0.145 mm/rad, α_y = 0.221 mm/rad, β_x = 0.997 mm/rad β_y = 1.12 mm/rad, α_z = 0.0103 mm/rad β_z = 0.224. The equivalent uniform diameter of the beam spot size at the midpoint of the stripper canal is calculated to be 5 mm in the horizontal direction and 5 mm in the vertical direction. The calculated equivalent uniform beam envelopes half-widths through ion transport system is shown two plots on the bottom Fig. 4.13, with the horizontal plane displayed in the top half and the vertical plane on the bottom half. The full scale of each plot is 60 mm. The beam current is 15 mA.

The effect of the reduced value resistors in lower energy injection is a soft/gentle acceleration of the incoming ions, and ultimately ensures a better beam transmission through the stripper canal. The low energy accelerator columns were divided into different voltage gradients, with the first one greater than the second. The larger voltage gradient at the accelerator entrance is required to produce a strong lens which must capture the diverging beam and in a short distance, focus it through the gas stripper canal. The entrance and exit apertures of the acceleration tube were set to zero to negate any TRACE 3-D calculated fringe fields effects and thin lens were inserted to handle the focusing properties of the gradient change at both the entrance to the accelerator and at the interface between the two voltage gradients. The beam optics calculation of the low energy system as shown in Fig. 4.13, indicates that the beam is clearly transported through the injection magnet is well matched to the acceptance of the accelerator tubes, and produces a waist in the stripper canal.

The higher energy beam optics calculations were performed for iThemba LABS AMS system. The first elements of the ion optical elements are two higher energy accelerating tubes. The tubes with electrode arranges such that they optimized to create a electrostatic dispersion, which suppress the influence of unwanted charge exchange processes e.g. the $^{13}C^{4+}$ exchanges to the $^{13}C^{3+}$ in the first part of the high energy tube having then the same magnetic rigidity as the $^{14}C^{3+}$ (Purser, 1992). The beam of interest continues to be analyzed by the first EQT after

accelerator, which provides mass independent focusing of the beam. The beam formulates a waist before the second EQT and another waist before the AMS analyzing magnet. The AMS analyzing magnet image falls at the center between the magnet and the first MQD which is approximately around 2.6 m, since the radius of the magnet is 1.27 m (i.e. 2*R*). The beam is then analyzed by ESA (cylindrical type) which bends the beam in one direction with radius of 1.38 m, then after the beam of interest is switched to the line of interest by switch magnet (25°) which also performs as additional analyzer due to its configuration with entry angle being 0° and exit angle of -12.5°. Then the beam is magnetically focus by a second MQD. Finally the beam is detected at the gas ionization detector.

The virtual emittance position was defined at the middle of the stripper canal. An emittance of 104.7 π mm mrad at 3.039 MeV and Twiss parameters of $\alpha_x = \alpha_y = 0$ and $\beta_x = \beta_y$ = 1.53 mm/rad were defined for modeling the higher energy side. The final beam has the following the energy of 12.9313 MeV and Twiss parameters of $\alpha_x = 0.738$ mm/rad, $\alpha_y = 0.309$ mm/rad, $\beta_x = 1.596$ mm/rad and $\beta_y = 6.938$ mm/rad. The calculated equivalent uniform beam envelopes half-widths through ion transport system is shown two plots on the bottom Fig. 4.17, with the horizontal plane displayed in the top half and the vertical plane on the bottom half. The full scale of each plot is 100 mm. The beam current is 0.0001 mA.

CHAPTER 5
RADIOCARBON AMS SAMPLE PREPARATION

5.1 Sample preparation for radiocarbon

Sample preparation constitutes an essential part of any AMS facility. Such a laboratory, as part of this PhD work, was designed according to the CAMS/LLNL standards and protocols and it has now been completed at iThemba LABS. The sample preparation laboratory for graphitization at iThemba LABS is illustrated in Fig. 5.1. Additional equipment and processes regarding preparation for other isotopes, such as Al, Be, Cl and actinides are in progress and fall out of the scope of the present project.

Sample preparation usually includes certain chemical pretreatment suitable to the different types of samples and extraction of *in situ* carbon material that contains sufficient quantity for a ^{14}C AMS measurement. The main intention of chemical pretreatment is to remove contaminating substances, which can seriously interfere with the dating, and produce a pure graphitic substance representative of the age of the sample itself (Slota et al., 1987). In addition, it is desirable to take into account that the final material which formulates the cathode in the Ion Source of the AMS system should be preferably in a form that will optimize the formation of negative ions in the ion source, as well as chemically enriched with respect to the isotope of interest and chemically purified with regards to interfering isobars.

Figure 5.1: The graphitization line for sample preparation at iThemba LABS.

In the present study, two different sample preparation procedures were followed pertaining to the fact that there were two different categories of samples; one in relation to sample preparation for shells from the archaeological excavation site in Kasteelberg B and the other in relation to quartz filters sampling environmental air pollution in the Lephalale district. The details of the procedures are given below.

5.2 Sample preparation of quartz filter for environmental air pollution

The quartz-fiber filter for each sample was sliced, and all slices were place in a test tube together with 200 mg of CuO and glass wool on the top of test tube. Samples were sealed using acetylene/O_2 torch gas. Subsequently, they were placed in an oven for combustion over

5 hours at 900°C. After combustion, the samples are allowed to cool over at least 4 hours, preferably overnight.

The CO_2 produced during combustion must be isolated and trapped and finally converted to elemental carbon through the graphitization Bosch reaction (Manning and Reid, 1977) is using Fe as catalyst at 550-650°C (Vogel et.al., 1987):

$$CO_2 + 2H_2 \rightarrow C + 2H_2O. \quad (5.1)$$

The vacuum lines are made of glass and stainless steel as seen in Fig. 5.2. The combusted CO_2 is purified through a series of cryogenic traps. The first trap is maintained at -78°C with a dry ice/isopropyl alcohol slurry to remove water vapor. The second and third traps are maintained at -196°C using liquid nitrogen to condense sample CO_2, non-condensable gases are pumped away. The frozen CO_2 is warmed and allowed to sublime and the evolved gaseous CO_2 is then transferred into the graphitization reactor. Manganese perchlorate ($Mg(ClO_4)_2$) is used in the second arm of the graphitization reactors to absorb the water vapor produced during the graphitization reaction. The CO_2 is moved to a trap of known volume and CO_2 is allowed to warm to room temperature; then the pressure in the trap is measured and the mass of carbon in the isolated sample is determined using the measured pressure and the known volume of the trap. The gas pressure of each graphitization reaction is monitored by a PC.

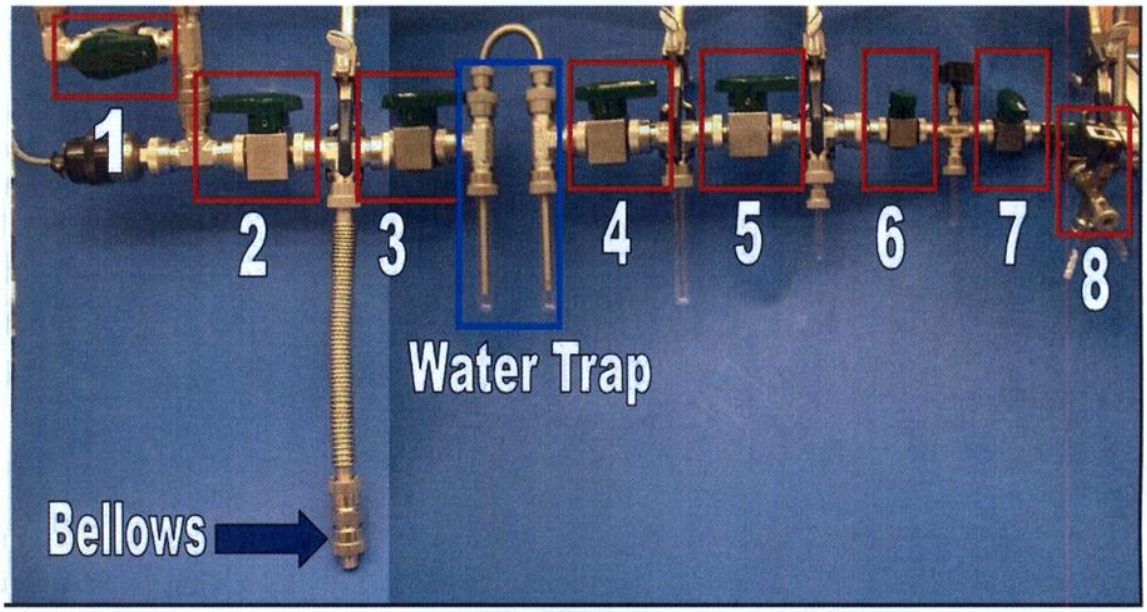

Figure 5.2: Picture showing the main section of the University of California (Irvine) sample preparation line of the graphite target with labelled valves (UCI, 2012).

For the graphitization reaction step, an aliquot of the isolated sample CO_2 is transferred to a further reaction vessel (graphitization reactor) that has two arms and a pressure measuring transducer (see schematic diagram Fig. 5.3). The graphitization reaction containing 5 mg of Fe powder and 2.5 mg of $Mg(ClO_4)_2$ and Fe is heated to 550°C. The Fe reduces the CO_2 to graphite coating on the Fe powder, and $Mg(ClO_4)_2$ in the second arm of the reactor absorbs the H_2O produced during graphitization. Finally, the obtained graphite powder was pressed into a small-diameter hole in a target pellet for the AMS ion source.

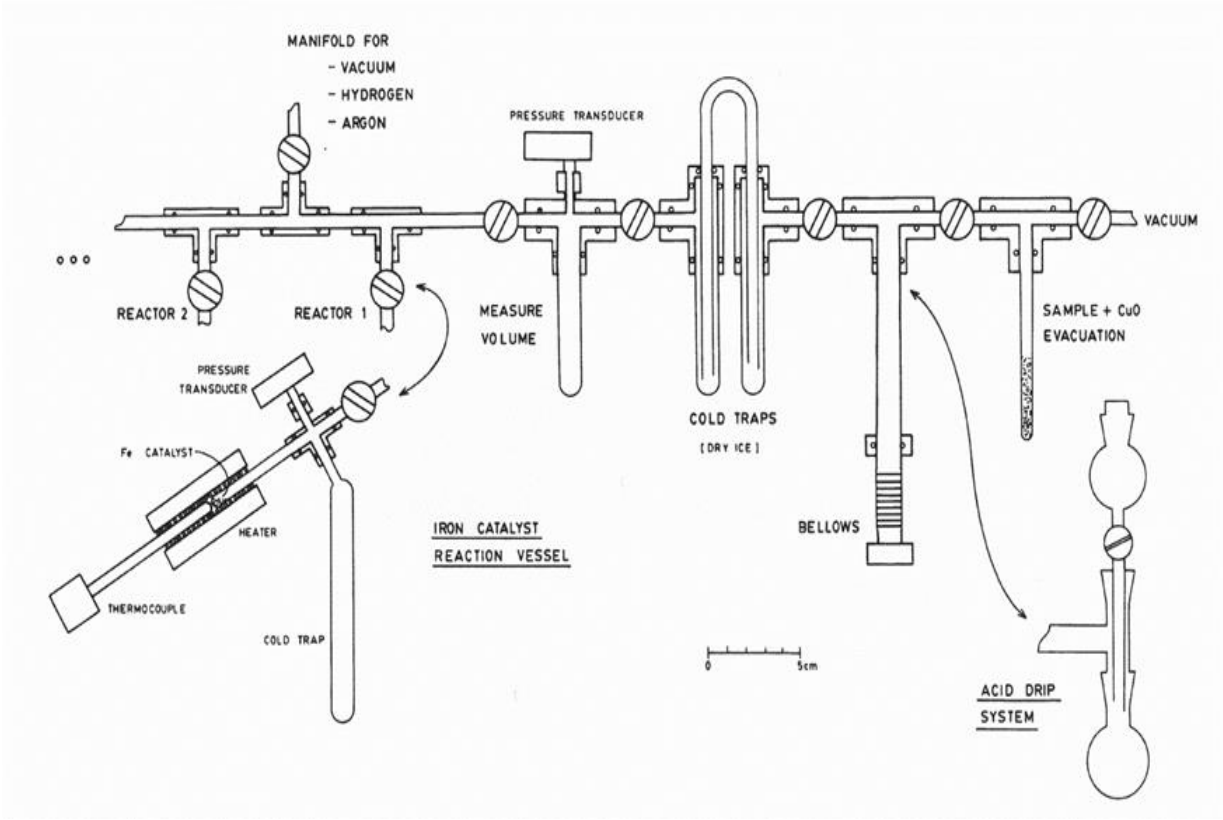

Figure 5.3: Multiple reactor apparatus for the graphitization of CO2 over an iron powder catalyst. The volume of reaction vessels could be varied by using different sized cold traps (Vogel et al., 1987).

5.3 Sample preparation for shells samples for AMS measurements

The sample preparation was carried out at LLNL in order to remove contaminants, combust the samples and ultimately carbonise them. Firstly, each sample was treated following the Acid-Base-Acid (ABA) method where upon the sample is mixed with 0.0001 N hydrochloric acid (HCl) and the mixture is heated to 95°C. Sodium hydroxide (NaOH) 1N was then added to the sample. Base wash was repeated until NaOH is almost completely clear. Each sample underwent a minimum of two base washes. HCl was removed from the sample by putting milli-q deionized water and milli-q was then removed from the sample using a pasteur pipette. Approximately 5-10 mg samples, an appropriate amount to yield 1 mg -carbon targets, are sealed in glass tubes and evacuated to 10^{-3} Torr. The pretreated shell samples were then

underwent the same graphitization procedure as described above using the same graphitization reactor line.

5.3 Sample preparation for Standards

^{14}C reference materials (Standards) were prepared at CAMS/LLNL using slightly different procedures. Sucrose from ANSTO, Oxalic acid materials such as Oxalic acid I and NIST Oxalic acid II are used as standards in most radiocarbon laboratories. Oxalic acid I and Oxalic acid II must be combusted to form CO_2. The same combustion procedure as in the case of quartz filter samples was followed. In this, the Oxalic acids are heated in 900°C oven in the presence of CuO. Each combustion batch produces 300-500 μmol C (4-6 mg C) in CO_2 gas.

5.4 Cathode Carbon Pellets

The graphitized powder from the samples is used to form a small 1 mg carbon pellet which is inserted in a cylindrical hollow sample holder that constitutes the cathode of the negative ion source. The sample holders are held in place using side-mounted ball-nosed spring plungers. Sample holders are made of aluminum and are ~6.3 mm in diameter by 12.7 mm long. The sample hole is "blind" and is 1 mm diameter by 2 mm deep. The sample hole is drilled "dry" just prior to sample pressing to assure no cutting fluid residues are in the hole. Graphite is front-loaded using a hammer and drill blank. The tapered front surface of the sample holder acts as a funnel to assist in the front-loading process. The holders are large enough to be easily labeled, reducing the probability of inadvertently swapping samples. The samples, in the graphite power, are loaded into the aluminum target holder. The loaded holder is then transferred to the wheel of the ion source which can accommodate 64 aluminum sample targets/cathodes as seen in Fig. 5.4.

Fig. 5.4: The 64 sample holder wheel of the CAMS/LLNL negative ion source.

Finally, the prepared graphite targets/cathodes are transported for AMS spectrometer measurements. CAMS/LLNL ^{14}C dates are based on $^{14}C/^{13}C$ ratios to obtain specific ^{14}C activities. Measurements of the $^{14}C/^{13}C$ ratios of the samples to be dated are determined relative to the respective NBS oxalic acid I or oxalic acid II standards values and three background samples from graphite derived from a ^{14}C free CO2 gas, coal or C-1 standard of IAEA. Radiocarbon age data are presented according to the conventions of Stuiver and Polach (1977). This means that by convention, the ^{13}C isotopic fractionation in all samples, irrespective of environment, is taken into account by normalizing to–25 per mil with respect to PDB. All samples of unknown, standards and blanks of one series are measured several times (typically three or four). The total measured times per sample is around 20 to 30 minutes.

CHAPTER 6
ENVIRONMENTAL ASSESSMENT OF THE AREA AROUND THE LEPHALALE COAL-FIRED POWER STATION USING AMS AND PIXE TECHNIQUES

6.1 Application to Environmental samples

6.1.1 *Lephalale-Marapong Sampling*

The identification of different sources of combustion particles and their apportionment in environmental samples is important; the potential effects of such particles on human health, visibility and climate change is becoming more widely recognized (Dockery et al., 1993; Lewis et al., 1988). AMS measurements are able to distinguish between different anthropogenic sources of air pollution and particles due to its unique ability to discriminate fossil-fuel based carbon containing material (which contain practically no ^{14}C), from contemporary (modern-^{14}C containing) carbon materials (Currie, 1984; Szidat et al., 2004; Szidat et al., 2009; Schichtel et al., 2008).

The ability of AMS to provide measurements of very small amounts of sample material (a few hundred μg of carbon), such as from air-samples containing minute amounts of carbon-containing-matter, particularly for samples taken in clean areas far from industrial cities, has enabled the accomplishment of atmospheric pollution source apportionment in some settings (Currie, 1984; Currie et al, 2000a, Szidat et al., 2004; Szidat et al., 2009; Schichtel et al., 2008). An extreme example of such studies has been the successful determination of ^{14}C in elemental or "black" carbon (BC) occurring at levels of 2-10 mg per kg of Greenland snow and ice (Currie et.al, 2000b).

In the present study, AMS has been applied in analyzes of environmental samples collected in the Lephalale municipality. Lephalale is a predominantly rural municipality with 38 villages, two townships Marapong and Onverwacht and one town known as Lephalale, which is located in the Limpopo Province of South Africa. Lephalale is situated between 23°30´ and 24°00´ south latitude and 28°00´ east longitude. In Marapong and Onverwatcht and some other surrounding informal settlements, there are some houses which still use coal, paraffin and wood as fuel sources. Other sources of concern to air quality in the Lephalale area are brickworks operations, agricultural activities, biomass burning, fossil-fuel powered vehicle operations and other fugitive dust/aerosol emissions. The town is at an elevation of 820 meters above sea level and is positioned west of the Moloko River, a tributary of the Limpopo River.

The regional climate is hot with average temperatures ranging from 22.3°C in June to 31.9°C in January. The Limpopo region is South Africa's northernmost area and is bisected by the tropic of Capricorn. The regional climate is typified by long summer afternoons and dry days. The capital city of Limpopo, Polokwane (previously known as Pietersburg) lies more or less in the centre of Limpopo Province. Lephalale normally receives about 400 mm of rain per year, with most rainfall occurring during mid-summer.

The Lephalale town is growing rapidly and more industries are becoming concentrated within the small town. The new developments include expansion of the local Grootegeluk coal mine, a new shopping complex, various road developments, the Firestone Energy/Sekoko thermal coal mine and Medupi coal-fired power station. Medupi power station is a dry-cooled coal-fired power station consists of six units that will together generate 4,800 MW. The Medupi power station will be similar to Matimba in terms of operation. The power plant accommodates six boilers, each powered by an 800 MW turbine. The boilers are expected to be more efficient and operate at high temperatures and pressures than previous generation boilers. Matimba is also a dry-cooled coal fired power station with six units of 665 MV turbo-generator that

together generate 4,000 MW. The adjacent Grootegeluk colliery has sufficient coal reserves to guarantee Matimba a minimum lifespan of 35 years, extending to a possible 50 years at 2100-2130 tons of coal per hour. Figure 6.1 shows the map of the study area including adjacent coal-fired power stations.

The sampling area for this study is in the vicinity of the existing Matimba coal-fired power station at Lephalale as well as the vicinity of the under-construction Medupi coal-fired power station. The Medupi coal burning power station (with 4.8 GW capacity) will be, the third largest coal burning power station in the World, when it starts operations by the end of 2015 (expected).

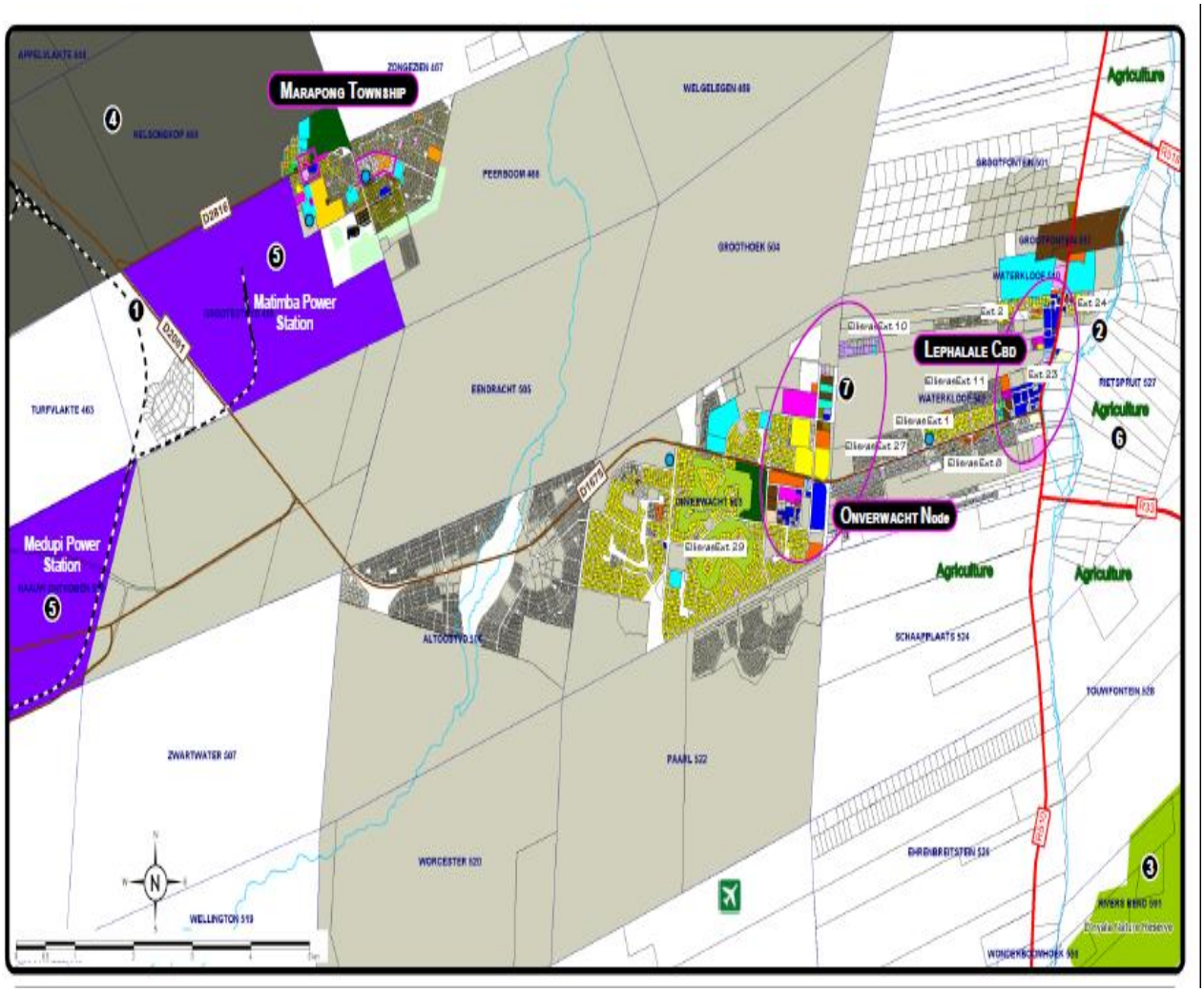

Figure 6.1: The map showing the study area at Marapong Township in Lephalale.

Radiocarbon measurements are going to be used to distinguish between pollution contributions due the coal-fired power station and wood burning activities in the area. The radiocarbon measurements were also complemented with Proton Induced X-Ray Emission (PIXE) analyzes of a range of aerosol samples collected from the same Lephalale area. PIXE is a trace element analysis technique providing ppm sensitivity measurements of many (essentially spanning the entire periodic table) elemental abundances in the particulate matter collected the samples.

Samples for both AMS and PIXE analysis were collected using a Partisol-plus 2025 Sampler with a flow rate of 16.7 l/minute (1 m^3/h) with a PM_{10} porous filter inlet. The AMS quartz-fiber filters used for the collection of the aerosol samples were pre-fired by baking at 500°C for 6 hours (in order to reduce their carbon blank) and then stored in sealed holders prior to use. The samples were collected daily from 9h00 to 21h00 and from 21h00 to 9h00 during the period between 20 March and 04 April 2012. Over the course of the collections the prevailing wind direction was south-eastly. The mass of the samples collected on the filters were obtained through gravimetric measurements, of filters before and after exposure using a 0.1 µg sensitivity electronic microbalance (which was in a controlled atmosphere room (20°C, 50% relative humidity). A picture of the Partisol-plus Sampler that was used for sampling with quartz-fiber filters is shown in Fig. 6.2.

Figure 6.2: Partisol-plus sampler (Rupprecht & Patashnick, 2012).

The exposed quartz-fiber filters were placed into holders and were transported to the Center for Accelerator mass Spectrometry (CAMS) at the Lawrence Livermore National Laboratory (LLNL) for ^{14}C analyzes. There, the organic aerosol is combusted and the released CO_2 is used to quantify the amount of carbon and the isotopic fraction ratio is measured. In this case the CO_2 is converted to a form of graphite for AMS analysis (i.e. to convert air pollution carbon into graphite for AMS analysis). An AMS sub-milligram carbon target was prepared for each sample using the well-established graphitization process at CAMS/LLNL described below.

6.1.2 *Measurements and methods*

^{14}C analysis is based on sequential injection of mass 14 and mass 13. The system allows measurement a sequence of unknown samples, of radiocarbon standards NBS Oxalic Acid I (NIST-SRM-4990 and, Oxalic II (NIST-SRM-4990C), and also graphite derived from ^{14}C free CO_2. Control samples were made by adding Hepta methyl nonane (HMN) onto the quartz-fiber filter blanks in order to introduce carbon on the blanks and HMN was also added to

unknown samples to act as "carrier" throughout processing. In addition, coal and/or the blank IAEA C-1 standard Carrara marble was also measured in order to evaluate possible contamination or systematic errors. For measurements, all 18 samples, plus blanks and standards were mounted on a 64-sample holder wheel of the CAMS/LLNL Cs-sputter negative-ion source. Every group of samples processed includes an appropriate blank, which is analyzed concurrently with the group. In general, a group is composed of 10-14 unknowns with intervening and bracketing primary standards. Samples are analyzed in such a way that a single group is completely analyzed prior to proceeding onto the next. A group is analyzed repeatedly such that a suite of bracketing primary standards and secondary standards are analyzed in conjunction with the unknown samples (Guilderson et al., 2003).

During the AMS measurements of ^{14}C, the terminal voltage used was 6.5 MV; this corresponds to an approximately maximum 4+ fraction of the ions produced in equilibrium charge state stripping of the injected negative carbon ions in transiting a thin 4 μg/cm^2 carbon stripper foil in the terminal. The 4+ carbon ions produced in this stripping process exit the accelerator with an energy of about 32.5 MeV. The LE $^{12}C^-$ ion currents from the source were in the range of 250 μA and the resulting HE currents were about 5 μA $^{13}C^{4+}$. The ^{14}C data were reported as fraction modern carbon (F_M), following the nomenclature of Reimer (Reimer et al., 2004), as in Eq. (6.1).

Table 6.1 below shows the ^{14}C AMS measured values from the Marapong town. The fraction modern carbon aerosols samples in PM from Marapong Township over the sampling period are shown in Fig. 6.3. Though most of the sampling period the fraction modern carbon is approximately 0.51 and the average is 0.53. There is no wind direction data of the sampling site; the wind data is available from South African Weather Service (SAWS).

Table 6.1: **Marapong data with radiocarbon age analyzed at LLNL**

CAMS #	Sample Name	Other ID	$\delta^{13}C$	Fraction Modern	±	^{14}C age	±
160591	**Marapong-3**	**N103646**	**-25**	**0.5556**	**0.0024**	**4720**	**40**
160592	**Marapong-4**	**N103647**	**-25**	**0.5037**	**0.0021**	**5510**	**35**
160593	**Marapong-7**	**N103650**	**-25**	**0.5365**	**0.0022**	**5000**	**35**
160594	**Marapong-8**	**N103651**	**-25**	**0.4990**	**0.0029**	**5585**	**50**
160595	**Marapong-9**	**N103652**	**-25**	**0.5243**	**0.0027**	**5185**	**45**
160596	**Marapong-11**	**N103654**	**-25**	**0.5783**	**0.0031**	**4400**	**45**
160597	**Marapong-13**	**N103655**	**-25**	**0.4664**	**0.0034**	**6130**	**60**
160598	**Marapong-14**	**N103656**	**-25**	**0.5757**	**0.0027**	**4435**	**40**
160599	**Marapong-17**	**N103659**	**-25**	**0.5331**	**0.0030**	**5055**	**50**
160402	**Marapong-5**	**N103648**	**-25**	**0.5445**	**0.0067**	**4880**	**100**
160403	**Marapong-10**	**N103653**	**-25**	**0.5164**	**0.0079**	**5310**	**130**
160404	**Marapong-15**	**N103657**	**-25**	**0.5113**	**0.0077**	**5390**	**130**
160405	**Marapong-19**	**N103661**	**-25**	**0.4945**	**0.0048**	**5660**	**80**
160406	**Marapong-21**	**N103664**	**-25**	**0.3882**	**0.0054**	**7600**	**120**
160649	**Marapong-18**	**N103660**	**-25**	**0.6104**	**0.0030**	**3965**	**40**
160650	**Marapong-20**	**N103663**	**-25**	**0.6711**	**0.0031**	**3205**	**40**
160651	**Marapong-22**	**N103665**	**-25**	**0.5337**	**0.0025**	**5045**	**40**
160652	**Marapong-23**	**N103666**	**-25**	**0.4658**	**0.0033**	**6140**	**60**
160653	**HMN-1**	**N103798**	**-28**	**0.0027**	**0.0001**	**47640**	**220**
160654	**HMN-2**	**N103799**	**-28**	**0.0044**	**0.0001**	**43510**	**170**

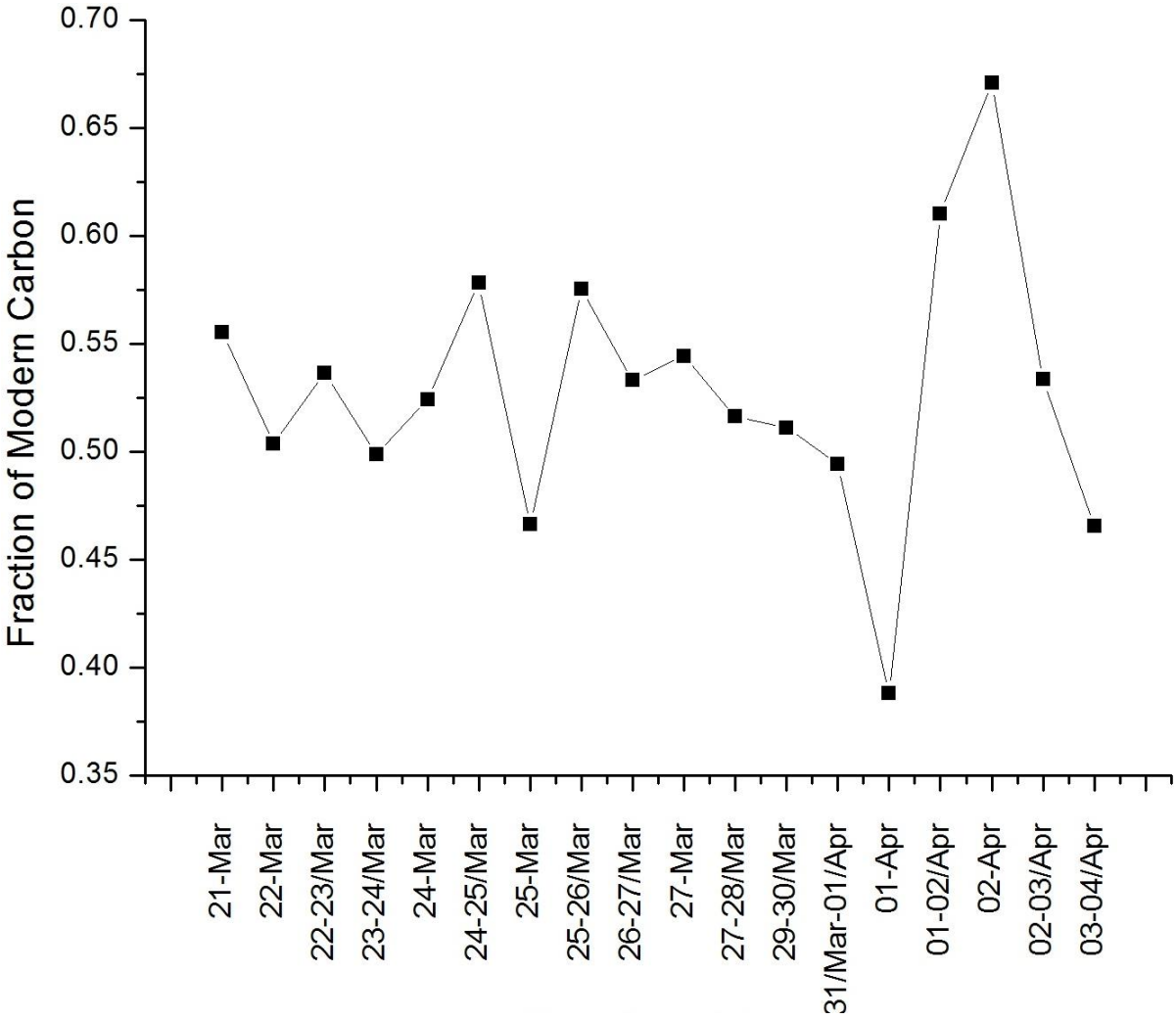

Figure 6.3: Fraction of modern carbon in aerosol samples collected at Lephalale.

The data were reported as a fraction of the modern radiocarbon standard (Fraction Modern or F_M) (Stuiver and Polach, 1977). At the CAMS/LLNL facility, radiocarbon ages are determined by measuring the ratio ($^{14}C/^{13}C$) in a sample and comparing that ratio with similar measured for known standards. The $\delta^{13}C$ are assumed to be -25‰ for all samples in order to correct the radiocarbon measurements for isotopic fractions effects. The fraction of modern carbon was calculated as follows:

$$F_M = \frac{\left(^{14}C/^{13}C\right)_{\text{sample}}}{\left(^{14}C/^{13}C\right)(1950)} \tag{6.1}$$

The $^{14}C/^{13}C$ ratios of the samples and standards are both corrected for machine background and normalized for fractionation to $\delta^{13}C = -25‰$.

The $\delta^{13}C$ values are given by the equation:

$$\delta^{13}C = \frac{\left(^{13}C/^{12}C\right)_{sample} - \left(\frac{^{13}C}{^{12}C}\right)_{PDB}}{\left(^{13}C/^{12}C\right)_{PDB}} .1000‰ \quad (6.2)$$

The extent of isotopic fractionation can be measured by determining the $^{13}C/^{12}C$ ratio in an ordinary mass spectrometer or by AMS. The isotopic ratio of the sample of international standard PDB, where PDB is an abbreviation for the belemnite formation (carbonate) at Peedee in South Carolina and has a $\delta^{13}C$ value of 0‰ by definition. Wood and most plants in the temperate zones have a $\delta^{13}C$ of about -25‰. For a better comparison, especially for the calibration to the actual calendar age with the data set of the dendrochronology-based calibration curve, it is an internationally accepted practice in radiocarbon laboratories to correct radiocarbon results for sample fractionation to a $\delta^{13}C$ value.

The Radiocarbon Age (t) of sample is calculated using the equation:

$$t = -8033 \ln F_M . \quad (6.3)$$

where -8033 represents the Libby mean life (Stuiver and Polach, 1977). According to Stuiver and Polach (1977). Most radiocarbon laboratories calculate the radiocarbon age of a sample from the equation:

$$t = -8033 \ln \frac{A_{SN}(1950)}{A_{ON}(1950)}, \quad (6.4)$$

where A_{on} is the activity in counts per minute of the modern standard while A_{sn} is the normalized specific activity of the sample.

For the measurements of $^{14}C/^{13}C$ ratios, the equation is:

$$(^{14}C/^{13}C)_{1950[-25]} = 0.9558(^{14}C/^{13}C)_{OX[-19]} = 0.74598(^{14}C/^{13}C)_{NOX[-25]}, \quad (6.5)$$

where OX is the Oxalic standard which is known as Oxalic acid I and NOX is National Institute of standards and Technology, Standards Reference Material 4990C Oxalic Acid which is known as Oxalic acid II.

During the measurements, the $^{14}C/^{13}C$ ratios of the samples were determined and expressed in the internationally used modern fraction (F_M).

By measuring the ^{14}C content of ambient aerosols, along with the $^{13}C/^{12}C$ isotopic ratio to correct for isotopic fractionation processes, F_M in aerosol samples can be determined, and the nominal fraction derived from fossil combustion, F_F is calculated as $1-F_M$. Contemporary carbon emission includes fireplace combustion of wood, cigarette smoke, food cooking operations, paved road dust containing ground-up leaf material, brake lining dust and natural rubber in tire dust (Hildemann et al., 1994).

Most indigenous people in rural South Africa as well as the townships (ghettos) live under poor conditions. Certain parts of the country have no electricity or people lack the financial resources to pay for it. It is therefore common for people in these areas like Marapong and Onverwatcht and other surrounding informal settlements to use firewood for cooking and heating. A large amount, therefore, of the carbon on the filters in this study is assumed to originate from local burning of wood, which contains contemporary carbon.

The fossil carbon fraction (F_F) value is determined from contemporary fraction carbon (F_C) value in such a way that the carbon being not firewood or modern biogenic origin in the

aerosol, is considered to be that of fossil origin (Levin and Hesshaimer, 2000). The fraction of fossil carbon is given by:

$$F_{\mathrm{F}} = 1 - F_{\mathrm{C}} \tag{6.6}$$

The total carbon mass from each sample was measured at the end of the CO_2 purification steps just before transfer to the graphitization reactors. The contemporary carbon fraction is product of fraction modern and measured carbon mass. The fossil carbon is derived from contemporary carbon as in Eq. (6.6). Table 6.2 shows Marapong data analysis.

Table 6.2: Marapong data analysis

Sample name	Mass after (mg)	Mass before (mg)	Mass difference (mg)	Measured CO_2 (mg of C)	Measured CO_2(%)	Fraction Modern (F_m)	Contemporary carbon fraction {F_c (mg of C)}	Fossil carbon fraction (F_f)	F_f (mg of C)
Marapong_3	155.98	153.66	2.32	0.161	6.94	0.5556	0.089	0.4444	0.072
Marapong_4	153.37	151.38	1.99	0.255	12.81	0.5037	0.128	0.4963	0.127
Marapong_5	153.73	152.73	1	0.153	15.3	0.5445	0.083	0.4555	0.07
Marapong_7	150.12	149.56	0.56	0.244	43.57	0.5365	0.131	0.4635	0.113
Marapong_8	155.22	151.76	3.46	0.122	3.52	0.499	0.061	0.501	0.061
Marapong_9	151.87	150.58	1.29	0.138	10.7	0.5243	0.072	0.4757	0.066
Marapong_10	153.87	153.13	0.74	0.127	17.16	0.5164	0.066	0.4836	0.061
Marapong_11	154.08	153.81	0.28	0.135	48.21	0.5783	0.078	0.4217	0.057
Marapong_13	154.46	154.29	0.17	0.112	65.88	0.4664	0.052	0.5336	0.06
Marapong_14	153.05	152.41	1.62	0.161	9.94	0.5757	0.093	0.4243	0.068
Marapong_15	153.21	152.72	0.49	0.130	26.53	0.5113	0.066	0.4887	0.064
Marapong_17	153.68	152.38	1.3	0.114	8.77	0.5331	0.061	0.4669	0.053
Marapong_18	152	150.1	1.9	0.127	6.68	0.6104	0.078	0.3896	0.049
Marapong_19	152.64	151.87	0.77	0.190	24.68	0.4945	0.094	0.5055	0.096
Marapong_20	152.3	151.46	0.84	0.135	16.07	0.6711	0.091	0.3289	0.044
Marapong_21	153.43	152.33	1.1	0.143	13	0.3882	0.056	0.6118	0.087
Marapong_22	152.53	150.72	1.81	0.195	10.77	0.5337	0.104	0.4663	0.091
Marapong_23	154.65	153.62	1.03	0.112	10.87	0.4658	0.052	0.5342	0.06

Figure 6.4 shows the amount CO_2 collected as a function of the combusted CO_2 mass; the linear behavior suggests a good reproducibility of the combustion. Figure 6.5 shows Fraction Modern Carbon as function of combusted CO_2 with the inclusion of the sampler volume.

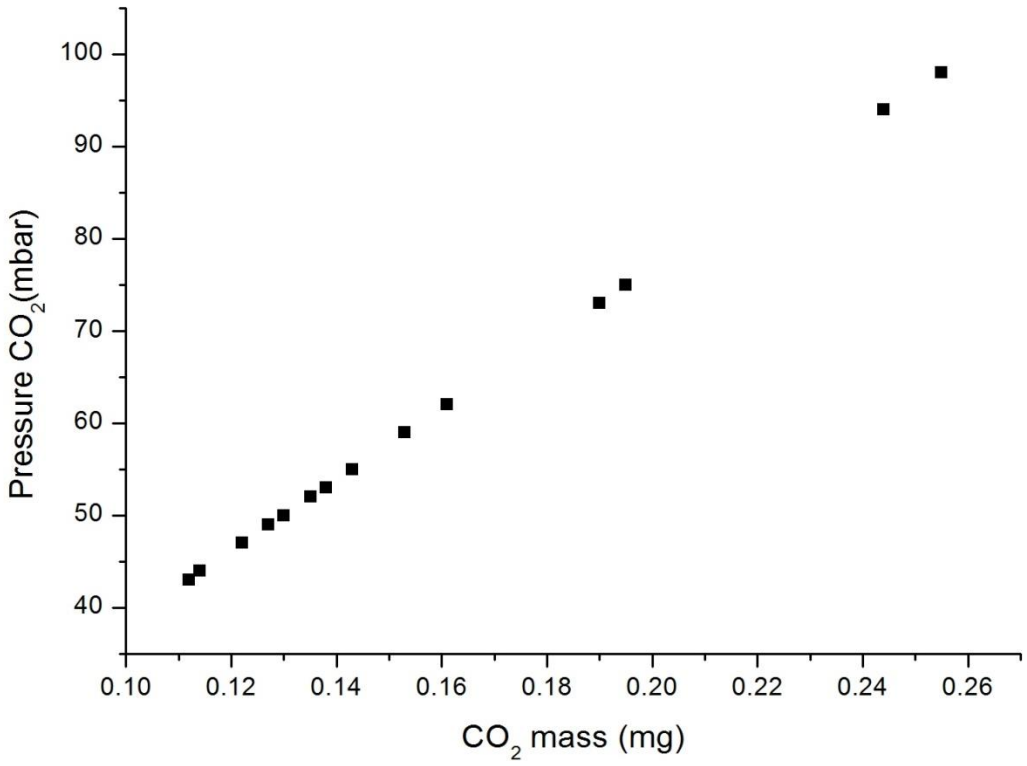

Figure 6.4: CO_2 collected (pressure measured in the graphitization reactor) as a function of the combusted CO_2 mass in aerosol samples collected at Lephalale.

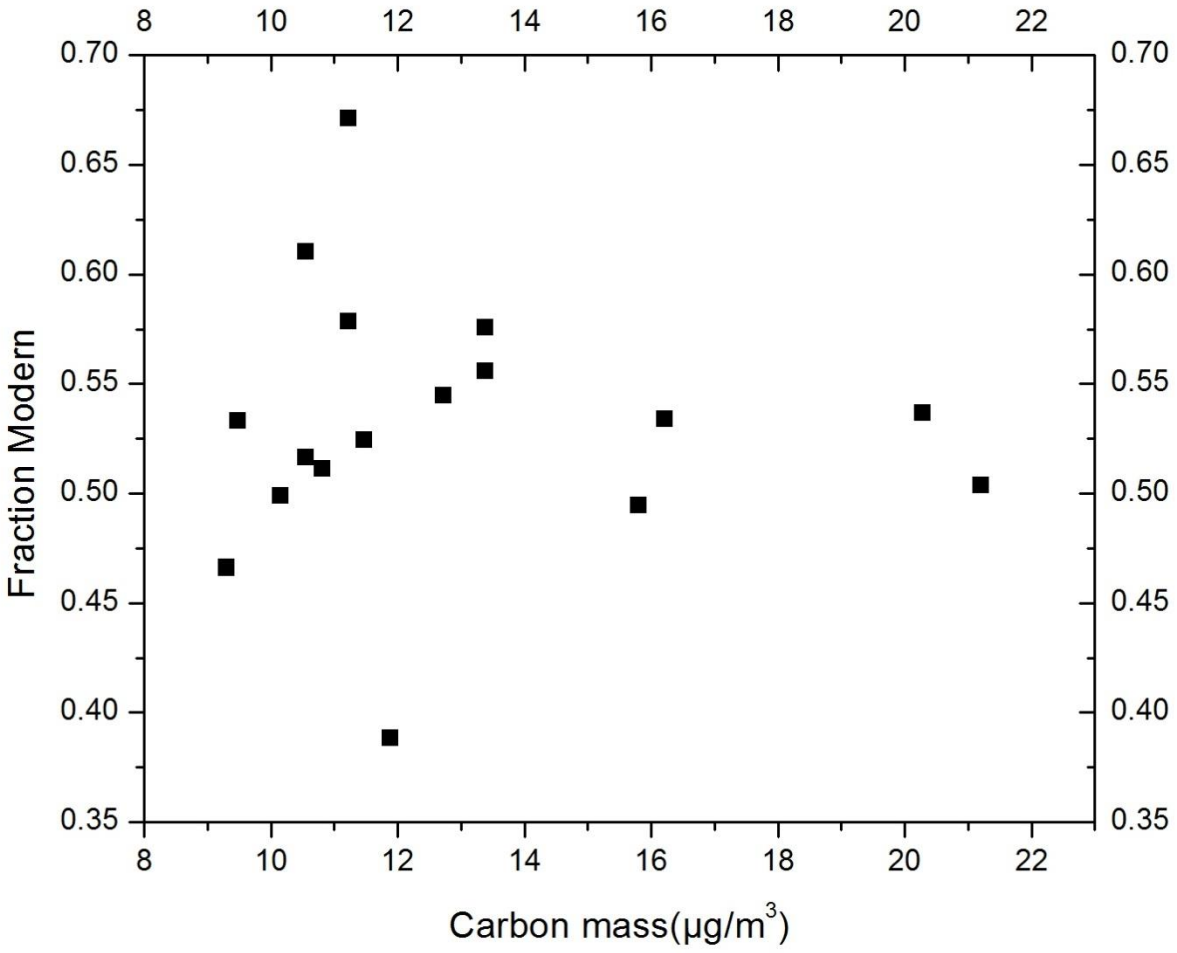

Figure 6.5: Fraction Modern Carbon vs CO_2 mass of the samples collected at Lephalale.

Figure 6.6 shows the contemporary and fossil carbon as function of measured CO_2. There is no correlation between fraction of modern carbon and carbon mass, and the highest fraction of modern carbon is not the highest measured CO_2 carbon mass in $\mu g/m^3$of air.

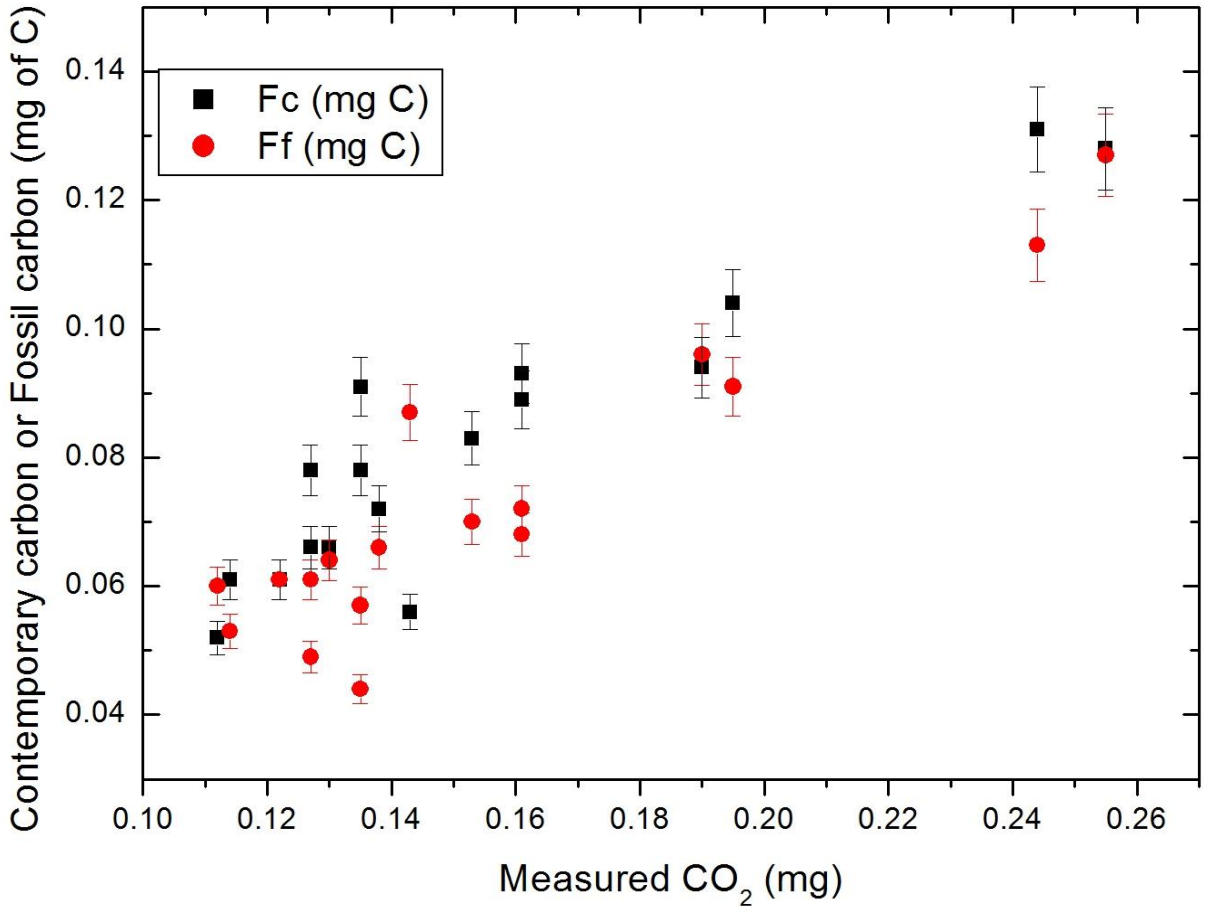

Figure 6.6: Contemporary carbon and fossil carbon vs measured carbon mass for aerosols collected at Lephalale site.

6.2 Proton Induced X-ray Emission (PIXE) Analysis

6.2.1 *Basic principles of the PIXE technique*

Among a range of analytical techniques applied to the characterization of thin aerosol samples, PIXE holds an outstanding position because of its multi-elemental simultaneous analysis ability, high sensitivity, and high throughput that allows the analysis of several particulate samples in short times. In PIXE our sample to be analyzed were set up as targets for

a beam of accelerated protons and, therefore, did not require major sample preparation processes.

The PIXE technique makes use of protons accelerated to energies typically in the 2 to 4 MeV range which are directed onto a target (here, the aerosol sample under analysis) where they interact with atoms in the target. The incoming protons induce ionization of the target atoms where upon electrons from the inner shells can be ejected, leaving a vacancy in that particular shell. The vacancy is filled by an outer electron, as shown on the top of Fig. 6.7. This electronic transition from the outer shell to the unfilled inner shell is accompanied by the emission of an X-ray to be emitted as shown on the bottom of Fig. 6.7. The energy of this X-ray is equal to the difference in energy between the electronic energy states involved in the transition. As atoms of different elements are characterized by unique electronic energy states, the emitted X-ray originating from electron transitions between these states carry a unique signature of the element of the particular atom from which they were emitted. Unfortunately, the technique is unable to detect elements lighter than aluminum (Al) ($Z \leq 13$), which can be major constituents of particulate matter in the atmosphere. This is due to the small energy of these X-rays which makes them vulnerable to absorption by the sample itself. In most atmospheric aerosols thin targets are used because the X-ray production cross-section is constant through the targets and hence X-ray absorption inside the sample is negligible.

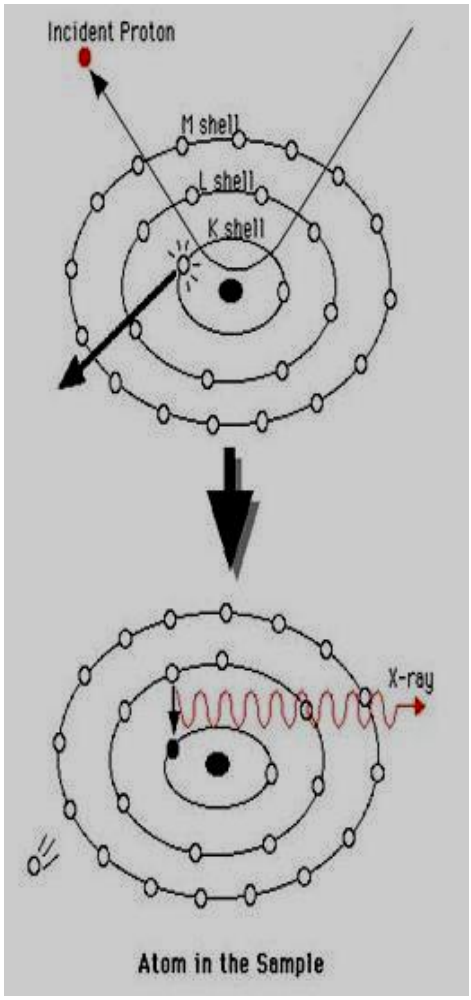

Figure 6.7: Schematic diagram of PIXE. The top diagram shows an incident proton ejecting an inner shell electron from the specimen atom and the bottom diagram shows an outer shell electron filling the resulting inner shell vacancy and emitting an X-ray.

The number of X-rays from the same transition j of an element Z, detected during a measurement is (Johansson and Campbell, 1988):

$$Y_{0X_j}(Z) = \sigma_X(Z, E_0)\alpha_z . \frac{\Omega}{4\pi} . \varepsilon_{det} . \frac{Q}{e} . \frac{N_{AV} . (\rho t)_z}{A} \qquad (6.7)$$

where:

α_z is the fraction of transmitted X-rays from the target to the detector sensitive area

Ω and ε_{det} are the solid angle covered by the detector and its intrinsic efficiency

$(\rho t)_z$ is the mean areal density of the element Z in the surface impinged by the beam

N_{AV} is the Avogadro number

A is the atomic mass of the element Z

Q is the integrated beam charge and

E is the unit charge of the particle

$\sigma_X(Z, E_0)$. is the cross section (probability) of producing an X-Ray from an atom-Z interacting with a proton of energy E_0.

The equation can be rearranged as (Johansson and Campbell, 1988):

$$Y_{0X_j}(Z) = \eta Q(\rho t)_z \tag{6.8}$$

By defining the efficiency factor η for a given X-ray, beam energy, detector and geometry:

$$\eta = \eta_X(Z) = \sigma_{X_j}(Z, E_0).\frac{\Omega}{4\pi}.\varepsilon_{det}.\frac{N_{AV}}{A.e} \tag{6.9}$$

If η is known, the areal density $(\rho t)_z$ of a given element can be obtained by measuring the corresponding X-ray yield on the detector and the integrated beam charge on the target. The efficiency factor $\eta(Z)$ is generally obtained experimentally. This is done by bombarding a series of thin standards containing known quantities $(\rho t)_z$ of the various elements, and measuring the corresponding X-ray yields. Such calibrations using known standards must be performed exactly in the same geometry and all other conditions as those on the samples. The subscript zero, where it appears, serves to remind us that the specimen is so thin that the proton energy is essentially constant within the target material.

By fitting the X-Ray spectra of the unknown samples using the GUPIXWIN software package from Guelph PIXE Group (Guelph, 2013) and modeling the background noise as well

as incorporating the established $\eta(Z)$ value from measured standards, one can calculate the quantity or concentration of a trace element in the unknown sample.

Figure 6.8 shows the schematic diagram of the 6 MV EN Tandem Van de Graaff accelerator at iThemba LABS. The 2.2 MeV proton beam used was directed into the nuclear microprobe facility where it was focused down to a microbeam and scanned over the aerosol sample. The beam spot on the target was about 5 x 8 µm, and the beam was scanned over the sample to avoid damage to filters and reduce elemental losses. The acquisition time was 600 s for each Micromatter thin standards and 1800 s for each sample.

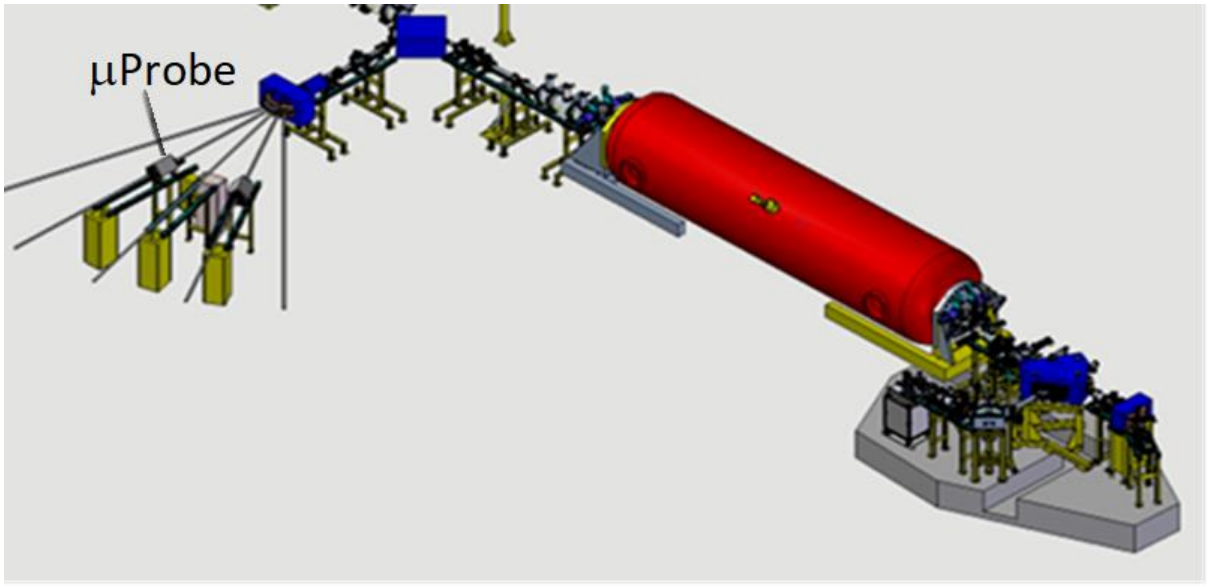

Figure 6.8: Nuclear Microprobe beamline layout of 6 MV EN Tandem van de Graaf accelerator of iThemba LABS.

6.2.2 *Application on aerosol samples*

Thin filters are used to collect particles on their surface by pumping atmospheric air through the filters. Nucleopore or Millipore filters are suitable and are widely employed with

different pore sizes and, hence can allow the separation aerosol particles into different size fractions. In this PIXE study, Polytetrafluorothylene (PTFE) filters were used to collect aerosol matter. They are well known for their chemical resistance, thermal stability and hydrophobicity (Wikol et al., 2007). PTFE is a simple polymer composed of only two elements, carbon and fluorine. It has a long, straight carbon backbone to which the fluorine atoms are bonded.

In most of the cases, the aerosol deposit consists of very few layers of particles with aero-diameter of less than 10 (D_{ae} < 10 μm). Particulate matter of specific size, in this study less than 10 μm, was selected through the use of PM_{10} porous filters.

6.3 *PIXE* analysis in the Lephalale district

6.3.1 *Sampling collections*

Sample collection was perform over a 6 days period of many 12 hrs intervals with day (09h00-21h00) and night (21h00-09h00) sampling times. PTFE filters were used with diameter of 46.2 mm and pore size of 2 μm as collection substrates to be used in Partisol-plus sampling. After aerosols samples are deposited on the PTFE filter, the samples were removed and placed in a membrane filter holder until the PIXE measurements took place on the EN Tandem accelerator at iThemba LABS.

The particulate matter mass on each filter was obtained by comparing the mass of the filters before and after the atmospheric sampling; the masses were determined using, an analytical electronic microbalance (with sensitivity ± 0.1 μg) with the masses being determined only after a storage period (24 h) in a temperature and humidity controlled room (20°C, 50% relative humidity). The masses of particulate matter on the filters during the sampling campaign ranged from 0.53 to 15.99 g between 11 April to 09 May 2011 as shown in Table 6.3.

Table 6.3: Gravimetric mass, the mass of each sample were measured using the precise microbalance before sampling and after sampling for Lephalale.

Sample ID	Mass(g) before	Date	Time	Mass(g) after	Mass diff
PTFE2	0.151433	11 April	21H00-09H00	0.151791	0.000358
PTFE10	0.149497	15 April	21H00-09H00	0.149924	0.000427
PTFE11	0.148931	16 April	09H00-21H00	0.149349	0.000418
PTFE21	0.151179	22 April	21H00-09H00	0.151816	0.000637
PTFE35	0.150406	1 May	21H00-09H00	0.15043	0.00024
PTFE36	0.148732	4 May	09H00-21H00	0.149329	0.00597

6.3.2 *PIXE Analysis and Results*

PIXE measurements were performed using the 6 MV EN Tandem accelerator of iThemba LABS to accelerate protons to an energy of 2.28 MeV. The beam current on target was of the order of 2 nA. The emitted characteristics X-rays traversed a 50μm Al absorber before they were detected by lithium drifted silicon (Si(Li)) detector with an energy resolution of 140 eV at 5.9 keV. The detector was placed at 45° angle relative to the beam direction. The detector was calibrated using several thin Micromatter standards foils; each composed of about 17 μg/cm^2 of single elements or mixed elements (molecular) covering an X-ray energy range from Si (1.74 keV) up to Pb (74.97 keV). A typical PIXE spectrum is shown in Fig. 6.9.

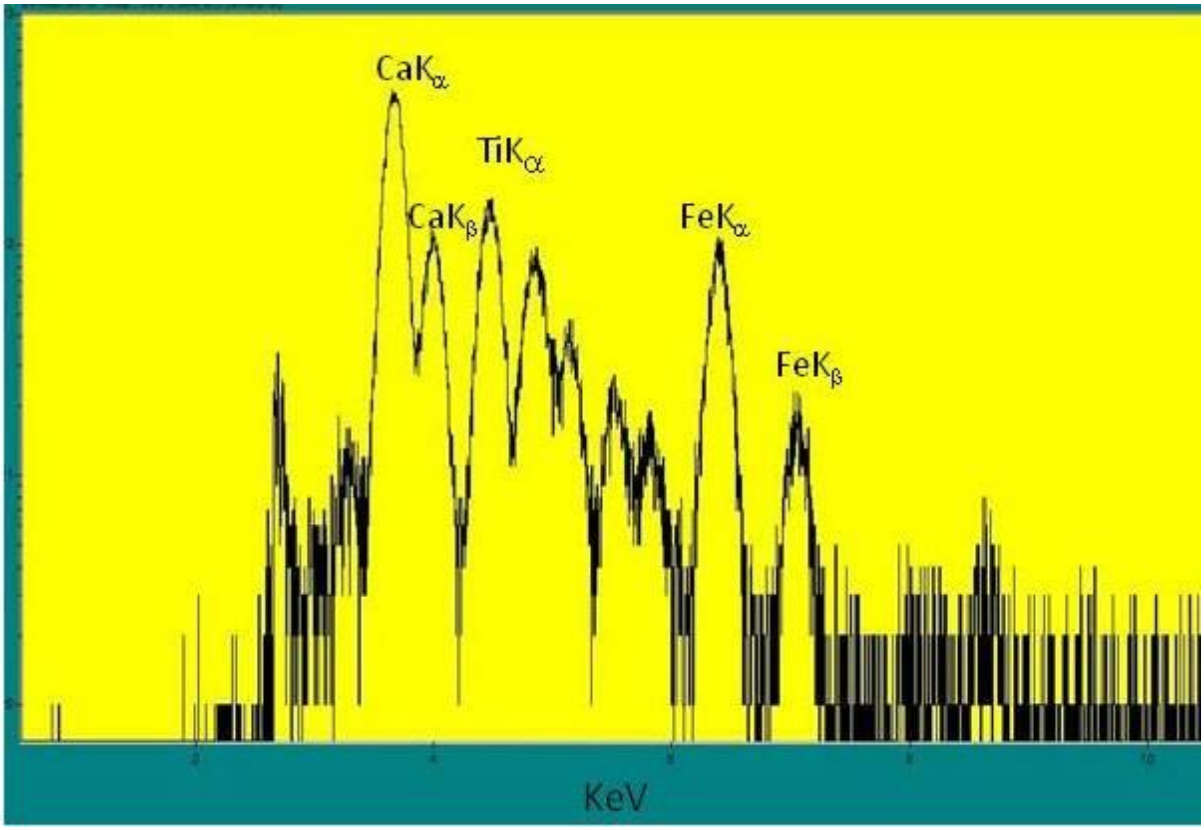

Figure 6.9: Typical PIXE aerosol spectrum from the Lephalale area.

The acquired PIXE spectra were analyzed using the GUPIXWIN code in the thin target approximation mode software in order to determine the elemental contents and concentrations of the sample. The program uses a non-linear least squares fitting approach for fitting PIXE spectra. PIXE measurements determined the elemental composition of the particulate matter in terms of six elements, namely, K, Ca, T, Mn, Fe, and Zn. Table 6.3 shows the gravimetric analysis of the PTFE filters.

Since the sampling is performed in terms of air volume (1 m^3/h or 1.21 kg/h) through the Partisol-plus sampler, the elemental concentrations are presented in µg/m^3 taking the following into account:

1. the air flow through the sample
2. the time of exposure

3. the diameter of the filter.

The exposed portion of the 46.2 mm PTFE filter is 37.8 mm in diameter corresponding to an area of A = 3.14159 (37.8 mm/2 x (1 cm/10 mm))^2 = 11.28 cm^2. The flow rate of the Partisol-plus sampler is 1 m^3/h (16.7 l/min) and given the density of air at 20°C and 1 atmosphere pressure being 1.21 kg/m^3, the total mass collected onto each filter over 12 hours is:

$$m = \rho V \tag{6.10}$$

$$= 1.21 \text{ kg/m}^3 \text{ x } 12.024 \text{ m}^3 = 14.52 \text{ kg}$$

The change in mass, Δm, of the filter before and after exposure represents the concentrated matter collected during sampling.

$$\text{mass concentration} = \Delta m/\text{volume} \tag{6.11}$$

$$= \Delta m/12.024 \text{ m}^3$$

Concentrations as calculated by GUPIXWIN are presented in terms of areal densities (ng/cm^2). The concentrations for every element in each sample as a percentage with respect to the Δm over the area of the sample are:

$$\text{Percentage} = \frac{Concentration}{\frac{\Delta m}{cm^2}} \tag{6.12}$$

Therefore the concentration in μg/m^3, given that 1 percent= 10,000 ppm is given as:

$$\mu g / m^3 = \frac{ppm \times MW}{0.02445} \tag{6.13}$$

where *ppm* is part per million and *MW* is molecular weight of element.

The results after the GUPIXWIN analysis of the spectra and after converting to μg/m^3 are summarized in Table 6.4 expressed as average and median values over the entire range of samples measured.

Table 6.4: Descriptive statistics of the concentrations of 6 elements as determined by PIXE over 6 samples from the Lephalale sampling site.

Element	Mean µg/m^3	Median µg/m^3	STD µg/m^3
K	0.685	1.187	0.238
Ca	15.99	17.523	12.182
Ti	7.442	6.932	6.727
Mn	0.534	0.739	0.237
Fe	12.478	8.461	10.656
Zn	0.757	0.702	0.808

The median elemental composition of particulate matter from Lephalale is presented in Fig. 6.10. It shows high concentration on Ca and Fe, lower concentrations on K, Mn and Zn.

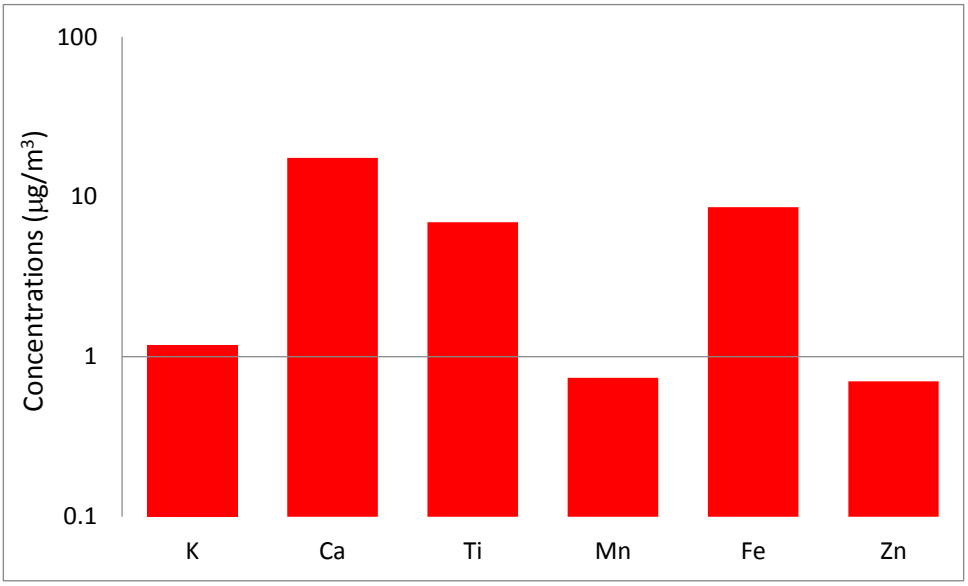

Figure 6.10: Median composition of particulate matter elements deduced by PIXE analysis at Lephalale.

6.3.3 Enrichment factor analysis

In order to assess the origins of the different identified pollutants as measured in air the results are analyzed using the concept of Enrichment Factor (EF) (Hobbs, 2000) which compares the relative concentration of an element accumulated in air to that in a source e.g. soil. EF values were calculated (Hobbs, 2000) for the PM_{10} samples using the equation:

$$EF = ([X]air/[Ref]air)/([X]source/[Ref]source, \quad (6.14)$$

where [X] is the concentration of the element of interest and [Ref] is the concentrations of reference element for the particular source of interest (Hobbs, 2000). EF values near unity for a certain reference element [X] suggest that the source of interest is the primary source of element [X] and that it has not been altered by emissions from other sources. An EF much less than 1, or much higher than 1, indicates the presence of sources other than the source of interest (Senaratne and Shooter, 2004). Table 6.5 shows the average of the crustal elements that were used in the study.

Table 6.5: The average of the elements in crustal rocks (Mason, 1982).

Atomic number	Element	Crustal average (ppm)	Crustal average (µg/m3)
19	K	25900	41
20	Ca	36300	59.51
22	Ti	4400	8.62
25	Mn	950	2.1
26	Fe	50000	114.21
30	Zn	70	0.19

Table 6.6 shows the enrichment factor values for the particulate matter sampled at the Lephalale site. The EF's with respect to Ca, Ti and Mn were calculated relative to soil dust by using Fe as a reference trace element. Their EF values were found to be less than 10, suggesting that they are present in the aerosol in crustal proportions which implies that they are non-

enriched elements (NEE) relative to soil dust. The EF value of K with 0.153 indicates that it is depleted with respect to Fe. The EF value of Zn is highly enriched element with respect to Fe, indicating an anomalously enriched element (AEE). Figure 6.11 summarizes the estimated enrichment factors with respect to Fe as reference element in terms of soil dust for the Lephalale site.

Table 6.6: Enrichment factors for particulate matter analyzed with PIXE (Lephalale).

Elements	**Fe (Soil)**
K	0.153
Ca	2.459
Ti	7.947
Mn	2.389
Fe	1
Zn	30.5

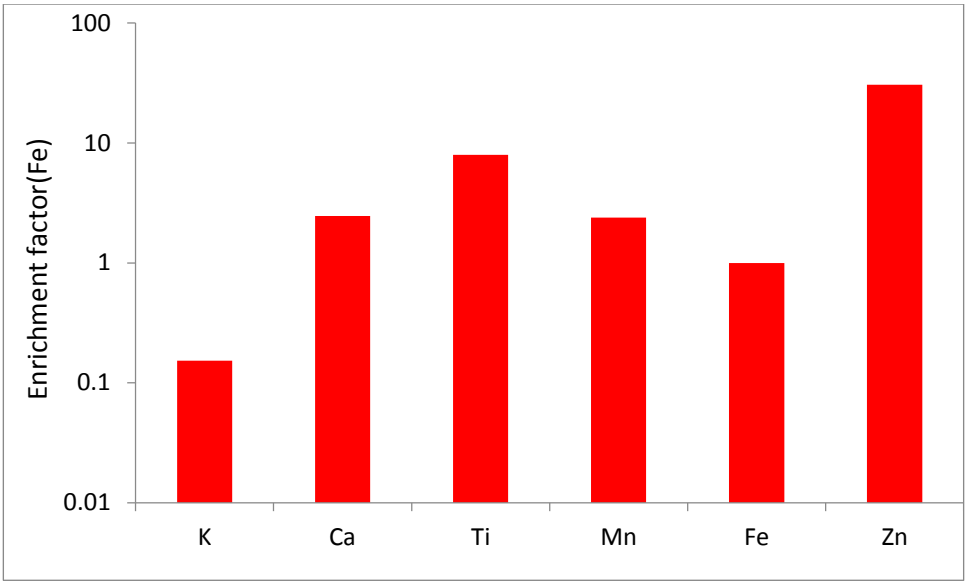

Figure 6.11: Enrichment factor with respect to Fe as soil reference element.

6.3.4 *Source Profiles by Unique ratios (SPUR)*

The identification of PM sources is necessary to develop air quality improvement strategies in order to be able to control and reduce ambient PM concentrations through targeted actions. Many tools have been used for identification and quantification of PM sources to address the issue. Receptor models have been applied in many studies and in many regions around the world and have shown the ability to identify accurately the potential emission sources at a receptor site (Watson et al., 2001; Chow et al., 1992).

Most of the models are based on the hypothesis that mass conversation as well as mass analysis can be used to apportion sources of ambient PM in the atmosphere. In this study, Source Profiles by Unique Ratios (SPUR) technique is being used. The SPUR is a combination of event identification using unique elemental ratios in sources and correction for background events by identifying events of differing time constrains in the time domain (Annegarn et al., 1992). This is similar to the technique used for source apportionment by Absolute Principal

Component Analysis (Maenhaut and Cafmeyer, 1987). By comparing the detected elements with time and size fraction it is possible to separate the contributing sources from stand-alone key elemental indicators, for example Fe for soil dust.

The impact of a source allows one to determine unique ratios between elements for given sources, or alternatively, known ratios of each element to known elements for that source are utilized to extract the contribution of that source from the detected inorganic mass. This type of source apportionment requires a good knowledge of the local and regional meteorology as well as the possible contributing sources. SPUR is based on receptor modelling principles which have been used extensively for identifying contributing sources to receptor site samples (Gordon, 1980; Artaxo, et al., 1988; Rheingrover et al., 1988).

The source apportionments of aerosols study at Lephalale are presented. Elemental concentrations will be used to apportion the aerosols source category of soil dust The elemental concentrations are taken from Table 6.5 for Lephalale and Table 6.6 is used to obtain the ratio to Fe for crustal average

The ratios of elemental concentrations in standard crustal material with respect to Fe, is shown in Table 6.7.

Table 6.7: Ratios of elemental concentrations in standard crustal material with respect to Fe.

Elements	Ratio to Fe
K	0.518
Ca	0.726
Ti	0.088
Mn	0.019
Fe	
Zn	0.0014

Soil dust

Soil has previously been identified as a significant component of South African aerosol in many studies (Piketh, 1999). In order to obtain a reliable estimate of the soil mass associated with major crustal components associated with soil fingerprints for the Lephalale site, the five elements, K, Ca, Ti, Mn and Zn were used. The source profile derived from atmospheric aerosol samples is used to apportion appropriate to soil dust. The total soil component is made of the following equation:

$$[Soil]_i = [K]_i + [Ca]_i + [Ti]_i + [Mn]_i + [Zn]_i . \quad (6.15)$$

The equation is broken-down into individual concentrations of elements as follows:

$$[K]_{res1} = [K]_i - [K/Fe]_{soil} \times [Fe]_i \quad (6.16)$$

$$[Ca]_{res1} = [Ca]_i - [Ca/Fe]_{soil} \times [Fe]_i \quad (6.17)$$

$$[Ti]_{res1} = [Ti]_i - [Ti/Fe]_{soil} \times [Fe]_i \quad (6.18)$$

$$[Mn]_{res1} = [Mn]_i - [Mn/Fe]_{soil} \times [Fe]_i \quad (6.19)$$

$$[Zn]_{res1} = [Zn]_i - [Zn/Fe]_{soil} \times [Fe]_i \quad (6.20)$$

Contribution to the detected elemental mass by PIXE has been calculated for soil:

$$[Soil]_{detected} = [Fe]_i + \Sigma [Fe]_i \times \{[K/Fe] + [Ca/Fe] + [Ti/Fe] + [Mn/Fe] + [Zn/Fe]\} \quad (6.21)$$

$$= 29.353.$$

Table 6.8 shows the residual of the detected element with respect to soil dust.

Table 6.8: Elemental concentrations for soil dust source calculated from source apportionment by unique ratio.

	Soil	Residual
K	6.464	-5.779
Ca	9.059	6.936
Ti	1.098	6.344
Mn	0.237	0.297
Zn	0.017	0.74

So that the percentage contribution for each source has been calculated from Eq. (6.22) for soil dust with respect to each source. The results are being presented on Table 6.9.

$$[\text{Soil}]_{\text{detected}} / [\text{Total}_{\text{elements}}] \text{ x } 100\% \quad (6.22)$$

Table 6.9: Source apportionment from filter samples at Lephalale.

Source	Soil	Residual
%	78.54	21.42

The source apportionment reveals that soil dust has 78.54% of the detected source at Lephalale. The residual source contributes 21.42%. This source could be made-up of many sources and it was beyond the scope of this research to try and break this down into all the contributing sources.

6.4 Results and discussion

The $^{14}C/C$ was used to discriminate the carbon concentrations contents between the contemporary and fossil carbon fractions of the aerosol samples collected at Lephalale from 20 March 2012 to 4 April 2012. The fraction modern carbon was in the range 0.3882 to 0.6711 as shown in Table 6.1. The average contemporary carbon was measured to be approximately 53% at Lephalale. The Lephalale data shows that there is no sample with contemporary carbon

fraction of greater than 1. This shows that there is no underestimation of the contemporary carbon fractions from other sources, which also imply that there is no older wood which have been used in some of the residential wood burning that occurred during the sampling period. The fossil carbon concentration is 47%. The fossil carbon fractions were higher than the contemporary carbon on three days during the sampling period. These correspond to night samples and are namely, Marapong_13, Marapong_21 and Marapong_23 with fossil carbon fraction of 53%, 61% and 53%, respectively. The following samples have 50% of contemporary and fossil carbon; Marapong_4 (day sample), Marapong_8 (day sample) and Marapong_19 (night sample).

The analysis shows that the standard deviation is of the order of 6.108×10^{-2} and the variance of 37.30865. The 95% confidence intervals for the mean is 0.4979 thru 0.5586 for contemporary carbon and 0.4414 thru 0.5021 for fossil carbon accordingly. The analysis of the eighteen aerosols samples also revealed that the measurement uncertainties for the fraction modern correspond to one sigma value of 0.00383 for each filter. The carbon masses range from 0.112 to 0.255 mg. The average mean value for carbon mass is 0.154 mg with standard deviation of 0.042 and a variance of 0.00176.

Table 6.2 summarises the Marapong data analysis with inclusion of fraction of modern carbon, measured CO_2 and contemporary carbon and fossil carbon as derived from carbon mass. The contemporary carbon and fossil carbon are plotted against carbon mass in Fig. 6.5.

The study was undertaken to distinguish between contemporary carbon and fossil carbon. Since the carbon captured on the filter is probably originating from local wood burning, it is implied that this carbon is associated also with contemporary aerosol particulate matter which is of biogenic origin as shown in Fig. 6.5.

The mass concentration measured at Lephalale during the sampling campaign ranged from between 19.96 to 109.65 µg/m^3 between 11 April to 9 May 2011. For the 6 samples that were analyzed, the particulate matter concentrations did not exceed the air quality standards regulation at Lephalale. The recommended daily limit air quality standard by South African legislation is 75 µg/m^3.

Particulate matter particle studies at the Lephalale sampling site revealed the presence of K, Ca, Ti, Mn, Fe, and Zn, leading to characterization of soil source of these elements. Calcium (Ca) has highest concentrations with 15.99 µg/m^3 (mean) as from Table 6.4 followed by Iron (Fe) (12.478 µg/m^3).

Source apportionment reveals that soil dust has a 78.54% detected source at Lephalale. The residual contributed with 21.426%.

The enrichment factor of soil with respect to Fe shows that Ca, Ti and Mn have their EF values of less than 10, which are refer as non-enrich elements. The EF value of K with 0.153, indicate that it is depleted with respect to FE. Whereas the EF value of Zn with respect to Fe is highly enriched element with value of 30.5, which is referred to as an anomalously enriched element.

CHAPTER 7
AMS ^{14}C DATING OF ARCHAEOLOGICAL SITES OF KHOI-KHOI PEOPLE

7.1 Application of AMS on archaeology

7.1.1 *Introduction to Kasteelberg B site*

^{14}C dating continues to form the foundation of archaeological chronologies and southern African researches benefit enormously from Pretoria internationally reputed Quaternary Dating Research Unit. The first direct AMS ^{14}C dating of sheep bones in South Africa. Sealy and Yates (1994) redated important sites of Spoegrivier, Kasteelberg, De Kelders, and Byneskranskop in the southern and western Cape regions and in Nambia, and obtained ^{14}C ages that were mostly younger (about 1630-1330 BP) in contradiction to ages extracted (about 1960-1860 BP) in earlier dating of associated materials (Kuzmin, 2009; Sealy and Yates, 1994).

Kasteelberg is a large granite inselberg on Vredenburg Peninsula (south-western Cape, South Africa), 4 km from Atlantic Ocean coast, and 130 km north of Cape Town; Fig. 7.1 shows a map of the sampling site. Its topographic setting, location near the coast, and the surrounding pastures made the site an attractive place for human occupation (Smith, 1992). The archaeological deposit in the main excavation site within a cave, was on average 1.7 m deep as shown Fig. 7.2. The main site on the hill, KBB, is generally considered to have been occupied by KhoiKhoi pastoralists for at least a millennium before the arrival of European settlers in the 17th century (e.g. Klein, 1986; Mitchell, 2002; Smith, 2006). The site was first reported by Jalmar Rudner (1968) in connection with whole pots and enigmatic grooves on the ground into the bedrock surrounding the site.

The Khoisan populations of Southern Africa are conventionally divided into the KhoiKhoi and the San, the main logic of the dichotomy being that the KhoiKhoi were pastoralists at first contact with Europeans, while the San subsisted purely by foraging (Barnard, 1992). It has long been observed that some groups of KhoiKhoi peoples of South-Western Africa acquired pottery, sheep and cattle within quite a short time window (ca. 2000 BP) before attested contact with expanding Bantu-speakers.

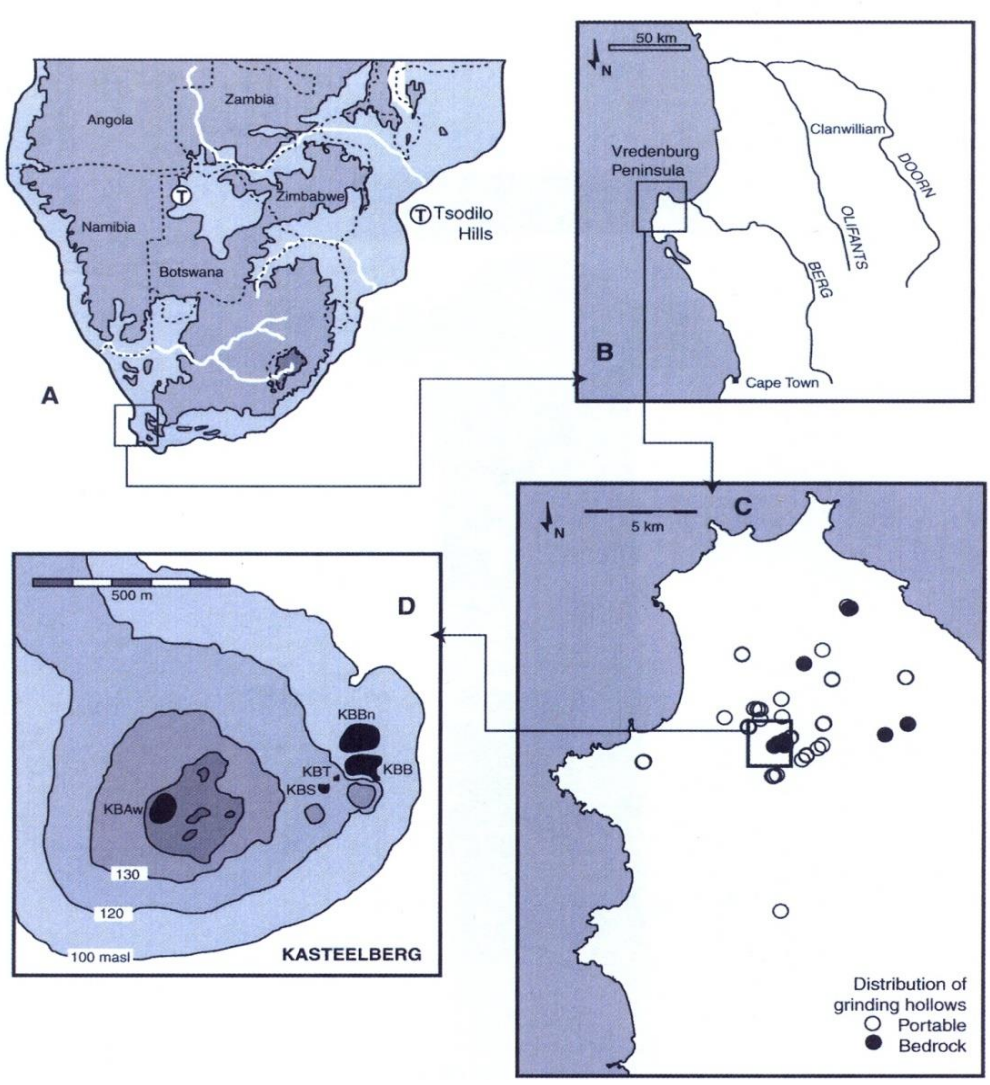

Figure 7.1: Maps of the west coast, Vredenburg Peninsula and Kasteelberg (Sadr and Fauvelle-Aymar, 2006).

The KhoiKhoi were in possession of cattle, sheep, goats and dogs when first encountered by European observers (Boonzaier et al., 1996). Picture shown in Fig. 7.3 depicting a KhoiKhoi kraals. Figure 7.4 shows picture of KhoiKhoi woman milking the cow. Table 7.1 shows selected early dates for Southern African livestock in the archaeological record.

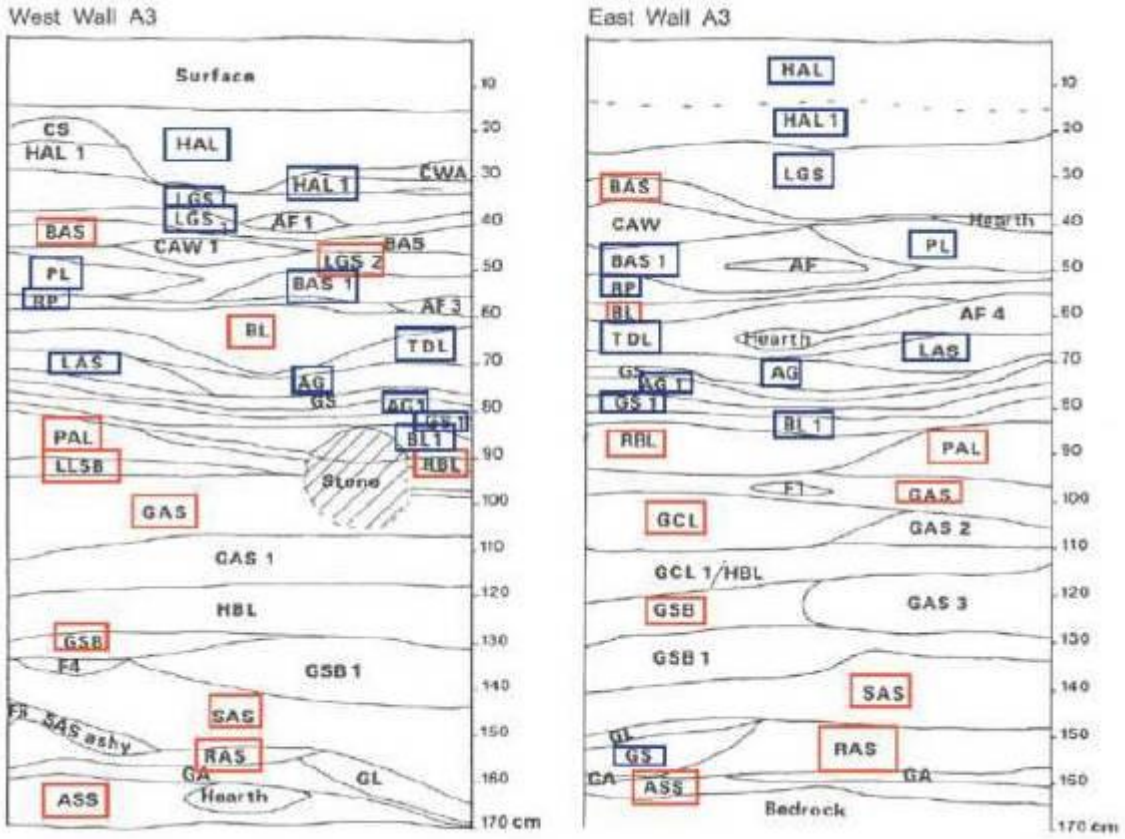

Figure 7.2: KBB west section square A3 and KBB east section square A3 (Smith, 2006). Stratum labels outlined in red indicate contexts of the marine shells samples dated by AMS in this thesis. Blue outlines indicate shell was collected but had not been dated.

The wild ancestors of KhoiKhoi domestic stock never lived closer than 7000 km from the Cape and there is no evidence that the KhoiKhoi or their predecessors ever domesticated any indigenous animal species (Klein, 1986). It is thus very clear that herding and the herding

way of life were introduced from elsewhere. Y-chromosome E3b1f-M293 (Henn et al., 2008) and lactase persistence allele -14010*C (Macholdt et al., 2014) convince geneticists that the KhoiKhoi-speakers are linked, at least through the male lineage (Barbieri et al., 2014), to pastoralists in East Africa; What remains intriguing is whether the earliest livestock in southern Africa arrived in the company of immigrant Khoi-speakers, or whether the Khoi-speakers were later arrivals while the first livestock were traded down the line or infiltrated among southern African San (a.k.a. Bushman) people speaking Kx'a and Tuu (non-Khoi) languages (e.g. Sadr 2015). The revised chronological record at Kasteelberg sheds light on this issue.

KBB is not a single component site (Smith, 2006). Two major and one minor, terminal components were recognized in the ceramic remains, lithics and radiocarbon dates (Sadr and Smith, 1991; Smith, 2006). In the debate about whether immigrant KhoiKhoi speakers introduced the first sheep to the southwestern Cape of South Africa, it has been argued by Sadr (1998) that the earliest component at KBB probably represented locals and that the KhoiKhoi may have introduced the lugged ware which appears around AD 1000 at Kasteelberg site. The argument was based on the analysis of ceramics. Smith has countered the arguments by maintaining the case for an immigrant ancestral of KhoiKhoi population having introduced both pottery and sheep to the Cape some 2000 years ago (Smith, 2006; Smith, 2008).

Table 7.1: Early dates for cattle and sheep of southern African (Blench, 2007).

Species	Location	Site	Calibrated date
Sheep	Namibia	Falls Rockshelter	190 BC-383 AD
Sheep	Botswana	Toteng	190 BC- AD 20
Sheep	South Africa	Blombos	82 AD-215 AD
Sheep	South Africa	Spoegrivier	165 BC- AD 13
Ovicaprines	South Africa	Ma38	200- 300 AD
Cattle	Botswana	Toteng	190 BC-AD 20
Cattle	Botswana	Lotshitshi	>200 AD
Cattle	South Africa	Happy Rest	>300 AD

Sheep are the best documented stock in western and southern Cape archaeological sites (Klein, 1986). The cattle occur much less often and may have been introduced somewhat later (?1600-1500 BP) (Klein, 1986). The occupants of the site engaged in hunting and gathering, which is shown by stock and indigenous animals which are also well presented.

Figure 7.3: A KhoiKhoi kraals as depicted by Peter Kolbe (1719).

At the time of the early European settlement at the Cape, KhoiKhoi herders traded cattle, sheep, tortoises and fish with the settlers, provided them with slaves, and it is noted that these animals constituted part of the KhoiKhoi and San people's diet (Moodie, 1950; Raven-Hart, 1971). It is also mentioned that when the Europeans landed on the western or southern Cape coasts, they bartered metal items, tobacco, alcohol and other goods for the sheep and cattle tended by native herders. Records from the journal of Van Riebeeck indicate that the KhoiKhoi managed grazing with fire and that timing was related to transhumance (Thom, 1952). Deacon also cites ethnographic evidence (Bleek, 1928; Schapera, 1930) that this was a traditional practice. Deacon (1978) suggested that deliberate veld-burning as a grazing and geophytes management tool had an early history, possibly amongst hunter-gatherers as well as herders, and may have been a seasonal practice related to transhumance.

Figure 7.4 A picture of late 17th century of a KhoiKhoi woman milking the cow (Smith and Pheiffer, 1993).

The use of marine resources is clearly documented at Kasteelberg and establishes a clear link to both the lagoon and seashore. Marine shell is present at most of the localities, most notably in pottery. The presence of pottery at many localities reflects occupation by hunter-gatherers, pastoralists, or a combination of both. Fragments of pottery vessels are abundant at localities such as pottery, and stone ring.

There were also differences in subsistence practices associated with the lower and middle occupations at KBB. Although black mussel (*Choromytilis*) dominated the marine shell assemblage of the entire KBB sequence, the lower occupation contains a slightly higher ratio of black mussel shells to limpets than middle KBB (Smith, 2006). Bullia shells dominated Burnapena in lower KBB while in the middle occupation they were equally represented (i*bid*.:

Smith, 2006). Faunal remains show proportionally more sheep and small-medium bovids in lower KBB, and relatively more seal in middle KBB (Smith, 2006).

The material difference between the pre- and post-1000 AD occupations at KBB are distinctive, but what explains the difference? Are two different populations represented; two successive occupations by people of two different cultures, one replacing the other? Or were the lower and middle occupations by the same population at two separate points in time; two phases in the evolution of the same culture separated by a hiatus? A third possible hypothesis, that pure activity differences account for the observed changes, does not merit further consideration in view of the scale of stylistic differences in the pre- and post-1000 AD ceramic assemblages (Sadr and Smith, 1991). Both types of pottery, the spouted ware associated with lower KBB and lugged ware of middle and upper KBB, were primarily used for rendering seal blubber (Patrick et al., 1986; Copley et al., 2004; Stewart, 2005), but in terms of shape, decoration and size they are two different wares.

7.1.2 *Sampling*

Kasteelberg B (KBB) artifacts were excavated during the 1980s by team from the University of Cape Town under direction of Andrew Smith (Sadr and Fauvelle-Aymar, 2006). The samples were collected by Smith from his excavated samples in square A3 as shown in Figure 7.2. Smith selected three whole shells of the limpet *Scutellastra granularis* from each of stratigraphic layer excavated in square A3 at Kasteelberg. These shells were selected to cover the entire sequence of occupation at KBB, with denser sampling around the time of transition from lower to upper occupation at the site. These indicate that the entire KBB sequence is pottery bearing.

KBB site is one of the Late Stone Age open-air shell midden site. Here, 27 square meter (sq m plus ten 1 sqm test pits across the site have been excavated (Sadr and Smith, 1991). KBB

has three main occupation horizons: the first is dated to c. 1300-1100 BP, the second to c. 990-880 BP and the last to c. 190 BP (Balasse et al., 2003) and excavated materials at Kasteelberg date to within the last 2000 years (Sadr and Fauvelle-Aymar, 2006). The interface of the periods is unclear as Sadr (1998) argued that we cannot tell whether the transition was rapid or took over 200 years. With the available evidence of the AMS dating it is possible to determine how quickly the change took place from early KBB to late KBB. Or if the change occurred gradually it could support the idea of an *in situ* cultural transformation thus refuting the idea that migration was responsible for new lugged ceramic types, which appear in the second millennium (Sadr, 1998).

Recently, in order to have a better idea of the occupation and palaeoclimatic sequence (which is not part of this study) at this site and to determine whether an occupation hiatus existed between the first and the second component at KBB, a stratified series of limpet shells were AMS dated. This thesis reports on these dates and discusses their implication for understanding the history of early herding at KBB.

7.1.2 *Measurements and methods*

All AMS analyses described in this thesis were performed at CAMS, which is a state of the art AMS facility operated at LLNL in Livermore, California. The AMS beam line of the LLNL FN Tandem accelerator is equipped, on the low-energy side, with 64 multi-cathode ion source for production of negative ions, magnetic analysis, electrostatic analyzer and deflection magnet and a high voltage (10 MV) FN Tandem Van de Graaf accelerator, on the high-energy side is equipped with magnetic and electrostatic analysis and a gas ionization detector. ^{13}C isotope is measured by offset Faraday cups after the high-energy magnet; ^{14}C ions are counted in an ionization chamber. Measured $^{14}C/^{13}C$ ratios in unknown samples are corrected for

isotopic fractionation and for background events and normalized to NIST oxalic acid I and NIST oxalic acid I.

CAMS/LLNL ^{14}C dates are based on $^{14}C/^{13}C$ atom ratios to obtain the equivalent of specific ^{14}C activities. Date extraction and normalization algorithms, developed by J. Southon (unpublished), are used at CAMS/LLNL which are similar to those developed in the Arizona AMS facility (Donahue et al., 1990). Radiocarbon age data are presented following the conventions of Stuiver and Polach (1977), including using the Libby half-life of 5568 years. Calculations include a background subtraction and inclusion of background error based on ^{14}C-free calcite determined on multiple samples for each wheel of unknowns (Brown and Southon, 1997). To obtain the inherent ^{14}C within the shell is complicated process due to problems associated with comparison to uncorrected ^{14}C. As the ^{14}C content of marine samples is different than in terrestrial samples due to the large carbon reservoir of the oceans the measured ages of marine shells can differ by hundreds of years. To standardize our results and increase the accuracy of our interpretations, all dates were calibrated with Calib 6.1 (Stuiver et al., 2005) and applying a ΔR of 146 ± 85 years correction to compensate for local ocean upwelling (Dewar et al.). Table 7.2 lists the results of the analysis performed at LLNL for all Kasteelberg B samples and the last column on the table shows the calibrated results using "Calib".

Figure. 7.5 shows an example of calibration of a radiocarbon age for a Kasteelberg B sample using the Calib code; the calibrated calendar age is shown on the x-axis and the measured radiocarbon value is represented on the y-axis after having subtracted the ΔR value of 146 ± 85 years. Both x and y ages include 1-sigma and 2-sigma ranges corresponding to the measurement uncertainty probability distribution (Calib, 2014).

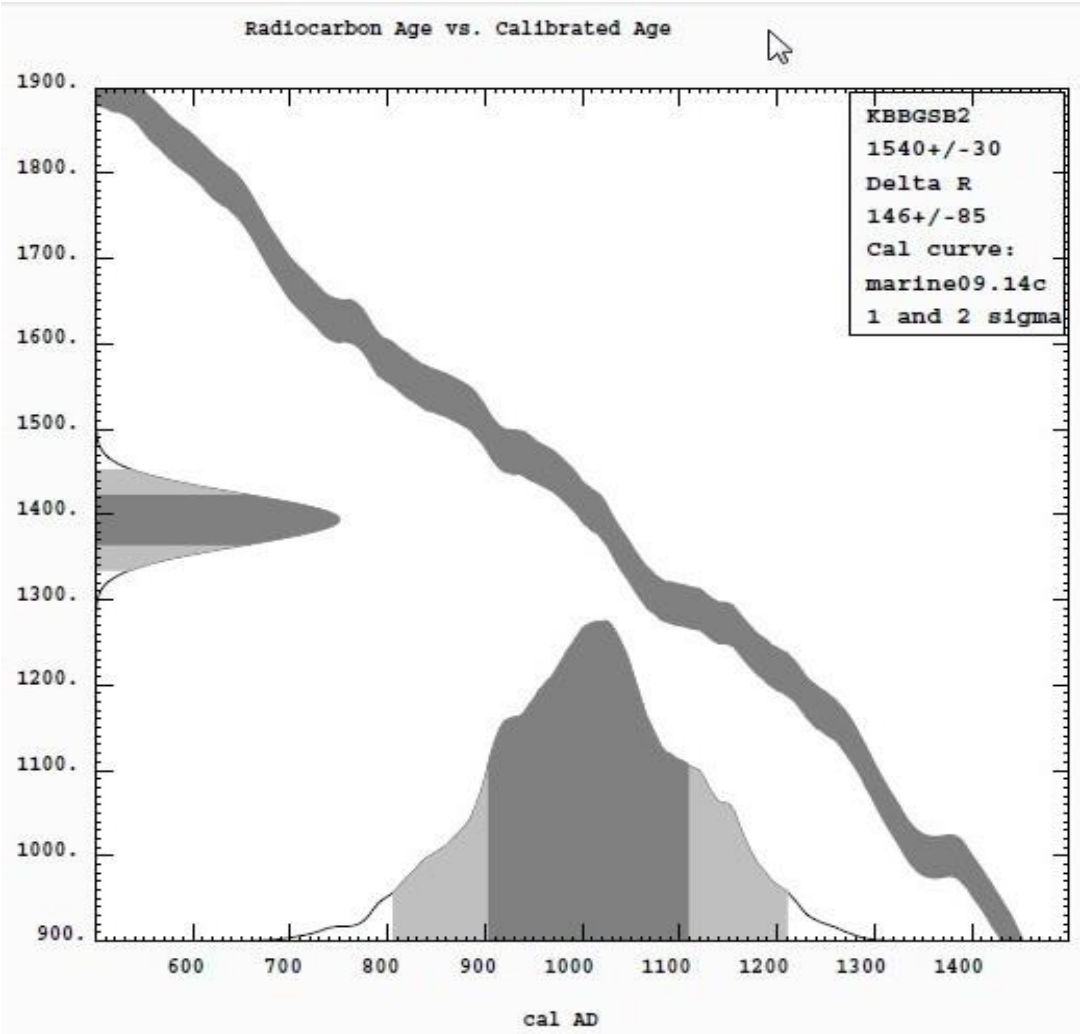

Figure 7.5: An example calibration of a radiocarbon age from a Kasteelberg B sample; the calibrated age is on the x-axis and the measured radiocarbon value is represented on the y-axis with the plot showing 1-sigma and 2-sigma ranges of the measurement uncertainty probability distribution (Calib, 2014).

Table 7.2: Summary of the results for the Kasteelberg B samples analyzed at LLNL, calibration ages are quoted at two sigma uncertainity.

AMS #	Sample Name	Other ID	$\delta^{13}C$	Fraction Modern	±	1-sigma	2-sigma	^{14}C age	±	Cal AD
160481	**KBB GSB1**	N103740	-3	0.8304	0.0030	971-1170	866-1257	1495	30	**1059**
160482	**KBB GSB2**	N103741	-3	0.8254	0.0029	903-1110	805-1212	1540	30	**1007**
160483	**KBB GSB3**	N103742	-3	0.8252	0.0031	898-1108	795-1207	1545	35	**1002**
160484	**KBB LSB1**	N103743	-3	0.8282	0.0030	945-1151	831-1231	1515	30	**1036**
160485	**KBB LSB2**	N103744	-3	0.8360	0.0030	1031-1210	929-1286	1440	30	**1113**
160486	**KBB LSB3**	N103745	-3	0.8305	0.0030	977-1173	875-1261	1490	30	**1064**
160487	**KBBGCL1**	N103746	-3	0.8401	0.0032	1057-1235	974-1312	1400	35	**1147**
160488	**KBBGCL2**	N103747	-3	0.8349	0.0032	1022-1207	914-1280	1450	35	**1104**
160489	**KBB RBL2**	N103750	-3	0.8388	0.0030	1052-1227	969-1304	1410	30	**1139**
160490	**KBB RBL3**	N103751	-3	0.8317	0.0030	986-1182	886-1270	1480	30	**1075**
160491	**KBB GAS1**	N103752	-3	0.8349	0.0030	1022-1205	918-1278	1450	30	**1105**
160492	**KBB GAS2**	N103753	-3	0.8317	0.0030	988-1180	889-1267	1480	30	**1075**
160493	**KBB GAS3**	N103754	-3	0.8253	0.0029	899-1105	797-1204	1545	30	**1002**
160494	**KBB PAL1**	N103755	-3	0.8339	0.0040	1006-1200	902-1279	1460	40	**1095**
160495	**KBB PAL3**	N103756	-3	0.8389	0.0031	1052-1227	969-1304	1410	30	**1139**
160407	**KBB BAS2**	N103668	-3	0.8309	0.0029	977-1173	875-1261	1490	30	**1064**
160408	**KBB PAL2**	N103669	-3	0.8472	0.0030	1129-1299	1034-1356	1330	30	**1209**
160496	**KBB LGS2**	N103677	-3	0.8404	0.0029	1062-1237	984-1311	1395	30	**1152**
160409	**KBB BL3**	N103670	-3	0.8415	0.0030	1072-1247	992-1317	1385	30	**1161**
160410	**KBB SAS3**	N103671	-3	0.8096	0.0028	743-943	677-1028	1695	30	**847**
166588	**KBB ASS2**	N103672	-3	0.8072	0.0031	713-909	660-1018	1720	35	**825**
166589	**KBB SAS2**	N103673	-3	0.8287	0.0029	953-1157	837-1236	1510	30	**1046**
166590	**KBB RAS3**	N103674	-3	0.8208	0.0029	854-1053	759-1168	1585	30	**958**
166591	**KBB RAS2**	N103675	-3	0.8173	0.0029	828-1023	716-1113	1620	30	**920**
166592	**KBB ASS3**	N103676	-3	0.8126	0.0029	784-981	689-1048	1665	30	**875**
160496	**UCI-2**	N103758	-1	0.9431	0.0033			470	30	
160497	**Calcite**	N103757	0	0.0023	0.0001			48860	230	

A graph of the Kasteelberg B sample arranges according to dates, as from 825-1209 AD, is shown Fig. 7.6. The calibrated ^{14}C dates are quoted within 1 and 2 sigma ranges. An age-depth correlation regarding the Kasteelberg B samples is shown in Fig. 7.7. This provides an idea of the strategraphic chronology over the time period studied and the difficulty of simply correlating ages to depth.

Figure 7.8 represents the stratigraphic order of the Kasteelberg B samples using the order of the samples from Fig. 7.2 as they were excavated at the Kasteelberg B site.

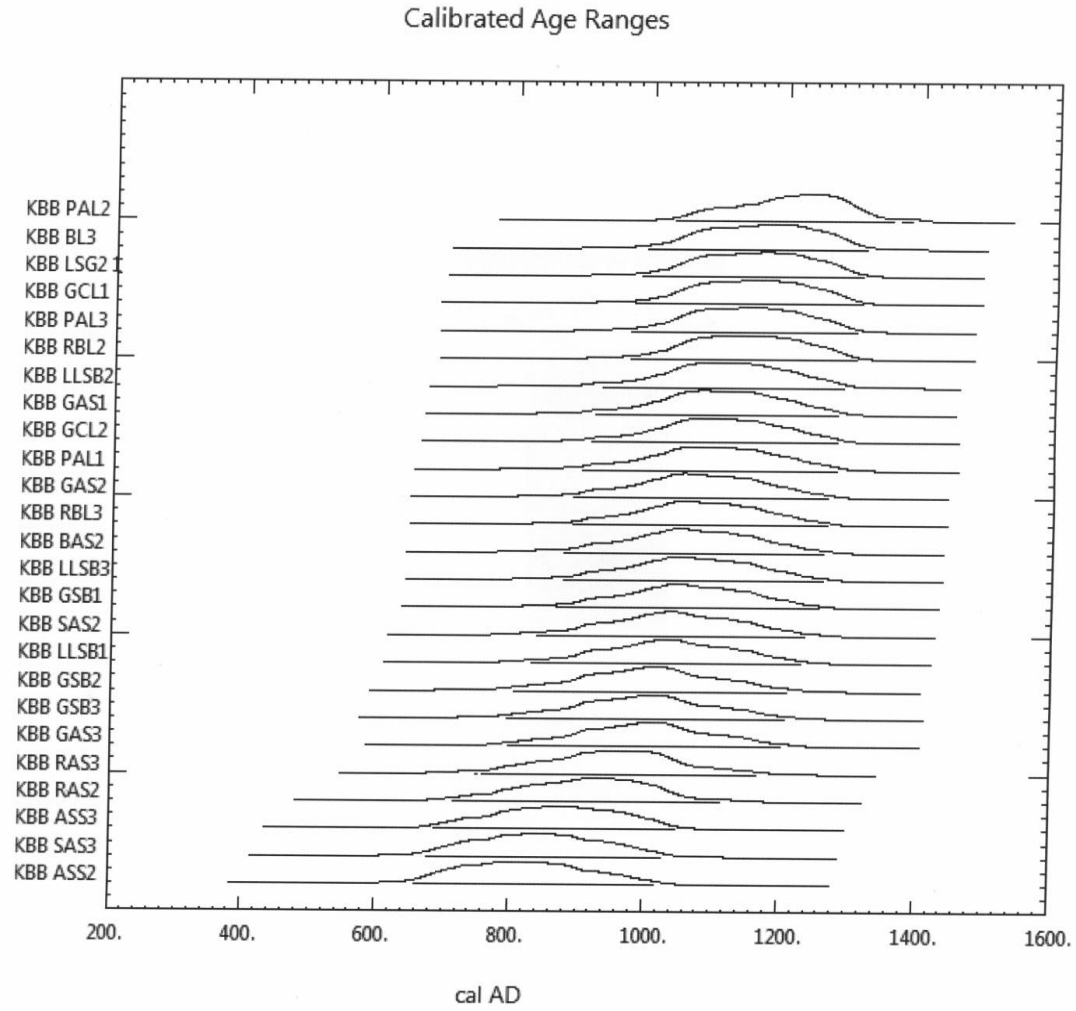

Figure 7.6: Plot of probability distributions for the calendar ages of samples at Kasteelberg B site.

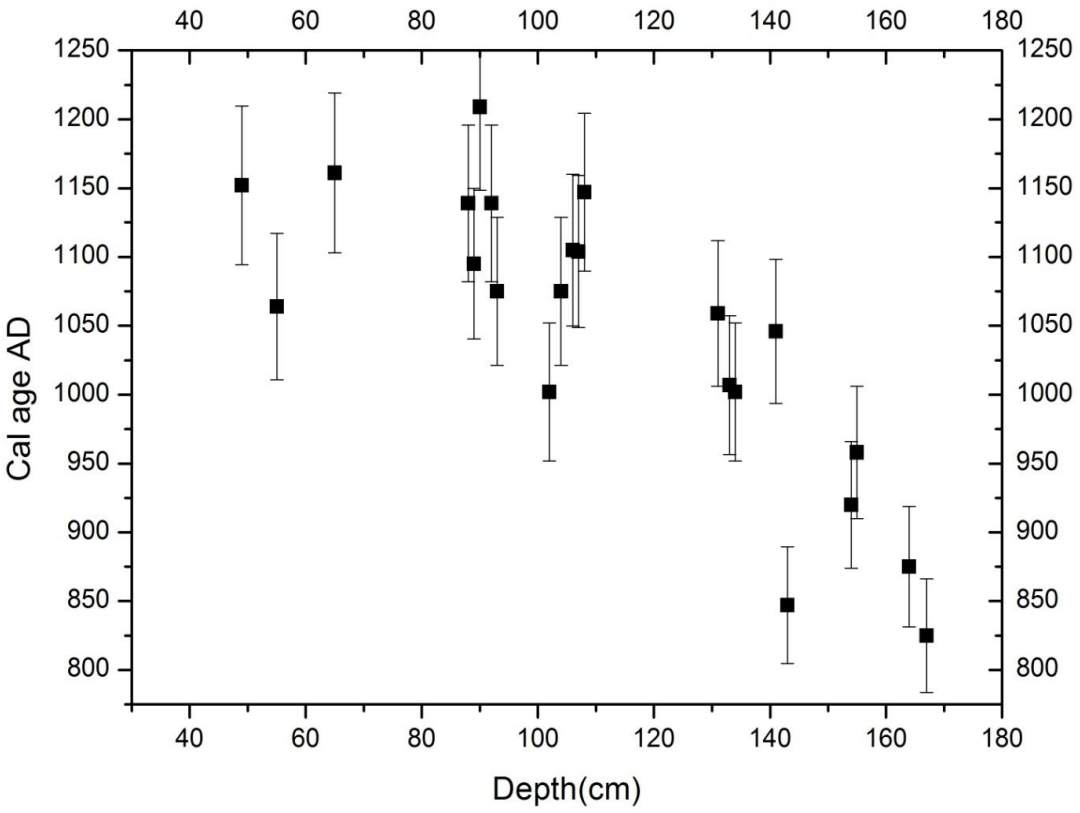

Figure 7.7: Age-depth plots for Kasteelberg B site sampling.

Statistical data analysis was also performed by using the appropriate subroutine in Calib 6.1 (Stuiver et al., 2005) to test for statistically significant age differences between samples from a given depth. The analysis determines the pooled average (weighted mean) of the ^{14}C dates, calculates the test statistics T from the differences between each sample age and pooled average, and compares T with a chi-square distribution for n-1 samples. If T is less than the chi-square value, the dates do not differ statistically (Oswald et al., 2005). The level of acceptable chronological uncertainty depends on the objective of the research; in the present case the analysis is limited to dates with uncertainties less than 200 ^{14}C years.

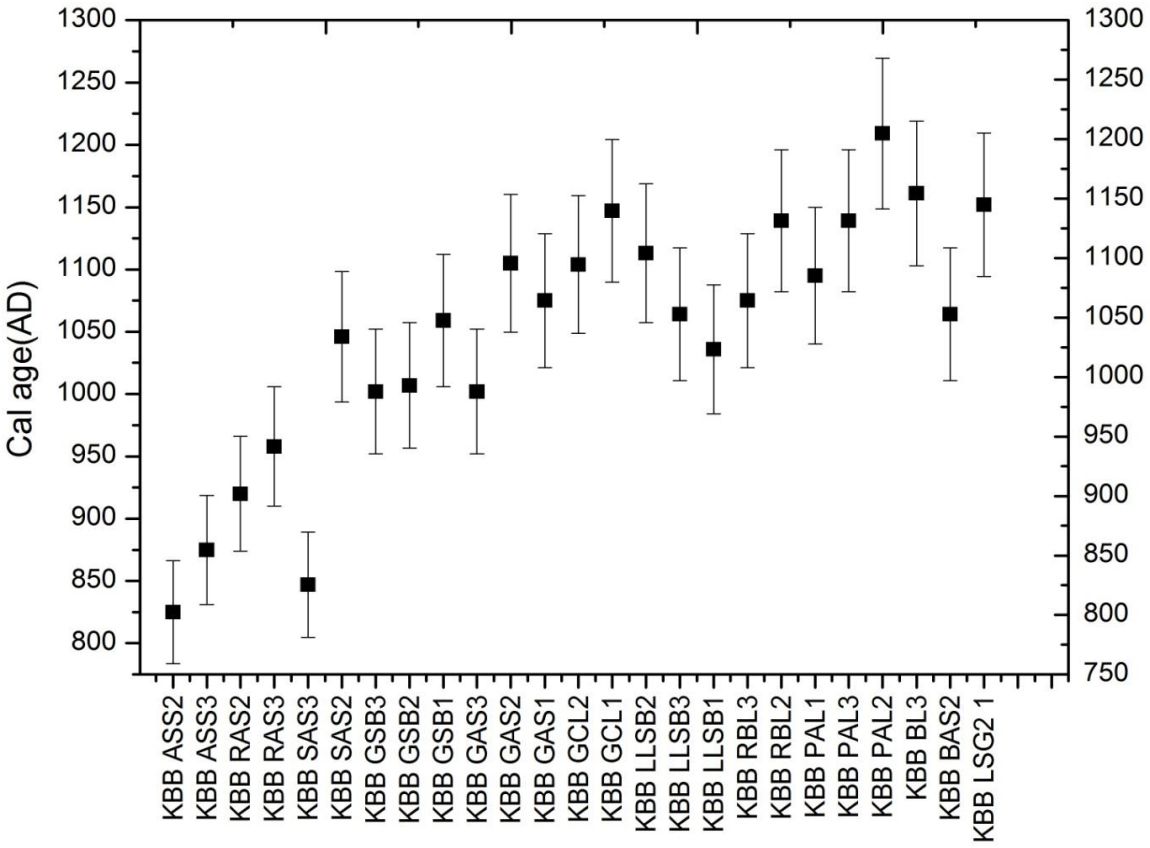

Figure 7.8: Calibrated AMS dates arranged according to samples which correspond to different depths as depicted in Fig. 7.2.

7.2 *Results and discussion*

All dates were converted to calibrated (cal.) ages using Calib 6.1(Stuiver et al., 2005) and applying a ΔR of 146 ± 85 years to compensate for local upwelling (Dewar et al.), assuming $\delta^{13}C$ values of -3 per mil (‰)(Stuiver and Polach, 1977). ^{14}C age of sample is shown in Fig. 7.5, plotted using Calib 6.1 radiocarbon calibration program. As shown in Fig. 7.5, the grey filled curves are statistical (Gaussian) distribution of the statistical distribution of the measured ^{14}C ages. The grey wiggly curve is the marine09 radiocarbon calibration curve from delta R from local ^{14}C data. The filled black curve is the statistical distribution of the calibrated ^{14}C ages obtained using Bayesian analysis. The horizontal lines signify the 1σ (68.2%) and 2σ (95.4%) probability ranges of the dates. Calibrated calendar (cal.) ages are also shown in Fig.

7.5. Each 1σ and 2σ probability distribution corresponds to one or several ranges, out of which the most probable cal AD for each sample was established by using the statistical analysis process coded in the calib software. Calendar ages of samples represent the difference between year of dating and mean value of the most probable date.

Fraction modern (F_M) values and radiocarbon dates of samples from the Kasteelberg B site are listed in Table 7.2. Radiocarbon dates and errors were rounded to the nearest year. The average age of the samples is 1049 years. Radiocarbon dates from Kasteelberg B samples reveal that the dates range from 825-1209 years. The radiocarbon of the oldest sample was 1330 ± 30 years (i.e. KBB PAL2) which corresponds to a most probable date of calibrated age of 1209 years. The radiocarbon of the youngest sample was 1720 ± 35 years which corresponds to a most probable date of calibrated age of 825 years. Radiocarbon dates of KBB GSB3 and KBB GAS3 were 1545 ± 35 years and 1545 ± 30 years respectively, which correspond to calendar age of 1002 years are identical. Radiocarbon date of KBB LSB3 and KBB BAS2 were 1490 ± 30 years and 1490 ± 30 years respectively, which correspond to calendar age of 1064 years are identical. Radiocarbon date of KBB RBL3 and KBB GAS2 were 1480 ± 30 years and 1480 ± 30 years respectively, which correspond to calendar age of 1075 years which are identical. Most radiocarbon dates are between 80-120 cm depth and have between 1002-1209 years. The positions of these samples at KBB site on Fig. 7.2 are very close to one another, which suggest that the dates from same depth provides the dates that are very close. Radiocarbon dates of KBB GCL2 and KBB GAS1 with dates of 1450 ± 35 years and 1450 ± 30 years respectively with calendar age of 1104 years and 1105 years, show that they belong to same depth from excavation. The age gap between the oldest samples and younger sample is 362 years. The young samples are between 150-170 cm depth of the excavation area as shown in Fig. 7.2 of age depth plot, these samples are KBB SAS3, KBB ASS2, KBB RAS3,

KBB RAS2, and KBB ASS3 as shown in Fig. 7.7 and their calibration age is between 825-958 years.

Radiocarbon dates of the samples that have been analyzed reveal no large differences within the 20-140 cm excavation depth. The plot of probability distributions shows that the majority of the samples are of the same phase or close to each other in terms of the year, except for the samples that are between the 150-170 cm depth. The time span of the samples from 150-170 cm depth is about 221 years. The probability plot on Fig. 7.6 shows that the single sample of KBB PAL2 is an outliner which is not part of the upper and lower group, but an independent group.

By using Calib, some statistical analysis was performed and obtained the mean pooled radiocarbon age of 1500.151 years with square root of variance of pooled mean age of 18.1124 years over 25 samples. The test T is 28.21875, chi-square $X_i 2(0.05)$ of 36.4 and 24 degrees of freedom. Since T value of 28.21875 is less than the chi square value of 36.4, this implies that the dates do not differ statistically (Ward and Wilson, 1978). As we have limited our analyzes to dates with uncertainties less than 200 ^{14}C years, this shows that the samples below 150-170 cm depth dates differ statistically as their dates are above 200 ^{14}C year differences. The difference in ^{14}C depletion has been accounted for by adjusting ^{14}C values relative to measured ^{13}C values or by calculations assuming an expected $\delta^{13}C$ value. In this study, ^{14}C dates were calculated assuming $\delta^{13}C$ values of -3 as per LLNL as shown in Table 7.2.

By aligning the dates in sequence, it can be seen that the deposits in the lower half of site accumulated more slowly than in the upper half. Given that the upper half has much higher densities of cultural material, faunal remains and marine shell, we can propose the occupation was more intensive, involved perhaps more people and activities, and the nature of the site more closely resembles a shell midden than the lower part. The similarity in faunal and cultural

remains of lower deposit with those found at site KBA (Sadr, 2007), and the similar span of occupation, suggest that the lower occupation at KBB may also have functioned as a special location for feasts and not as a conventional habitation sites. The upper part of the occupation with its richer and more diverse material remains suggests a more conventional habitation site/shell midden. The difference in material culture and nature of occupation between lower and upper KBB is thus considerable.

Isotopic analysis in terms of the $^{12}C/^{13}C$ and $^{18}O/^{16}O$ of the KBB GSB3 (at depth of 120-132 cm, $d^{13}C/^{12}C$ = -1.0, $d^{18}O/^{16}O$ = 0.6) and KBB GAS3 (at depth of 100-111 cm, $d^{13}C/^{12}C$ = 0.3, $d^{18}O/^{16}O$ = 0.6) (Sadr and Woodborne, 2013), in combination with radiocarbon dating will assist in determining the diet of the occupants at the site. This falls out of the scope of the present study. The intention is to take it further in the future and perform more analysis at iThemba LABS when the AMS system is in full operation.

CHAPTER 8
CONCLUSIONS

The main objective of this thesis has been the upgrade and development of the iThemba LABS 6 MV EN Tandem Accelerator to AMS system with respect to applications in environmental sciences and archaeology. The AMS capability to measure isotopic ratios in extremely low levels as well as extremely low mass samples enabled the applications discussed in Chapter 6 and Chapter 7 which could not have been performed with same sensitivity, small samples in μg and/or short measuring time of less than five minutes in a (archeological samples) by any other method available at present.

The design and technical development of the 6 MV Tandem accelerator for AMS system has been completed during the first half of the year 2014. The range of capabilities of the accelerator is widened by this upgrade from analytical tool for material physics to flexible tool in dating and wide variety of AMS applications. The facility is now ready to perform AMS measurements, optimized for ^{10}Be and ^{14}C isotopes as a start. Applications with radioisotopes other than ^{14}C can be considered too. The main impetus for improvements of our Tandem system is the developing interest within the accelerator community in South Africa on actinide and cosmogenic isotopes.

One of the most crucial parts regarding a high quality AMS system lies with the ion beam source. In this regard, the present design of the AMS system comprises of probably the best model of an ion source; that is the third generation high-specification source developed at the CAMS/LLNL with low emittance and high luminosity. Beam optics calculations have been performed with respect to the new AMS design on the low energy injection beam line coupling the Livermore source to the Tandem via a series of optical elements including Einzel lenses and a 90^{o} electrostatic analyzer and a 90^{o} double focusing magnet. Care was taken to model the

electrostatic tubes of the Tandem in terms of the appropriate field gradients and the respective focusing effects. The beam optics calculations of the low energy system show that the beam is clearly transported through the injection magnet and well matched to the acceptance of the accelerator tubes. Similar beam optics calculation has been performed on the high energy beam line for iThemba LABS AMS system.

The calculations for both the LE and HE systems were then compared with real beam profiles using a ^{14}C beam produced from standards of a respective NBS Oxalic acid I, Oxalic acid II (NIST-SRM-4990C), ANU sucrose sample and also graphite. The initial tests indicate that the coupling of the ion source to the low energy injection line matches the beam optics models.

Distinguishing between different anthropogenic activities such as contemporary wood burning or fossil fuel burning was made possible for the Lephalale site in South Africa using the ^{14}C as indicator in AMS measurements.

The AMS analysis of samples collected over three weeks prior to the newly built 4.8 gigawatts Medupi power station coming onto operation. This study, therefore, has set a landmark of the existing pollution which can be used in the years to come after the Power Station comes in full operation. The analysis has revealed that 53% of collected particulate carbon at Lephalale site is associated with contemporary carbon. The highest fraction of contemporary carbon with 67.1% corresponds to a night sample (i.e. Marapong_20) with sampling having been taken over the night of the 1-2 April 2012. The highest fraction of fossil carbon with 61.2% corresponds to a day sample (i.e. Marapong_21) which was sampled on 2 April 2012. The contemporary carbon fraction is the dominant fraction at site, except on three occasion were the fossil fraction is high than contemporary fraction. Night here is defined as the period between 21h00 and 09h00. It is important to note that this is the period in rural South Africa which falls just after wood fires are lit for cooking as well as for heating. This wood

burning, therefore, constitutes the largest source of the contemporary carbon. Despite the various efforts in many other studies to distinguish between contemporary carbon and fossil carbon, no other assessment method provides the definitive results that can be obtained from radiocarbon measurements as has been demonstrated in this study. Although other single and multiple chemical tracers have been suggested, these provide only a qualitative estimate of the wood burning contribution and then only if it is one of the dominant sources.

Our future intention is to perform extensive studies in the area after the Medupi power station comes to operation and assess the different contributions to the monthly atmospheric carbon aerosol at Lephalale. Thereafter, sampling covering the entire year needs to take place in order to understand pollution dynamics in terms of absolute aerosol and carbon concentration.

The PIXE analysis of aerosols samples at Lephalale reveals the presence of 6 elemental pollutants, namely K, Ca, Ti, Mn, Fe and Zn. This elemental composition has been used in enrichment factor analysis of soil. Extraction of the enrichment factor with respect to Fe shows that Ca, Ti and Mn have their EF values of less than 10 which is indicative of soil dust as a source. The EF value of K is depleted with respect to Fe. Whereas the EF value of Zn with respect to Fe is highly enriched element.

In summary, source apportionment reveals that soil dust has 78.54% detected source at Lephalale. The residual contributed with 21.426%. This source could be made-up of many sources and it was beyond the scope of this research to try and break this down into all the contributing sources.

The second part of the present study was concerned with AMS radiocarbon dating of archaeological artefacts from the site of KBB. In Sadr (1998) it was hypothesized that the makers of lugged pottery in the southwestern Cape were probably immigrant Khoi-speaking

pastoralists and that they had replaced the local San herding population who made and used spouted pots. The test of this hypothesis depended to some extent on whether the switch from lower to upper occupation at KBB was a rapid event or whether an occupational hiatus existed between the lower and upper deposits of KBB. A hiatus would allow space for an argument that the spouted pottery tradition evolved into the lugged pottery tradition, and that the excavations at KBB had simply not intercepted this period of transition.

The radiocarbon dates are in agreement with the other studies that have been done on the site which shows that the age of artifacts are less 2000 years (Smith, 2006; Sadr and Smith, 1991). The samples were from stratigraphic level of square A3 as shown in Fig. 7.3. It was evident from excavation that the stratigraphy was horizontal across the site, and that the cultural remains were reasonably homogeneous (Smith, 2006).

The new AMS dates reported here suggest the high probability that indeed there was a hiatus between the two occupations designated as lower and the upper KBB. The significant changes seen in material culture styles as well as in the nature of occupation and change in accumulation rate of deposits therefore do not necessarily indicate a cultural replacement caused by the arrival of a new population. This implies that the occupants of lower KBB may also have been done Khoi-speakers, and not local San. Radiocarbon dates from KBB cannot resolve the situation any further.

The question of why this part of Kasteelberg probably was abandoned for a short time around AD 1000 and where the cultural evolution from the spouted ware tradition to that of the lugged ware tradition took place remains to be investigated. The transition could have occurred on Kasteelberg but at a location that has not yet been excavated. But it could also have occurred far away following a general abandonment of area around Kasteelberg. We know that there was significant change towards a warmer and (in the winter rainfall zones such as the south-

western Cape) drier climate around AD 1000 (the Medieval warming epoch e.g. see Tyson et al., 2001; Woodborne et al., 2015). We also know that there is an increase in the number of radiocarbon dates from this period in coastal areas a hundred or more kilometres to the north of Kasteelberg (Sadr, 2014), which could be interpreted as a general population increase there just when the numbers of radiocarbon dates around Kasteelberg started a decline. This could suggest that the inhabitants of KBB, along with those from many other sites in its vicinity abandoned the area and moved north along the coast towards the summer rainfall areas which would have started to receive more rain with the onset of the Medieval warming trend. But all this remains highly speculative and other possibilities can also be entertained. Testing such diverse hypotheses is a subject for future research.

REFERENCES

AccelSoft Inc., Del Mar, CA 92014.

Alvarez, L. W. and Cornog, R. (1939). Helium and Hydrogen of Mass 3. *Physical Review, 56*, p613-613.

Annegarn, H. J., Braga-Marcazzan, G. M., Cereda, E., Marchionni, M. and Zucchiatti, A. (1992) : Source profiles by unique ratios (SPUR) analysis - Determination of source profiles from receptor-site streaker samples". *Atmospheric Environment, 26A*, p333-343.

Arnold, J. and Libby, W. (1949). Age determinations by radiocarbon content: checks with samples of known age. *Science,110*, p678-680.

Artaxo P., Storms H., Bruynseels, F., Van Grieken R.E. and Maenhaut, W. (1998). "Composition and sources of aerosols from the Amazon Basin". *Journal of Geophysical Research, 93*, p1605-1615.

Balasse, M., Smith, A. B., Ambrose, S. H., and Leigh, S. R. (2003). Determining Sheep Birth Seasonality by Analysis of Tooth Enamel Oxygen Isotopic Ratios: The Late Stone Age Site of Kasteelberg (South Africa). *Journal of Archaelogical Science, 30*, p205-215.

Barbieri, C., Güldemann, T., Naumann, C., Gerlach, L., Berthold, F., Nakagawa, H., Mpololoka, S.W., Stoneking, M., Pakendorf, B. 2014. Unravelling the complex maternal history of Southern African Khoisan populations. *American Journal of Physical Anthropology* 153(3):435-48.

Barnard, Alan 1992. Hunters and herders of Southern Africa: a comparative ethnography of

the Khoisan peoples. Cambridge: Cambridge University Press.

Bench, G., Fallon, S., Schichtel, B., Malm, W. and McDade, C. (2007). Relative contributions of fossil and contemporary carbon sources to PM 2.5 aerosols at nine Interagency Monitoring for Protection of Visual Environments /(IMPROVE) network sites. *Journal of Geophysical Research,* Vol. 112,D10205,doi:10.1029/2006JD007708

Bench, G. (2004). Measurements of Contemporary and Fossil Carbon contents of $PM_{2.5}$ Aerosols: Results from Turtle dome, Yosemite National Park. *Environ. Sci. Technol, 38*: p2424-2427

Bennet, C. L., Beukens, R. P., Clover, M. R., Gove, H. E., Liebert, R. B., Litherland, A. E., Purser, K. H., and Sondheim, W. (1977). Radiocarbon dating using electrostatic accelerators: negative-ions provide the key. *Science*, 198, p508-510.

Berger, L. R., Lacruz, R., and de Ruiter, D. J. (2002). Brief Communication: Revised Age Estimates of Australopithecus-Bearing Deposits at Sterkfontein, South Africa. *Americal Journal of Physical Anthropolgy, V119:*p192-197.

Bethe, H. A., Korff, S. A., and Placzek, G. (1940). On the Interpretation of Neutron Measurements in Cosmic Radiation. *Phys. Rev., 57*, p573.

Bleek, D. (1928). –The Naron, Cambridge, Cambridge University Press.

Blench, R. (2007). Special Research Centre ACACIA project "Migration, Settlement and Cultural History on the Basis of Linguistic Sources", University of Cologne. Presented at Königswinter, March 28-30, 2007.

Boonzaier, E., Malherbe, C., Smith, A., and Berens, P. (1996). The Cape Herders: A history of the Khoikhoi of Southern Africa, David Philip, Cape Town and Johannesburg, p25-27.

Bronk Ramsey, C. (2009). Bayesian analysis of radiocarbon dates. *Radiocarbon, Vol.51,*

p337-360.

Brown, K.L. (1975). A First- and Second-Order Matrix Theory for the Design of Beam Transport Systems and Charged Particle Spectrometers. *SLAC Report-75.*

Brown, T. A. (2013). Private communication.

Brown, T. A., Marchetti, A. A., Martinelli, R. E Cox, C. C., Knezovich, J. P., and Hamilton, T. F. (2004). Actinide measurements by accelerator mass spectrometry at Lawrence Livermore National Laboratory. *Nucl. Instrum. Meth. Phys. Res.* B223, p788-795.

Brown, T. A., Roberts, M. L. and Southon, J. R. (2000). Ion-Source Modeling and Improved Performance of the CAMS High-Intensity Cs-Sputter Ion Source *Nucl. Instrum. Meth. Phys. Res.* B172, p344-349.

Brown, T. A., Roberts, M. L. and Southon, J. R. (2000). Ion-Source Modeling and Improved Performance of the CAMS High-Intensity Cs-Sputter Ion Source *Nucl. Instrum. Meth. Phys. Res.* B172, p344-349.

Brown, T. A. and Gillespie, G. H. (1999). Optics Elements for Modeling Electrostatic Lenses and Accelerator Components: III. Electrostatic Deflectors. *8th International Conference on Accelerator Mass Spectrometry, Vienna, Austria,* September 6-10.

Brown, T.A. and Southon, J. R. (1997). Corrections for contamination background in AMS ^{14}C measurements. *Nucl. Instrum. Meth. Phys. Res. B123*, p208-213.

Chow, J. C., Watson, J. G., Lowernthall, D. H., Solomon, P. A., Magliano, K. L., Ziman, S. D., and Willard Richards, L. (1992). PM_{10} source apportionment in California's San Joaquin valley. *Atmos. Environ. A.-Gen., 26,doi:1016/0960-1686(92)9035-T.*

Crandall , K. R. and Rusthoi, D. P. (1997). " TRACE 3D Documentation". , LA-UR-97-986, Los Alamos National Laboratory (1997).

Copley, M. S., Hansel, F. A., Sadr, K. and Evershed, R.P. 2004. Organic residue evidence for the processing of marine animal products in pottery vessels from the pre-colonial archaeological site of Kasteelberg D east, South Africa. *South African Journal of Science* 100: p279-283.

Currie, L. A. (2000a). Evolution and multidiscliplinary frontiers of ^{14}C aerosol science. *Radiocarbon, Vol 42, No.1*, p115-126.

Currie, L. A., Kessler, J. D., Marolf, J. V., Mc Nichol, A. P., Stuart, D. R., Donoghue, J. C., Donahue, D.J., Burr, G.S., and Biddulph, D. (2000b). Low-level (submicromole) environmental ^{14}C metrology. *Nucl. Instrum. Meths. Phys. Res. B172*, p440-448.

Currie, L. A., and Klouda, G. A. (1984). Atmospheric Carbon: The importance of accelerator mass spectrometry. *Nucl. Instrum. Meths. Phys. Res. B5*, p371-379.

Davisson C. J. and Calbrick C. J. (1932). *Phys. Rev.* 42, p580

Davisson C. J. and Calbrick C. J. (1931). *Phys. Rev.* 38, p585

Deacon, J. (1984). Later Stone Age people and their descendants in southern Africa. In Klein, R. G. (ed.), *Southern African Prehistory and Paleoenvironments,* A. A. Balkema, Rotterdam, p 221-328.

Deacon, H. J., Deacon, J., Brooker, M., and Wilson, M. L. (1978). The evidence for herding at Boomplaas Cave in the southern Cape, South Africa. *South African Archaeological*

De Vries, H. L. and Barendsen, G. W. (1954). Measurements of Age by the Carbon-14 Techniques. *Nature, 174*:p1138-1141

Dewar, G., Reimer, P. J., Sealy, J. and Woodborne, S. (2012). "Late-Holocene marine radiocarbon reservoir correction (*ΔR*) for the west coast South Africa". The Holocene online version http://hol.sagepub.com/content/early/2012/06/18/0959683612449755 Accessed 23 June 2013

Dockery, D. W., Pope, C. A., Xu, X., Spengler, J. D., Ware, J.H., Fay, M. E., Ferris, B.G., and Speizer F. E. (1993). An Association between Air Pollution and Mortality in Six U.S. Cities. *New Engl. J. Med., 329*, p1753-1759, doi:101056/NEJM199312093292401.

Donahue, D. J., Linick, T. W., and Jull, A. J. T. (1990). Isotope-Ratio and Background Corrections for Accelerator Mass Spectrometry Radiocarbon Measurements. *Radiocarbon, Vol. 32, No.2.* p135-142.

Fallon, S. J., Guilderson, T. P. and Brown, T. A. (2007). CAMS/LLNL ion source efficiency revisted. *Nucl. Instrum. Meth. Phys. Res. B 259*, p106-110.

Fifield, L. K., Cresswell, R. G., Tada, M. L. D, Ophel, T. R., Day, J. P., Clasher, A. P., King, S. J and Priest, N. D. (1996). Accelerator mass spectrometry of plutonium isotopes.. *Nucl. Instrum. Meth. Phys. Res.* B117, p295-303.

Fifield, L. K., Clasher, A. P., Morris, K., King, S. J., Cresswell, R. G., Day, J. P., and Livens, F. R., (1996). Accelerator mass spectrometry of planetary elements. *Nucl. Instrum. Meth. Phys. Res.* B123, p400-404.

Gillespie, G. H. and Brown, T. A. (1999). "Optics elements for modeling electrostatic lenses and accelerator components II. Accelerator columns". *Nucl. Instrum. Meth. Phys. Res. A427*, p315-320.

Gillespie, G. H. (1998). in: Eyberger, C. E., Pardo, R. C., White, M. M. (Eds), *Proceeding of the XIXth International Linear Accelerator Conference*, Chicago, Illinois, USA, Argonne National Laboratory,ANL-98/28,p150.

Gillespie, G. H. and Brown, T. A. (1999). "Optics elements for modeling electrostatic lenses and accelerator components I. Einzel Lenses". http://accelconf.web.cern.ch/accelconf/pac97/papers/8P084.PDF. Accessed 07 September 2016.

Gillespie, G. H. (1995). Mac Trace User Inputs for Einzel Lens Models, prepared for MACcelerator project, GHGA-95-449-TM.

Gillespie, G. H. and Hill, B. W. (1992). "A Graphical User Interface for TRACE 3-D Incorporating Some Expert System Features," *1992 Linear Accelerator Conference Proc., AECL-10728*, p787-789.

Gordon, G.E., . (1980). "Receptor Models". *Environ. Sci. Technol.Vol.14,No. 7*, p792-800.

Guilderson, T. P., Southon, J. R., and Brown, T. A. (2003). High-Precision AMS ^{14}C Results on TIRI/FIRI Turbidite. *Radiocarbon, Vol. 45,No. 1*: p75-80.

Güldemann, T. 2008. A linguist's view: Khoi-Kwadi speakers as the earliest food-producers of southern Africa. *Southern African Humanities* 20(1): 93–132.

Guo, Z., Liu, K., Lu, X., Ma, H., Li, K., Yuan, S., and Wu, X. (2000). The use of AMS radiocarbon dating for Xia-Shang-Zhou chronology. *Nucl. Instrum. Meth. Phys. Res. B 172*, p724

Hajdas, I., Bonani, G., Slusarenko, I.Y. and Seifert, M. (2004). Chronology of pazyryk 2 and Ulandryk 4 Kugrans based on high resolution radiocarbon dating and dendrochronology-a step towards precise dating of Scythian Burials.- IN: Scott, E.M. (ed): Impact of the Environment on the Human Migration in Eurasia:p107-116; Printed in the Netherlands (Kluwer Academic Publishers).

Hellborg, R, and Skog, G (2008). Accelerator Mass Spectrometry. *Mass Spectrometry Reviews, Vol.27 issue No. 5*, p398-427.

Hellborg, R, and Skog, G (2007). Accelerator Mass Spectrometry. *Mass Spectrometry Reviews,* Doi 10.1002/mas.20172. Published online 9 May 2008 in Wiley InterScience (www.interscience.wiley.com).

Henn, B.M., Gignoux, C., Lin, A.A., Oefner, P.J., Shen, P., Scozzari, R., Cruciani, F., Tishkoff, S.A., Mountain, J.L. & Underhill, P. 2008. Y-chromosomal evidence of a pastoralist migration through Tanzania to southern Africa. *PNAS* 105(31):10693-98.

Hildemann, L. M., Klinedinst, D. B., Klouda, G. A. and Currie, L. A. (1994). Sources of Urban Contemporary Carbon Aerosol. *Environ. Sci. Technol., Vol. 28, No. 9*, p1565-1576.

Hobbs, P. V. (2000). Introduction to Atmospheric Chemistry. *Cambridge University Press.* Cambridge.

Hotchiks, M. A. C., Child, D., Fink, D., Jacobsen, G. E., Lee, P. J., Mino, N., Smith, M. A., and Tuniz, C. (2000). Measurement of ^{236}U in environmental media. *Nucl. Instrum. Meth. Phys. Res. B 172*, p659.

Jo, H. C., Bae, J. D. and Bak, H. I. (1991). Ion Optical Study on the He^{++} Beam Transport System of the SNU 1.5-MV Tandem Van de Graaff Accelerator. *Journal of the Korean Nuclear Society, Vol. 23, No.4*, p426-437.

Johansson, S. A. E. and Campbell, J. L. (1988). PIXE: A Novel Technique for Elemental Analysis. John Wiley: Chichester.

Juma, S. M., Jalil, F. A. and Mohannad, I. L. (2007). Computations on the optical properties of the electrostatic symmetric quadrupole triplets lens. *Journal of Al-Nahrain University, Vol. 10 (1),* p73-77.

Key, R. M. (2010). Radiocarbon. *Unpublished,* Atmospheric and Oceanic Sciences program, Princeton University, Princeton, NJ 08544

Kinahan, J. (1995). A new archaeological perspective on nomadic pastoralist expansion in

south-western Africa. *Azania 29/30*: p211-226.

Klein, R. G. (1986). The prehistory of stone age herders in the Cape Province of South Africa. *South African Archaeological Society, Goodwin Series 5*: 5-12.

Kolbe, P. (1719). *Caput Bonae Spei Hodiernum, das ist Vollständige Beschreibung des Africanischen Vorgebürges der Guten Hofnung. Conrad Monath, Nuremberg*.

Korff, S. A. and Danforth, W. E. (1939). Neutron Measurements with Boron-Trifluoride Counters. *Phys. Rev., 55,* p980

Kurie, F. N. D. (1934). A New mode of disintegration Induced by Neutrons. *Phys. Rev., 45,* p904.

Kutschera, W. (2010). "AMS and climate change". *Nucl. Instrum. Meth. Phys. Res.* B268, p693-7000.

Kuzmin, Y. V. (2009). Radiocarbon and the old world archaeology: shaping a chronological. *Radiocarbon, Vol.51, N0.1,* p149-172

Larson, J. D. and Jones, C. M. (1977). "Phase space acceptance and emittance in beam transport with application to tandem accelerators". *Nucl. Instrum and Methods, Vol.140,* p489-504.

Levin, I, Hammer, S., Kromer, B. and Meinhardt, F (2008) Radiocabon observations in atmospheric CO_2: Determining fossil fuel CO_2 over Europe using Jungfraujoch observations as background. *Science of The Total Environment,*391, p211-216.

Levin, I and Hesshaimer, V. (2000). "Radiocarbon- a unique tracer of global carbon cycle dynamics. *Radiocarbon, Vol.42, No.1,* p69-80.

Lewis, C. W., Baumgardener, R. E., Stevens, R. K., Claxton, L.D. and Lewtas, J. (1988). Contribution of woodsmoke and motor-vehicle emissions to ambient aerosol mutagenicity. *Environ. Sci. Technol., 22,* p968-971.

Libby, W.F. (1955). *Radiocarbon Dating*. University of Chicago Press, Second Edition.

Litherland, A. E. (1984). Accelerator mass spectrometry. *Nucl. Instrum. Meth. Phys. Res. B 5,* p100-108.

Locker , G. L. (1933). *Phys. Rev, 44;* p779.

Loyd, D. H., Vogel, J. S. and Trumbore, S. (1991). Lithium Contanimation in AMS Measurements of ^{14}C. *Radiocarbon, Vol.33, No.3,* p911-934.

Macholdt, E., Lede, V., BarbieriI, C., Mpoloka, S. W., Chen, H., Slatkin, M., Pakendorf, B. & Stoneking, M. 2014. Tracing pastoralist migrations to southern Africa with lactase persistence alleles. *Current Biology* 24(8): 875-79.

Maenhaut, W. and Cafmeyer, J., . (1987). "Particle induced X-ray emission analysis and multivariate techniques: An application to the study of the sources of respirable atmospheric particles in Gent Belgium". *Journal of Trace and Microprobe Techniques,* 5, p135-158.

Manning, M. P. and Reid, R. C. (1977). C-H-O Systems in the Presence of an Iron Catalyst. *Industrial & Engineering Chemistry Process Design and development, 16(3),* p358-361

Mason, B. (1982). *Principles of Geochemistry*. 4th Edition. J. Wiley: New York.

Meier, J. (20017. Matching of the beam from a negative-ion source for capture in a Penning trap. Diploma thesis, Faculty of Physics and Astronomy, University of Heidelberg, Max Planck Institute for Nuclear Physics, Germany.

http://www.mpi-hd.mpg.de/kellerbauer/en/articles/2007/Meier_Diplomarbeit_2007.pdf

Mitchell, P. (2002). The archaeology of southern Africa. Cambridge: Cambridge University Press.

Montgomery, C. G. and Montgomery, D. D. (1939). The intensity of neutrons of thermal energy in the atmosphere at sea level. *Phys. Rev. 56,* p10-12

Moodie, D. (1838). *The record 0/ a series 0/ official papers relative to the condition*

and treatment 0/ native tribes 0/ South Africa. Volume I and III.

Amsterdam:Balkema.

Muller, R A. (1979), Radioisotope dating with accelerators: *Physics Today, Vol. 32, No. 2,*

p23-30.

Nelson, D. E., Korteling, R. G. and Stott, W. R. (1977). Carbon-14 direct detection at natural concentrations. *Science, 198,* p507-508.

Ognibene, T. J., Brown, T. A., Knezovich, J. P., Roberts, M. L., Southon, J. R., and Vogel, J. S. (2000). Ion-optics calculations of the LLNL AMS system for biochemical ^{14}C measurements. *Nucl. Instrum. Meth Phys. Res. B172*, p47-51.

Oswald, W.W., Anderson, P. M., Brown, T. A., Brubaker, L. B., Hu, F. S., Lozhkin, A. V. Tinner, W., and Kaltenrieder, P. (2005). Effects of sample mass and macrofossil type on radiocarbon dating of arctic and boreal lake sediments. *The Holocene, 15(5)*, p758-767.

Patrick, M., Smith, A. and De Koning, A.J. (1985). Gas-liquid chromatographic analysis of fatty acids in food residues from ceramics found in the south-western Cape, South Africa. *Archaeometry 27(2):* p231-236.

Parkington, J. E., Yates, R., Manhire, A., and Halkett, D. (1986). The social impact of pastoralism in the southwestern Cape. *Journal of Anthropological Archaeology 5:* p313-329.

Parkington, J. E. (1984). Changing views of the Later Stone Age of South Africa. *Advances in World Archaeology 3*: p89-142.

Pearson, G. W., Pilcher, J. R., Baillie, M. G. L., Corbett, D. M., and Qua, F. (1986). High-precision ^{14}C measurement of Irish oaks to show the natural ^{14}C variations from AD 1840 to 5210 BC. *Radiocarbon, 28(2B)*, p911-934.

Pelletrons (2014). Principle of operation of ion sources. Available from: http://www.pelletron.com/necpub.htm#ion. Accessed 12 July 2014.

Piketh, S.J., Formenti, P., Annegarn, H.J. and Tyson, P.D. (1999). "Industrial characterization at remote site in South Africa". *Nucl. Instrum. Meth. Phys. Res. B150*, p350-355.

Piotrowska, N., Blaauw, M., Mauquoy, D., and Chambers, F. M. (2010). Constructing deposition chronologies for peat deposit using radiocarbon dating. *Mires and Peat, Vol 7, Article 10*, p1-14.

Purser, K. H. (1992). A high throughput ^{14}C accelerator mass spectrometry. *Radiocarbon, Vol. 34, No.3*, p458-467.

Raven-Hart, R. 1967. *Before Van Riebeeck.* Cape Town: Struik.

Reimer P. J., Baillie, M. G. L., Bard, E., Bayliss, A., Beck, J. W., Blackwell, P. G., Bronk Ramsey, C., Buck, C. E., Burr, G. S., Edwards, R. L., Friedrich, M., Grootes, P. M., Gilderson, T. P., Hajdas, I., Heato, T. J., Hogg, A. G., Hughen, K. A., Kaizer, K. F., Kromer, B., McCormac, F. G., Manning, S. W., Reimer, R. W., Richards, D. A., Southon, J. R., Talamo, S., Turney, C. S. M., van der Plicht, J., Weyhenmeyer, C. E. (2009). IntCal09 and Marine09 radiocarbon age calibration curves, 0-50,000 years cal BP. *Radiocarbon, Vol.51*, p1111-1150.

Reimer, P. J., Baillie, M. G. L., Bard, E., Bayliss, A., Beck, J. W., Bertrand, C. J. H., Blackwell, P. G., Buck, C. E., Burr, G. S., Culter, K. B., Damon, P. E., Edwards, R. L., Fairbanks, R. G., Friedrich, M., Guilderson, T. P., Hogg, A. G., Hughen, K. A., Kromer, B., McCormac, G., Manning, S., Ramsey, C. B., Reimer, R. W., Remmele, S., Southon, J. R., Stuiver, M., Talamo, S., Taylor, F. W., van der Plicht, J., and Weyhenmeyer, C. E. (2004). "INTCA04 TERESTRIAL RADIOCARBON AGE CALIBRATION, 0-26 CAL KYR BP". *Radiocarbon: Vol.46, No.3*, p1029-10584.

Rheingrover, S.W. and Gordon G.E., (1988). "Wind-trajectory method for determining compositions of particles from major air pollution sources". *Aerosol Science and Technology, 8*, p29-61.

Roberts, M. L., Burton, J. R., Elder, K. L., Longworth, B. E., McIntyre, C. P., von Reden, K. F., Han, B. X., Rosenheim, B. E., Jenkins, W. J., Galutschek, E., and McNichol, A. P. (2010) . A High-Performance ^{14}C Accelerator Mass Spectrometry system. *Radiocarbon, Vol 52, No. 2–3*, p 228–235

Roberts, M. L., Norman, P. J., Garibaldi, R.S. and Hornady, R. S. (1994). The new LLNL AMS sampler changer. *Nucl. Instrm. Meth Phys. Res. B92*, p111-1114

Rudner, J. (1968). Strandloper pottery from South and South West Africa. *Annals of the South African Museum 49: p*441-663 .

Rumbaugh, L. H. and Locker, G. L. (1936). The specific ionization of cosmic ray particles as determine by Geiger-Muller counter efficiency. *Phys. Rev. 49*, p854-855.

Rupprecht & Patashnick Co. Inc. (2012). *The Partisol-plus Model 2025 Sequential Air Sampler*. Available from: www.rpco.com Accessed 20 October 2012.

Sadr, K. 2015. Livestock First Reached Southern Africa in Two Separate Events. *PLoS ONE* 10(8): e0134215. doi:10.1371/journal.pone.0134215

Sadr, K. 2014. Radiocarbon Dates, Stone Tools and the Origins of Herding on the West Coast of South Africa. *Reports in African Archaeology 6*, Frankfurt: Africa Magna Verlag

Sadr, K. and Woodborne, S. (2013). Unpublished data for delta $^{13}C/^{12}C$ and delta $^{18}O/^{16}O$ form Kasteelberg B site.

Sadr, K. (2008). Invisible herders? The archaeology of KhoiKhoi pastroralists. *Southern African Humanities, 20:* p179-203

Sadr, K. (2007). Early First Millenium Pastoralists on Kasteelberg? The UB/UCT Excavation at KBA. *South African Archaeological Bulletin, 62(186):* p154-161.

Sadr, K. and Fauvell-Aymar (2006). "Ellipsoid grinding hollows on the west coast of South Africa", *Southern African Humanities Vol.18, No.2*, p29-50.

Sadr, K. (1998). The first herders at the Cape of Good Hope. *African Archaeological Review, 15:* p101-132.

Sadr, K. and Smith, A. B. (1991). On ceramic variation in the South-Western Cape, South Africa. *South African Archaeological Bulletin 46*, p107-114.

Schapera, I. (1930). The Khoisan Peoples of South Africa, London , Routledge and Kegan.

Schichtel, B. A., Malm, W. C., Bench, G., Fallon, S., McDade, C. E., Chow, J. C., and Watson, J. G. (2008.). Fossil and contemporary fine particle carbon fractions at 12 rural and urban sites in the United States. *Journal of Geophys. Res., 113*, D02311, doi:10.1029/2007JD008605.

Sealy, J.C. and Yates, R. (1994). "The chronology of the introduction of pastoralism to the Cape, South Africa", *Antiquity 68(582*), p58-68.

Senaratne, I. and Shooter, D. (2004). "Elemental composition in source identification of brown haze in Auckland, New Zealand". *Atmospheric Environment: 38(19)*, p3049-3059.

Slota, J. R., Jull, A. J. T., Linick, T. W. and Toolin, L. J. (1987). Preparation of Small Samples for ^{14}C Accelerator Target by Catalytic Reduction of CO. *Radiocarbon, Vol. 29, No.2*, p303-306.

Smith, A. B. (2006). Excavations at Kasteelberg and Origins of the KhoiKhoin in the Western Cape, South Africa. *Cambridge Monographs in African Archaeology, 66*, p32.

Smith, B. W. and Ouzman, S. (2004). Taking stock: identifying KhoiKhoin herder rock art.

*Current Anthropology, 45:*p499-526.

Smith, A. B. and Pheiffer, R. (1993). The Khoikhoi at the Cape of Good Hope: *Seventeenth-century Drawings in the South African Library.* Cape Town: The Library

Smith, A. B. (1992). Kasteelberg. In (A. B. Smith & B. Mütti, Eds). *Unpublished Guide to Archaeological Sites in the South-western Cape. South African Association of Archaeologists Conference July 5-9 1992. Cape Town*, p28-30.

Smith, A. B. (1992). *Pastoralism in Africa,* Witwatersrand University Press, Johannesburg.

Southon, J. R. and Santos, G. M. (2007). Life with MC-SNICS. Part II: Further ion source development at the Keck carbon cycle AMS facility. *Nucl. Instrm. Meth Phys. Res.* B259, p88-93

Southon, J. R. and Roberts, M. L. (2000). Ten years of sourcery at CAMS/LLNL– Evolution of a Cs ion source, *Nucl. Instr. and Meth. B 172*, p257.

Southon, J. R. , Vogel, J. S., Trumbore, S. E., Davis, J. C., Roberts, M. L., Caffee, M. W., Finkel, R. C., Proctor, I. D, Heikkinen, Berno, A. J., and Hornady, R. S. (1992). Progress in AMS Measurements at the LLNL Spectrometer. *Radiocarbon, Vol. 34, No.3,* p473-477.

Spalding, K. L., Arner, E, Westermark, P. O., Bernard, S., Buchholz, B. A., Bergmann, O., et al . (2008). "Dynamic of fat cell turnover in humans". *Nature 453 (7196*), p783-787.

Spalding, K. L., Bharwaj, R. D, Buchholz, B. A., Druid, H., Frisen, J. (2005). "Retrospective birth dating of cells in humans". *Cell* 122 *(1),* p133-143.

Septier, A. (1980). Applied Charged Particle Optics. *Academic Press, Vol 2, Part 2.*

Steier, P., Golser, R., Kutschera, W., Liechtenstien, V., Priller, A., Valenta, A., and Vockenhuber, C. (2002). Heavy ion AMS with a "small" accelerator. *Nucl. Instrum. Meth. Phys. Res*. B 188, pp 283-287

Steier, P. (2000). "Exploring the limits of VERA: A universal facility for Accelerator Mass Spectrometry". *PhD thesis, VERA.*Unpublished.p13

Stewart, B.A. 2005. Charring patterns on reconstructed ceramics from Dunefield Midden: implications for KhoiKhoi vessel form and function. *Before Farming 2005*: 11-28 [online: 2005/1 article 1]

Stuiver, M., Reimer, P. J., and Reimer, R. (2005). Calib 6.1. www.calib qub.ac.uk/calib

Stuiver, M., Reimer, P. J., Bard, E., Beck, J. W., Burr, G. S., Hughen, K.A., Kromer, B., McCormac, G., van der Plicht, J., and Spurk, M (1998). INTCAL98 radiocarbon age calibration, 24,000-0 cal BP. *Radiocarbon, Vol.40*, No.3, p1041-1083.

Stuiver, M., Long, A., and Kra, R. S., (eds) (1993). Calibration 1993. *Radiocarbon, Vol.*35, No.1.

Stuiver, M and Braziunas, T. (1993). Sun, ocean, climate and atmospheric $^{14}CO_2$: an evaluation of causal and spectral relationships. *The Holocene, 3(4),* p289-305.

Stuiver, M. (1993). A note on single-year calibration of the radiocarbon time scale Ad 1510-1954. *Radiocarbon, Vol.35, No.1,* p67-72

Stuiver, M. & Reimer, P.J. (1993). Extended ^{14}C database and revised CALIB radiocarbon

calibration program. *Radiocarbon, Vol.35*, p215–230.

Stuiver, M and Reimer, P. (1989). Histograms Obtained from Computerized Radiocarbon Age Calibration. *Radiocarbon, Vol.31*, p817-823.

Stuiver, M and Reimer, P. (1986). A Computer-Program for Radiocarbon Age Calibration. *Radiocarbon,Vol.*28, p1022-1030.

Stuiver, M and Kra, R. S. (eds) (1986). Calibration Issue: Proceedings of the 12th International Radiocarbon Conference, Trondheim, Norway Histograms Obtained from Computerized Radiocarbon Age Calibration. *Radiocarbon, Vol.*28, No.2B.

Stuiver, M. (1983). International Agreements and the Use of the Oxalic Acid Standards. *Radiocarbon, Vol. 25*, p793-795

Stuiver, M. and Polach, H. A. (1977). "DISCUSSION REPORTING OF 14C DATA". *Radiocarbon*: *Vol.19*, No.3, p355-363.

Suess, H. E. (1955). Radiocarbon Concentration in Modern Wood. *Science,*122, p415-417.

Suter, M., Jacob, S. A. W., and Synal, H. –A (2000). Tandem AMS at sub-MeV energies-Status and prospects. *Nucl. Instrum. Meth. Phys. Res. B 172*, p144-151.

Suter, M., Jacob, S. A. W., and H. A. Synal. (1997). AMS of /sup 14/C at low energies. *Nucl. Instr. Meth. Phys. Res B 172*, p257.

Suter, M. (1990). Accelerator mass spectrometry: state of the art in 1990*. *Nucl. Instrum. Meth. Phys. Res. B 52,* p211-223 .

Synal, H. –A., Döbeli, M, Jacob, S. and Suter, M. (2004). Radiocarbon AMS towards its low-energy limit. *Nucl. Instrum. Meth. Phys. Res. B 223-224*, p339.

Synal, H. –A., Jacob, S. and Suter, M. (2000). New concepts for radiocarbon detection systems. *Nucl. Instrum. Meth. Phys. Res. B 161-163.* p29.

Szidat, S., Ruff, M., Perron, N., Wacker, L., Synal, H. A., Hallquist, M., Shannigrahi, A. S., Yttri, K. E., Dye, C., and Simpson, D. (2009). Fossil and non-fossil source of organic carbon (OC) and elemental carbon (EC) in Goteborg, Sweden. *Atmospheric Chemistry and Physics* 9, p1521-1535.

Szidat, S., Jenk, T. M., Gaggeler, H. M. Synal, H-A, Fisseha, R., Baltensperger, U, Kalberer, M., Samburova, V., Reimann, S., Kasper-Giebl, A., and Hajdas, I. (2004). Radiocarbon (^{14}C)-deduced biogenic and anthropogenic contributions to organic carbon (OC) of urban aerosols from Zurich, Switzerland. *Atmospheric Environment, 38 (24):*p4035-4044.

Thom, H.B. 1952. *Journal of Jan Van Riebeeck.* Vol. I. Cape Town: Balkema.

Tuniz, C., Kutschera, W., Fink,D., and Herzog, G. F. (1998). "*Accelerator Mass Spectrometry: Ultrasensitive Analysis for Global Science.* New York: CRC Press.

Tumey, S., Brown, T., Buchholz, B., Hamiltom, T., Hutcheon, I., and Williams, R. (2009.). Ultra-sensitive measurements of ^{233}U by accelerator mass spectrometry for national security applications. *Journal of Radioanalytical and Nuclear Chemistry. Vol. 282(3), p721*.

Tyson, P. D., Odada, E. O., and Partridge, T. C. (2001). Late Quaternary environmental change in southern Africa: START Regional Syntheses. *South African Journal of Science,* 97(3 & 4): p139.

UCI (2012). UCI KCCAMS Facility. *Graphitization protocol-Hydrogen reduction method (organic and carbonates samples), April 25 2011*. Available from: http://webfiles.uciedu/setyrumbo/public/shortcourse/UCI_H2_Graphitization_04.pdf Accessed 12 May 2012.

Vogel, J. S., Nelson, D. E. and Southon, J. R. (1987). ^{14}C background levels in an accelerator mass spectrometry system. *Radiocarbon, Vol. 29*, No. 3, p323-333.

Vrba, E. S. (1982). Biostratigraphy and chronology, based particularly on Bovidae, of southern African hominid-associated assemblages: Mkapansgat, Sterkfontien, Taung, Kromdraai, Swartkrans; also Elandsfontein (Saldanha), Broken Hill (now Kabwe) and Cave of Hearths. In Proceedings of Congres International de Paleontologic Humaine (de Lumley H, de Lumley M.A., eds), p707-752. Nice: Union International des Sciences Prehistoriques et Protohistroriques.

Wacker, L., Chamizo, E.. Fifield, L.K., Stocker, M., Suter, M., and Synal, H.A. (2005). Measurement of actinides on a compact AMS system working at 300 kV. *Nucl. Instrum. Meth. Phys. Res B, Vol. 240*, pp 452-457

Walker, N. (1983). The significance of an early date for pottery and sheep in Zimbabwe.

South African Archaeological Bulletin, 38: p88-92.

Watson, J. G., Chow, J. C., and Houck, J. E. (2001). $PM_{2.5}$ chemical source profiles for vehicle exhaust, vegetative burning, geological material, and coal burning in Northwestern Colorado during 1995. *Chemosphere, 43 ,doi:10.1016/S0045-6535(00)00171-5*.p1141-1151

Weisser, D. C., Fifield, L. K., Tims, S. G., Lobanov, N. R., Crrk, G. G., Tsifakis, D., and Tunningley, T. B. (2013). Injection Optics for Fast Mass Switching for Accelerator Mass Spectrometry. *AIP Conf. Proc. **1515**, 464 (2013);* http://dx.doi.org/10.1063/1.4792817

Westphal, E. O. J. (1963). The linguistic prehistory of southern Africa: Bush, Kwadi, Hottentot and Bantu linguistic relationships. *Africa, 33:*p237-265.

Wikol, M., Hartmann, B., Brendle, J., Crane, M., Beuscher, U., Brake, J., and Shickel, T. (2007). Expanded Polytetrafluoroethylene Membranes and Their Applications. *Filtration and Purification in the Biopharmaceutical Industry*, Second Edition, Edited by Mark W. Jornitz and Theodore H. Meltzer.

Wollnik, H. (1987). Optics of Charged Particles, (Academic Press, New York)

Wollnik, H. (1967). Focusing of Charged Particles, ed. Septier, A. (Academic Press, New York)

Woodborne S., Hall, G., Robertson, I., Patrut, A., Rouault, M., and Loader, N. J., (2015).

A 1000-Year Carbon Isotope Rainfall Proxy Record from South African Baobab Trees (Adansonia digitata L.). *PLoS ONE 10(5):* e0124202. doi:10.1371/journal. pone.0124202

Yates, R. and A. Smith 1993. Ideology and hunter/herder archaeology in the South Western.

Cape. *Southern African Field Archaeology* 2: p96-104.

Zhao, X.-L, Nadeau, M.J, Killus, L.R. and Litherland, A.E. (1994). Detection of Naturally-Occurring ^{236}U from Uranium Ore. *Earth Plan. Sci. Lett 124*,p241.

Zworykin, V. K., Morton, G. A., Ramberg, E. G., Hiller, J. and Vance, A. W. (1945). Electron Optics and the Electron Microscope. *New York: John Wiley $ Son*

APPENDIX A
SHORT DESCRIPTION OF ACCELERATOR IMPROVEMENTS

The EN Tandem accelerator was transferred from University of the Witwatersrand in 2005 to iThemba LABS administered by the National Research Foundation (NRF) and Department of Science and Technology (DST) of the Rebublic of South Africa (RSA). The data acquisition system, OMDAQ, was purchased from Oxford Microbeams Ltd (UK). The vacuum pumps and other equipment that are related Nuclear Microprobe (NMP) were also improved. A new pelletron charging belt for the accelerator was installed. The terminal voltage stabilization was installed. Since the middle of 2006 and middle of 2007 when the building and accelerator became available, the reassembly and commissioning of Tandem accelerator for ion beam analysis (IBA) have been carried out and completed successfully.

The writer's contribution to this effort has been the ion-optical calculations of the AMS system, presented in this work, the design, building and assembly of the graphite target preparation laboratory for the AMS radiocarbon measurements, and also performing experiments demonstrating the versatility of radiocarbon AMS measurements. Of course, since these measurements were performed before the finalization of the AMS beam-lime at iThemba LABS, samples were analyzed at Lawrence Livermore National Laboratory at Livermore, California, USA. This analysis on quartz filters for environmental sample and shell for archaeological for radiocarbon analysis using AMS.

2005-2007

The interior of the accelerator building was reconstructed into the following dedicated areas, accelerator vault, experimental vault, control room, data room, electronics room, offices and user areas. The belt-charging system was replaced with a pelletron charging belt, new high-

voltage grading resistors and resistors mounts were installed. The axial electric field and spiraled magnetic field accelerator tubes were installed. A terminal voltage stabilization was installed.

The gas stripper was converted to recirculating gas stripper with high voltage (HV) terminal pumping. The corona probe, generating voltmeter and capacitive pick-offs were refurbished. The injection system was redesigned and upgraded which include the ion source MC-SNICS. The injection system and extraction beam line optics were redesigned by making use of the programs TRANSPORT and TOSCA which were not part of this study.

The services such as the cooling-water and compressed-air system were also upgraded. A de-ionised cooling-water plant was implemented (chiller plant). The vacuum systems were redesigned to be under computer control. A centralized computer control system and customized software were developed to be put in operation. A safety interlock systems were put into place. A new current measurement system, SABUS, control modules and power supplies interfaces were installed.

2009-2014

The AMS programme started at the beginning of 2009. The MC-SNICS ion source for AMS were first tested at ion source test bench at iThemba LABS (Faure) in December of 2009. The ion source gives 300 μA $^{12}C^-$. This was done with the help of Dr. Tom Brown from LLNL through International Atomic Energy Agency (IAEA) sponsored project. The computer controls for the injector, accelerator, and beam line were done by the Accelerator Group of iThemba LABS and Dr. Peter Steier from Vienna Environmental Research Accelerator (VERA).

AMS measurements require reproducible throughput of the ions through the accelerator. Because of hysteresis, the magnetic fields of the bending magnets cannot be

produced without a control loop utilizing the measurement of the field. That is why, Hall probes for the measurement of magnetic fields of the injector magnet and switching magnet were installed and put under computer control. The analyzing magnet was equipped with NMR probe for accurate measurement of the field, and the calibrations of the Tandem accelerator were done.

The injection system for AMS was installed with MC-SNICS ion source, Einzel lens, ESA, and new inflection magnet with large pole gap as compare to the magnet for ion beam analysis. Beam optics calculations were done firstly on lower energy until the middle of the tank. Second beam optics was done for higher energy side. The electrostatic quadrupole triplet, AMS analyzing magnet, cylindrical ESA, two magnetic quadrupole doublets, AMS switching magnet and detector were also installed at higher energy. The detection system was purchased and installed, along with pumps and vacuum controls.

APPENDIX B

PIXE ANALYSIS AT LEPHALALE

Table B.1: Mass concentrations of the Lephalale sample obtained from mass difference through the volume of sampler.

Sample I.D	Mass difference (g)	Mass concentration (µg/m3)
Blank1	0.000099	8.23
PFTE2	0.000358	29.77
PFTE10	0.000427	35.51
PFTE11	0.000418	34.76
PFTE21	0.000637	52.98
PFTE35	0.00024	20.00
PTFE36	0.000531	44.25

Mass concentration = (mass after exposure – mass before exposure)/volume, note that sampling period: 12 hours = 720 min, => sampled volume: 720*16.7= 12024L = 12.024 m^3.

Table B.2: PTFE 2 analysis.

Sample ID	Element	GUPIX(ng/cm^2)	Mass difference /area (mg/cm^2)	Concentration	Mol weight	µg/m^3
PTFE 2	**K**	19.1	0.0317	0.603	39.098	0.141
	Ca	1376.8	0.0317	43.43	40.08	10.151
	Ti	738.9	0.0317	23.31	47.9	5.448
	Mn	64.2	0.0317	2.025	54.938	0.473
	Fe	1212.7	0.0317	38.26	55.848	8.941
	Zn	99.7	0.0317	3.145	65.38	0.735

Table B.3: PTFE 10A analysis.

Sample ID	Element	GUPIX(ng/cm^2)	Mass difference /area (mg/cm^2)	Concentration	Mol weight	µg/m^3
PTFE 10A	**K**	419.5	0.0379	37.189	39.098	3.093
	Ca	119.3	0.0379	10.576	40.08	0.88
	Ti	111	0.0379	9.84	47.9	0.818
	Mn	0	0.0379	0	54.938	0
	Fe	533.1	0.0379	47.261	55.848	3.931
	Zn	0	0.0379	0	65.38	0

Table B.4: PTFE 11A analysis

Sample ID	Element	GUPIX(ng/cm^2)	Mass difference /area (mg/cm^2)	Concentration	Mol weight	µg/m^3
PTFE 11A	**K**	30.3	0.0371	2.686	39.098	0.223
	Ca	1927.6	0.0371	170.887	40.08	14.212
	Ti	1085.9	0.0371	96.268	47.9	8.006
	Mn	117.8	0.0371	10.443	54.938	0.868
	Fe	1677.8	0.0371	148.741	55.848	12.37
	Zn	119.3	0.0371	10.576	65.38	0.88

Table B.5: PTFE 21A analysis.

Sample ID	Element	GUPIX(ng/cm^2)	Mass difference /area (mg/cm^2)	Concentration	Mol weight	µg/m^3
PTFE 21A	**K**	34.2	0.0564	3.032	39.098	0.252
	Ca	3127.1	0.0565	277.225	40.08	23.056
	Ti	1669.5	0.0565	148.005	47.9	12.309
	Mn	0	0.0565	0	54.938	0
	Fe	2781.7	0.0565	246.605	55.848	20.509
	Zn	146.1	0.0565	12.952	65.38	1.077

Table B.6: PTFE 35A analysis

Sample ID	Element	GUPIX(ng/cm^2)	Mass difference /area (mg/cm^2)	Concentration	Mol weight	µg/m^3
PTFE 35A	**K**	0	0.0213	0	39.098	0
	Ca	53.7	0.0213	4.761	40.08	0.396
	Ti	0	0.0213	0	47.9	0
	Mn	0	0.0213	0	54.938	0
	Fe	621	0.0213	55.053	55.848	4.579
	Zn	0	0.0213	0	65.38	0

Table B.7: PTFE 36A analysis

Sample ID	Element	GUPIX(ng/ cm^2)	Mass difference /area (mg/cm^2)	Concentration	Mol weight	$\mu g/m^3$
PTFE 36A	**K**	54.5	0.0471	4.832	39.098	0.402
	Ca	6407.3	0.0471	568.023	40.08	47.241
	Ti	2451.2	0.0471	217.305	47.9	18.073
	Mn	252.1	0.0471	22.349	54.938	1.859
	Fe	3328.1	0.0471	295.044	55.848	24.538
	Zn	251.1	0.0471	22.261	65.38	1.851

APPENDIX C

BEAM OPTICS

The input for beam optics calculation of the injection system for AMS at iThemba LABS is shown below as show Tape 30.

```
&Data
Er = 11200.0000, q = -1.0000, w = 0.03900, xi = 15.0000
Freq = 2.00000, pqext = 2.5000, ichrom =  1, ibs =  0, xc = .00000
Smax = 10.0000, pqsmax = 1.00000000
emiti(1)= 94.7000, 94.7000, 5318.6200
emito(1)= 0.0000, 0.0000,  0.0000
beami(1)= 0.0000, 0.08650, 0.0000,
          0.0000, 0.08650, 17500000.00
beamf(1)= 0.0000, 0.16400, 1.59070,
          6.0000, 0.04900, 1.50970
beamo(1)= 0.0000, 0.0000,  0.0000,
          0.0000, 0.0000,  0.0000
beamci(1)= 0.0000, 0.0000,  0.0000,
            0.0000,-0.0000,  0.0000
xm = 47.67390, xpm = 292.33710
xmi = 5.0000, xpm i= 50.0000, ym = 60.0000, dpmi = 609887.750
dwmi = 0.03490, dpp = 731865.31200
xmf =  5.0000, xpmf = 10.0000, dpmf = 179.21510, dwmf = 118.8515
n1 = 1, n2 = 37, nel1 = 1, nel2 = 37, np1 = 1, np2 = 37
mt = 0, nc = 0, delta = 0.00001, nit = 10
mp  = 0, 0, 0, 0, 0, 0, 0, 0, 0, 0, 0, 0
mvc = 0, 0, 0, 0, 0, 0, 0, 0, 0, 0, 0, 0, 0, 0, 0, 0, 0, 0
ijm = 0, 0, 0, 0, 0, 0, 0, 0, 0, 0, 0, 0
val(1 = 0.00000, 0.00000, 0.0000, 0.0000, 0.0000, 0.0000
nprin = 0
nxtra = 0
sigi(1,1) = 6.3605, 0.0000, 0.0000, 0.0000, 0.0000, 0.0000
sigi(1,2) = 0.0000, 2.7209, 0.0000, 0.0000, 0.0000, 0.0000
sigi(1,3) = 0.0000, 0.0000, 7.9524, 0.0000, 0.0000, 0.0000
sigi(1,4) = 0.0000, 0.0000, 0.0000, 3.3201, 0.0000, 0.0000
sigi(1,5) = 0.0000, 0.0000, 0.0000, 0.0000, 0.0493, 0.0000
sigi(1,6) = 0.0000, 0.0000, 0.0000, 0.0000, 0.0000, 0.2500
nt(1) = 1, a(1,1) = 1.0000
nt(2) = 1, a(1,2) = 139.7250
nt(3) = 18, a(1,3) = 0.0000, 0.02200, 80.0000, 13.0000, 31.7500
nt(4) =  1, a(1,4 )= 316.250
nt(5) =  1, a(1,5) = 1.0000
nt(6) = 18, a(1,6) = 0.0000, 0.0240, 115.0000, 13.0000, 57.3500
nt(7) =  1, a(1,7) = 396.7250
nt(8) =  1, a(1,8) = 306.0000
nt(9) = 17, a(1,9) = 0.0000, 0.0000, 90.0000, 306.0000, 306.0000
nt(10) = 1, a(1,10) = 301.5000
nt(11) = 1, a(1,11) = 10.7000
nt(12) = 20, a(1,12) = 0.0000,-0.0020, 50.0000, 20.0000, 20.0000
```

```
nt(13) =  1, a(1,13) = 1181.9000
nt(14) =  9, a(1,14) = 30.0000, 608.0000, 94.0000, 0.4500, 2.8000
nt(15) =  8, a(1,15) = 90.0000, 608.0000, 0.00000, 0.00000
nt(16) =  9, a(1,16) = 28.0000, 608.0000, 94.0000, 0.4500, 2.8000
nt(17) =  1, a(1,17) = 1197.90
nt(18) = 20, a(1,18) = 0.0000, -0.0020, 50.0000, 20.0000, 20.0000
nt(19) =  1, a(1,19) = 125.0000
nt(20) =  1, a(1,20) = 221.8000
nt(21) = 18, a(1,21) = 0.0000, 0.0230, 127.0000, 8.0000, 50.6000
nt(22) =  1, a(1,22) = 256.0000
nt(23) =  1, a(1,23) = 254.7500
nt(24) = 18, a(1,24) = 0.0000, 0.0270, 127.0000, 9.2500, 50.6000
nt(25) =  1, a(1,25) = 307.6300
nt(26) = 20, a(1,26) = 0.00000, -0.0200, 50.0000, 25.0000, 25.0000
nt(27) =  1, a(1,27) = 400.0000
nt(28) =  2, a(1,28) = 722.0000, 722.0000, 0.0000
nt(29) = 20, a(1,29) = 1.0000, -0.0948, 228.4200, 0.0000, 0.0000
nt(30) =  2, a(1,30) = 1723.300, 1723.3000, 0.0000
nt(31) = 20, a(1,31) = 1.0000, -1.3268, 1598.9399, 0.0000, 15.0000
nt(32) =  1, a(1,32) = 152.0000
nt(33) = 20, a(1,33) = 1.0000, -1.5584, 1878.1200, 15.0000, 12.0000
nt(34) =  1, a(1,34) = 17.5500
nt(35) =  1, a(1,35) = 139.0000
nt(36) =  1, a(1,36) = 740.0000
nt(37) =  1, a(1,37) = 1000.0000
&end
```

The aperture data of the injection system is shown below:

TRACE 3D APERTURE DATA (Lower energy) 04-22-2015 10:32:03

Aperture Multiplication Factor = 1.000000

Values at Point of Maximum Beam Extent: (all units = mm)

Element No.	Profile Type	Radial Profile X	Radial Profile Y	Factor* Profile Center X	Factor* Profile Center Y	Circular Profile +Center X	Circular Profile +Center Y	Beampipe Radius R
1	Drft	2.86	2.86	0.00	0.00	2.86	2.86	4.05
2	Drft	5.47	5.47	0.00	0.00	5.47	5.47	7.74

3	Ezl1	11.08	11.08	0.00	0.00	11.08	11.08	15.67
4	Drft	11.58	11.58	0.00	0.00	11.58	11.58	16.38
5	Drft	11.59	11.59	0.00	0.00	11.59	11.59	16.39
6	Ezl1	14.94	14.94	0.00	0.00	14.94	14.94	21.13
7	Drft	8.87	8.87	0.00	0.00	8.87	8.87	12.54
8	Drft	8.42	8.42	0.00	0.00	8.42	8.42	11.90
9	Prsm	10.19	10.19	0.00	0.00	10.19	10.19	14.42
10	Drft	6.42	6.42	0.00	0.00	6.42	6.42	9.07
11	Drft	4.67	4.67	0.00	0.00	4.67	4.67	6.60
12	Tube	8.13	8.13	0.00	0.00	8.13	8.13	11.49
13	Drft	40.46	40.46	0.00	0.00	40.46	40.46	57.21
15	Bend	57.12	39.09	0.00	0.00	57.12	39.09	69.21
17	Drft	40.34	37.67	0.00	0.00	40.34	37.67	55.20
18	Tube	40.34	37.67	0.00	0.00	40.34	37.67	55.20
19	Drft	6.34	6.27	0.00	0.00	6.34	6.27	8.91
20	Drft	12.69	12.15	0.00	0.00	12.69	12.15	17.57
21	Ezl1	21.40	20.31	0.00	0.00	21.40	20.31	29.51
22	Drft	16.55	15.63	0.00	0.00	16.55	15.63	22.76
23	Drft	13.86	12.99	0.00	0.00	13.86	12.99	18.99
24	Ezl1	13.86	12.99	0.00	0.00	13.86	12.99	18.99
25	Drft	8.76	8.41	0.00	0.00	8.76	8.41	12.14
26	Tube	12.84	12.17	0.00	0.00	12.84	12.17	17.69

27	Drft	23.71	22.29	0.00	0.00	23.71	22.29	32.54
28	Lens	23.71	22.29	0.00	0.00	23.71	22.29	32.54
29	Tube	23.71	22.29	0.00	0.00	23.71	22.29	32.54
30	Lens	23.71	22.29	0.00	0.00	23.71	22.29	32.54
31	Tube	23.71	22.29	0.00	0.00	23.71	22.29	32.54
32	Drft	9.89	9.23	0.00	0.00	9.89	9.23	13.53
33	Tube	9.89	9.23	0.00	0.00	9.89	9.23	13.53
34	Drft	3.05	3.14	0.00	0.00	3.05	3.14	4.37
35	Drft	3.03	3.17	0.00	0.00	3.03	3.17	4.39
36	Drft	4.17	4.35	0.00	0.00	4.17	4.35	6.02
37	Drft	7.14	7.16	0.00	0.00	7.14	7.16	10.11

MAX VALUES: 57.12 40.46 0.00 0.00 57.12 40.46 69.21

VALUES ON ABOVE RUN: I= 15.0mA W(in)= 0.0390 W(out)= 3.0385MeV

EMITi= 94.700 94.700 5318.62, EMITo= 10.865 10.730 5319.35

Minimum Beampipe Radius Required(Factor= 1.000) R= 69.21 mm

The input for high energy beam optics calculation of iThemba LABS AMS system is shown below as show Tape 30.

```
&Data
er = 11200.0000, q = 3.0000, w = 3.0390, xi = 0.0001
freq = 0.9500, pqext = 2.5000, ichrom =  1, ibs =  0, xc = 0.0000
smax = 10.0000, pqsmax = 1.00000000
emiti(1)= 104.7000, 104.7000, 5850.4800
emito(1)= 0.0000, 0.0000, 0.0000
beami(1)= 0.0000, 1.5300, 0.0000,
          0.0000, 1.5300, 19300.00
beamf(1)= 0.7379, 1.5961, 0.3099,
          6.9385, 0.00000027, 4832879.786
beamo(1)= 0.0000, 0.0000,  0.0000,
          0.0000, 0.0000,  0.0000
beamci(1) = 0.0000, 0.0000,  0.0000,
            0.0000,-0.0000,  0.0000
xm = 100.00, xpm = 39.7072
xmi = 30.3759, xpmi= 19.8536, ym = 100.0000, dpmi = 805419.904
dwmi = 0.0418, dpp = 161000.00
xmf =  30.3759, xpmf = 19.8536, dpmf = 805419.904, dwmf = 0.041848515
n1 = 1, n2 = 42, nel1 = 1, nel2 = 42, np1 = 1, np2 = 42
mt = 0, nc = 0, delta = 0.00001, nit = 10
mp  = 0, 0, 0, 0, 0, 0, 0, 0, 0, 0, 0, 0
mvc = 0, 0, 0, 0, 0, 0, 0, 0, 0, 0, 0, 0, 0, 0, 0, 0, 0, 0
ijm = 0, 0, 0, 0, 0, 0, 0, 0, 0, 0, 0, 0
val(1 = 0.00000, 0.00000, 0.0000, 0.0000, 0.0000, 0.0000
nprin = 0
nxtra = 0
sigi(1,1) = 6.3605, 0.0000, 0.0000, 0.0000, 0.0000, 0.0000
sigi(1,2) = 0.0000, 2.7209, 0.0000, 0.0000, 0.0000, 0.0000
sigi(1,3) = 0.0000, 0.0000, 7.9524, 0.0000, 0.0000, 0.0000
sigi(1,4) = 0.0000, 0.0000, 0.0000, 3.3200, 0.0000, 0.0000
sigi(1,5) = 0.0000, 0.0000, 0.0000, 0.0000, 0.0492, 0.0000
sigi(1,6) = 0.0000, 0.0000, 0.0000, 0.0000, 0.0000, 0.2500
nt(1) = 1, a(1,1) = 1.0000
nt(2) = 1, a(1,2) = 17.5500
nt(3) = 1, a(1,3) = 139.1000
nt(4) =  1, a(1,4 )= 740.0000
nt(5) =  20, a(1,5) = 1.0000, 1.5950,  1878.120,  12.5000, 15.0000
nt(6) = 1, a(1,6) = 1.0000
nt(7) =  20, a(1,7) = 1.00000, 1.7032, 2005.200,  15.0000, 20.0000
nt(8) =  1, a(1,8) = 904.0000
nt(9) = 22, a(1,9) = 5.6500, 288.5000, 19.0000
nt(10) = 1, a(1,10) = 85.0000
nt(11) = 22, a(1,11) = 5.6500, 288.5000, 19.0000
nt(12) = 1, a(1,12) = 85.0000
nt(13) =  22, a(1,13) = 5.6500, 288.5000, 20.0000
nt(14) =  1, a(1,14) = 1850.000
nt(15) =  1, a(1,15) = 2310.0000
nt(16) =  1, a(1,16) = 1341.0000
nt(17) =  22, a(1,17) = 23.600, 162.6000, 22.0000
nt(18) = 10, a(1,18) = 13.3
```

```
nt(19) =  22, a(1,19) = -25.6000, 281.0000, 22.0000
nt(20) =  1, a(1,20) = 13.3000
nt(21) =  22, a(1,21) = 0.0000, 0.0230, 127.0000, 8.0000, 50.6000
nt(22) =  1, a(1,22) = 5746.8000
nt(23) =  1, a(1,23) = 2475.0000
nt(24) =  1, a(1,24) = 2600.0000
nt(25) =  9, a(1,25) = 26.7000, 1270.0000, 34.0000, 0.4500, 2.8000
nt(26) =  8, a(1,26) = 90.0000, 1270.0000,  0.0000, 0.0000
nt(27) =  9, a(1,27) = 26.7000, 1270.0000, 34.0000, 0.4500, 2.8000
nt(28) =  1, a(1,28) = 1641.0000
nt(29) =  1, a(1,29) = 192.0000
nt(30) =  1, a(1,30) = 2620.0000
nt(31) =  6, a(1,31) = 13.5000, 81.0000, 119.0000
nt(32) =  1, a(1,32) = 177.0000
nt(33) = 17, a(1,33) = 1.0000, 0.0000, 22.5000, 3810.0000, 3810.0000
nt(34) =  1, a(1,34) = 986.0000
nt(35) =  9, a(1,35) = 0.0000,  1480.0000, 34.0000, 0.4500, 2.8000
nt(36) =  8, a(1,36) = 25.0000, 1480.0000, 0.0000,  0.0000
nt(37) =  9, a(1,37) = -12.5000,1480.0000, 34.0000, 0.4500, 2.8000
nt(38) =  1, a(1,38) = 126.0000
nt(39) =  1, a(1,39) = 986.0000
nt(40) =  6, a(1,40) = 15.5000,   81.0000,  119.0000
nt(41) =  1, a(1,41) = 484.0000
nt(42) =  1, a(1,42) = 864.0000

&end
```

TRACE 3D APERTURE DATA (Higher energy) 08-12-2015 14:53:02

Aperture Multiplication Factor = 1.000000

Values at Point of Maximum Beam Extent: (all units = mm)

Element No.	Type	Radial Profile X	Radial Profile Y	Factor* Center X	Factor* Center Y	Circular Profile +Center X	Circular Profile +Center Y	Beampipe Radius R
1	Drft	12.66	12.66	0.00	0.00	12.66	12.66	17.90
2	Drft	12.66	12.66	0.00	0.00	12.66	12.66	17.90

3	Drft	12.72	12.72	0.00	0.00	12.72	12.72	17.99
4	Drft	14.67	14.67	0.00	0.00	14.67	14.67	20.75
5	Tube	20.09	20.09	0.00	0.00	20.09	20.09	28.41
6	Drft	20.81	20.81	0.00	0.00	20.81	20.81	29.43
7	Tube	27.44	27.44	0.00	0.00	27.44	27.44	38.80
8	Drft	31.35	31.35	0.00	0.00	31.35	31.35	44.34
9	ESq2	28.02	37.44	0.00	0.00	28.02	37.44	46.76
10	Drft	25.74	40.75	0.00	0.00	25.74	40.75	48.19
11	ESq2	23.10	44.12	0.00	0.00	23.10	44.12	49.81
12	Drft	24.26	39.97	0.00	0.00	24.26	39.97	46.76
13	ESq2	25.73	36.47	0.00	0.00	25.73	36.47	44.63
14	Drft	26.88	29.46	0.00	0.00	26.88	29.46	39.88
15	Drft	9.52	17.05	0.00	0.00	9.52	17.05	19.53
16	Drft	18.71	31.41	0.00	0.00	18.71	31.41	36.56
17	ESq2	17.19	37.98	0.00	0.00	17.19	37.98	41.69
18	Drft	16.84	38.94	0.00	0.00	16.84	38.94	42.42
19	ESq2	15.14	44.11	0.00	0.00	15.14	44.11	46.64
20	Drft	17.30	38.54	0.00	0.00	17.30	38.54	42.25
21	ESq2	17.74	37.40	0.00	0.00	17.74	37.40	41.40
22	Drft	19.22	31.50	0.00	0.00	19.22	31.50	36.91
23	Drft	15.76	25.75	0.00	0.00	15.76	25.75	30.19
24	Drft	21.83	26.80	0.00	0.00	21.83	26.80	34.57

26	Bend	28.99	26.67	0.00	0.00	28.99	26.67	39.39
28	Drft	19.12	26.57	0.00	0.00	19.12	26.57	32.73
29	Drft	16.98	11.17	0.00	0.00	16.98	11.17	20.33
30	Drft	42.09	37.05	0.00	0.00	42.09	37.05	56.07
31	Doub	29.53	52.73	0.00	0.00	29.53	52.73	60.43
32	Drft	28.90	52.62	0.00	0.00	28.90	52.62	60.03
33	Prsm	27.00	50.03	0.00	0.00	27.00	50.03	56.85
34	Drft	8.18	28.17	0.00	0.00	8.18	28.17	29.34
36	Bend	15.57	5.53	0.00	0.00	15.57	5.53	16.52
38	Drft	16.63	4.41	0.00	0.00	16.63	4.41	17.21
39	Drft	25.18	12.03	0.00	0.00	25.18	12.03	27.90
40	Doub	18.33	19.29	0.00	0.00	18.33	19.29	26.61
41	Drft	16.67	20.53	0.00	0.00	16.67	20.53	26.45
42	Drft	13.66	19.93	0.00	0.00	13.66	19.93	24.16

MAX VALUES: 42.09 52.73 0.00 0.00 42.09 52.73 60.43

VALUES ON ABOVE RUN: I= 0.0mA W(in)= 3.3000 W(out)= 13.1923MeV

EMITi= 104.700 104.700 5850.48, EMITo= 52.368 52.368 5852.11

Minimum Beampipe Radius Required(Factor= 1.000) R= 60.43 mm